UNIVERSITÉ
LAVAL

# LES GLACES DE PAROI
## Glaciologie, thermodynamique et prévision des chutes de blocs de glace sur les routes du nord de la Gaspésie (Québec, Canada)

**Thèse**

FRANCIS GAUTHIER

**Doctorat en sciences géographiques**
Philosophiæ doctor (Ph.D.)

Québec, Canada

# RÉSUMÉ

Les glaces de paroi résultent du gel progressif des eaux de ruissellement sur une falaise. Dans le nord de la Gaspésie (Québec, Canada), soixante de ces glaces, parfois volumineuses (> 3000 m$^3$), ont été localisées près des routes. Entre 2000 et 2012, le Ministère des Transports du Québec (M.T.Q.) a effectué 440 interventions pour déblayer les blocs de glace tombés sur la chaussée. Une meilleure compréhension des mécanismes de croissance, de fonte et d'écroulement des glaces de paroi est nécessaire pour améliorer la gestion du risque. Des échantillons de glace ont été prélevés et leur microstructure analysée par tomodensitométrie et polarisation croisée. L'évolution volumétrique de quatre glaces de paroi a été modélisée à l'aide de différents modèles thermodynamiques et validée à partir de mesures du volume de glace effectuées au LiDAR. Une méthode de prévision des chutes de blocs de glace a été développée en comparant les dates des interventions du M.T.Q. avec les données météorologiques d'Environnement Canada. Les résultats ont permis de décrire les mécanismes de croissance des quatre types de glace constituant les glaces de paroi. Les modèles ont permis de démontrer que le gel de l'eau suite au transfert de chaleur par convection de l'air est le principal responsable de leur croissance. La fonte des cascades de glace, issues du gel des eaux d'une chute, est principalement initiée par l'augmentation du débit. Celle des carapaces de glace, issues du gel d'une résurgence, est plutôt le résultat de la convection de l'air et du bilan radiatif. Le calcul des degrés-heures de gel (ou de fonte), s'est avéré efficace pour modéliser l'évolution des carapaces de glace d'orientation nord. L'ajout du bilan radiatif à ce modèle a amélioré ses performances et permis une modélisation convenable de celle exposée au sud. Enfin, les effets des variables météorologiques sur l'occurrence des chutes de blocs de glace ont été simulés à l'aide de modèles logistiques. Le calcul des degrés-jours de fonte et le suivi du meilleur modèle statistique permettent de prédire l'écroulement de certaines glaces de paroi à quelques jours près. C'est une étape importante vers une gestion plus efficace de l'aléa.

# ABSTRACT

The growth of rockwall icings result from the gradual freezing of runoff on a cliff. In northern Gaspésie (Québec, Canada), sixty of these sometimes voluminous ice formations (over 3000 $m^3$) were located near roads. Between 2000 and 2012, 440 interventions to remove ice blocks from the road were conducted by the "Ministère des Transports du Québec" (M.T.Q.). A better understanding of the growth, melt and collapse dynamics of rockwall icings is needed to improve the management of this natural hazard. Ice samples were collected and their microstructure analyzed by computed tomography and under cross polarized light. The ice volume evolution of four rockwall icings was studied using various thermodynamic models and validated from ice volume measurements made with LiDAR imaging. An ice blocks fall forecasting method was developed by comparing the timing of M.T.Q. interventions with meteorological data. The results were used to describe the growth mechanisms of four different types of ice formation found on rockwalls. The models showed that freezing of the water to cold air convection is the main process responsible for their growth. In spring, the melting rate of the ice cascade or frozen waterfall clearly depends on the sensible heat carried by the increasing water flow. The melting of the ice walls formed from the freezing of seeping water coming from underground water resurgences rather is the result of air convection and the radiation heat budget (Qrad). A simple model based on the calculation of the freezing, or melting, degree-hours was also effective for simulating the evolution of the north facing ice walls. Including Qrad to this model improved its performance and allowed accurate modeling of the south facing ice wall. Finally, the effects of meteorological variables on the occurrence of ice blocks falls were simulated using logistic models. By following the trends of the melting degree-days and the best statistical model, it is possible to forecast the collapse of some of the most problematic rockwall icings and target the most hazardous periods along northern Gaspésie roads. This study is an important step towards a more effective management of this natural hazard.

# AVANT-PROPOS

Cette thèse étudie un processus géophysique très peu étudié à ce jour : la formation de glace sur les parois rocheuses. Elle est organisée en six chapitres. Le premier fait état des connaissances générales sur les glaces de paroi, présente la problématique et les objectifs de l'étude. Le portrait général du territoire à l'étude est aussi dépeint. Il est également question des méthodes d'analyse utilisées dans la caractérisation des divers types de glace constituant les glaces de paroi. Un bref survol des autres méthodes utilisées est effectué, mais le lecteur doit se référer aux trois « chapitres-articles » pour les détails. Il importe également de mentionner que ce type de présentation a entraîné une légère redondance dans la description de la méthode de mesure des volumes de glace effectuée au LiDAR et celle des modèles thermodynamiques présentés dans les deux premiers articles (chapitre 3 et 4). La deuxième section présente une caractérisation et une classification des diverses unités glaciologiques formant les glaces de paroi. Les trois chapitres suivants sont des articles soumis ou à soumettre dans des revues scientifiques avec une portée internationale. Ils sont présentés en anglais, mais un résumé en français est proposé au début de chacun d'eux. Les références de chacun des articles ont été combinées et sont présentées à la fin de la thèse. Enfin, les grandes lignes de l'étude sont résumées et les conclusions sont exposées dans le dernier chapitre de la thèse.

Le premier article s'intitulant « Ice cascade growth and decay: a thermodynamic approach » présente un modèle thermodynamique de croissance et de fonte d'une cascade de glace issue du gel des eaux d'une chute sur une falaise. Une multitude de données hydrométéorologiques acquises à proximité de la cascade de glace est également analysée. L'auteur de cette thèse, Francis Gauthier, est le premier auteur de l'article. Il a réalisé le schéma expérimental, procédé à l'installation des instruments scientifiques, traité les données, développé le modèle, rédigé la première version de l'article et procédé aux révisions suggérées par les quatre coauteurs. Maurine Montagant et Jérôme Weiss tous les deux du Laboratoire de Glaciologie et Géophysique de l'Environnement, une entité du Centre National de Recherche Scientifique à Grenoble en France, ont participé au processus de développement du modèle et de révision de l'article. Michel Allard (Centre d'études nordiques, Université Laval, Département de Géographie) et Bernard Hétu (Centre d'études

nordiques, Université du Québec à Rimouski, Module de Géographie), respectivement directeur et codirecteur de thèse, ont soutenu et conseillé M. Gauthier durant les diverses étapes de cette recherche. Ils ont également participé au processus de révision de l'article. Ce dernier a été accepté pour publication dans le *Journal of Glaciology* de la *International Glaciological Society* en date du 10 février 2013.

Les deux autres articles, « Ice walls growth and decay: meteorological analysis and modelling » et « Forecasting method of ice blocks fall by logistic model and melting degree-day calculation: a case study in Northern Gaspésie, Québec, Canada », n'ont pas encore été soumis à une revue scientifique. Ils seront soumis, respectivement, aux revues *Permafrost and Periglacial Processes* et *Natural Hazards*. Le premier présente une analyse des conditions micrométéorologiques responsables de la croissance et de la fonte de trois carapaces de glace issues du gel des eaux d'une résurgence sur des falaises présentant une géomorphologie et des orientations géographiques différentes. Un modèle thermodynamique et deux modèles simples de croissance et de fonte sont également proposés. Le second présente une méthode de prévision des chutes de blocs de glace provenant du dégel des glaces de paroi. La méthode s'appuie sur les données météorologiques d'Environnement Canada et les interventions de déblaiement des blocs de glace tombés sur la chaussée dans le nord de la Gaspésie et compilées par le Ministère des Transports du Québec. Tout comme le premier article, M. Gauthier est le premier auteur et il est à l'origine de toutes les démarches scientifiques préalables à la rédaction des articles. Les coauteurs de ces deux articles, Michel Allard et Bernard Hétu, ont participé au processus de révision des articles en plus d'agir à titre de conseillers scientifiques.

# REMERCIEMENTS

> Une passion pour le monde naturel ne s'enflamme pas, elle est en nous tous, mais nous refusons parfois de porter son essence.

C'est en endossant les gènes de mon père, Raymond Gauthier, décédé le 12 septembre 2000, que je me suis lancé dans l'étude des processus géophysiques. J'aimerais rendre hommage à cet homme d'exception et lui dédier cette thèse. Cet homme, un physicien, un hydrométéorologue original et avant-gardiste qui dans les années soixante-dix discutait de changement climatique en auscultant les données des stations météorologiques d'Hydro-Québec. Mon père, une personne qui souhaitait le bonheur des gens, de sa famille. Un être de partage, un mentor et un passionné. Un ami avec qui j'ai partagé le plaisir des sports de montagne. Lui qui considérait être une entité intégrante du cycle de l'eau, et bien il était et il demeurera une fraction indissociable de cette ingénieuse machine naturelle. La célèbre citation de Lavoisier « Rien ne se perd, rien ne se crée, tout ce transforme » est empreinte de multiples significations. Aujourd'hui, j'imagine que la perte de cet être m'a insufflé le feu, la chaleur, l'énergie ou l'intuition directrice de mes actes, mes pensées et mes passions. Il fut et sera une inspiration tout au long de ma brève explosion sur Terre.

En rédaction comme en recherche ou en amour, une seule philosophie s'impose : Tout va pour le mieux dans le meilleur des mondes (Candide de Voltaire). C'est avec une telle inspiration que j'avoue diriger ma vie et ses aspirations. Aujourd'hui soutenu par le chaleureux pragmatisme de Michel Allard et l'effervescent éclectisme de Bernard Hétu, je soumets ce travail à la communauté scientifique. Votre mentorat m'a donné confiance, vos budgets m'ont supporté, les moments passés ensemble m'ont inspiré et votre amitié m'a réjoui. Merci pour toute cette confiance, estime et passion partagée!

Je ne voudrais pas passer sous silence tous les *sapiens* qui ont allégé mon travail et rendu cette étude possible. Tout d'abord, les précieuses mains et les corps d'athlète de mes très valeureux aides de terrain : Rosalie Davreux, Mathieu Leblanc et Frédérick Banville-Côté. Les conseils remplis d'intelligence de Thomas Buffin-Bélanger et de Daniel Fortier ont éclairé mon cheminement. Le fabuleux accueil et le soutien intellectuel de Maurine Montagnat et Jérôme Weiss au Laboratoire de Glaciologie et Géophysique de

l'Environnement (LGGE) à Grenoble m'ont touché et poussé à me surpasser. Pour demeurer en France, merci à Luc Moreau, François Damilano, Didier Lavigne et la Fondation Petzel d'avoir pris soin de moi sur les petites cascades de glace alpines!

Tous les employés de la Section des mouvements de terrain au Ministère des Transports du Québec (M.T.Q.) et ceux du Centre de service de Sainte-Anne-des-Monts en Gaspésie doivent être remerciés. Parmi toutes ces personnes, je suis particulièrement redevable à Pascal Locat, Denis Demers et Danielle Fleury pour avoir cru si fort en moi et avoir donné tant de sens à cette thèse. J'ai également bénéficié du support de plusieurs étudiants du Laboratoire de géomorphologie et dynamique fluviale de l'UQAR, de certains membres du Centre d'études nordiques, des étudiants et chercheurs du LGGE et de Frédérick D'aigle du Laboratoire multidisciplinaire de scanographie pour les ressources naturelles et le génie civil de l'INRS-ETE.

*I would also like to greatly acknowledge my godfather André Gauthier, Raymond's brother, and my dear friend Alexandre Gauthier for their Shakespearean support.*

Des remerciements sans limites aux Eskiboys. Merci d'endurer et apprécier ma joie, ma voie et mes onomatopées dans les plus beaux moments de détente qu'un être de versant puisse souhaiter! Je tiens aussi à remercier Martine et Marie-Pier pour avoir partagée et supportée mon énergie et mes passions dans les moments les plus heureux, intenses et parfois ardus de mon existence.

Mes pensées se tournent maintenant vers les deux femmes de ma vie, ma mère Mariette Duhaime et ma sœur Jolène Gauthier, sans oublier sa « gang » composée de mon filleul Médrick et mes nièces Maïlie, Loïkim et Kaïlane. Tous sont issus du courageux et remarquable stock chromosomique de mon beau-frère Martin Heppell. Ils sont pour moi l'exemple le plus probant d'équilibre entre passion, raison et amour!

Finalement, je tiens aussi à remercier les organismes qui me nourrissent, m'abreuvent et me transportent depuis le début de cette aventure scientifique : les Fonds de recherche du Québec sur la nature et les technologies, les fameuses bourses EnviroNord du programme de formation FONCER du CRSNG en sciences environnementales nordiques et le Ministère des Transports du Québec.

# TABLE DES MATIÈRES

## LISTE DES TABLEAUX

# LISTE DES FIGURES

xviii

# LISTE DES SYMBOLES (CHAPITRES 3 ET 4)

$a$ : radiation linearization constant ($8.1 \times 10^7$ K$^3$)

$C_a$ : specific heat of air (1005 J·kg$^{-1}$·K$^{-1}$)

$C_w$ : specific heat of water (4218 J·kg$^{-1}$·K$^{-1}$ at 0$^o$C)

$C_i$ : specific heat of ice (2050 J·kg$^{-1}$·K$^{-1}$ at 0$^o$C)

$D_{in}$ : mass flux of water at the top (kg·s$^{-1}$)

$e_{(Ta)}$ : saturation water-vapor pressure at $T_a$ (Pa)

$e_{(Tf)}$ : saturation water-vapor pressure at 0$^o$C (611 Pa)

$e_{(Tis)}$ : saturation water-vapor pressure at $T_{is}$ (Pa)

$e_{(Twt)}$ : saturation water-vapor pressure at $T_{wt}$ (Pa)

$G$ : global radiation (long and short wave) (W·m$^{-2}$)

$H$ : height difference between the water level logger and the barometer (m)

$h_{wa}$ : convective heat-transfer coefficient at the water-air interface (W·m$^{-2}$·K$^{-1}$)

$h_{ia}$ : convective heat-transfer coefficient at the ice-air interface (W·m$^{-2}$·K$^{-1}$)

IR : long wave radiation from the ice surface

$I_t$ : mean ice thickness (m)

$k_{ice}$ : ice thermal conductivity ($\sim 2.22$ W·m$^{-1}$·K$^{-1}$ at 0$^o$C)

$k_{rw}$ : "rockwall" or hydrated shale thermal conductivity ($\sim 1.5$ W·m$^{-1}$·K$^{-1}$)

$K_s$ : bulk-exchange coefficients

$L_e$ : latent heat of evaporation at 0$^o$C (2 514 000 J·kg$^{-1}$)

$L_f$ : latent heat of freezing (melting) (334 000 J·kg$^{-1}$)

$L_s$ : latent heat of sublimation of ice (2 848 000 J·kg$^{-1}$)

$M$ : ice mass (Kg)

$P$ : atmospheric pressure (Pa)

$P_{wll}$ : atmospheric pressure at the water level logger height (Pa)

$R$ : relative humidity (%)

$S$ : mean surface area covered by the rockwall icings (G-Voile: 2294.81160 m$^2$; G-69: 1533.27 m$^2$; G-Amphi: 1009.74 m$^2$; G-195: 315.36 m$^2$)

$t$ : time (s)

$T$ : air temberature ($^o$C)

$T_a$ : air temperature (K)

$T_f$ : freezing water temperature (273.15 K)

$T_{is}$ : ice surface temperature ($T_{is} = T_a$), (K)

$T_{rw}$ : rockwall mean annual temperature at $X_{rw}$, *air mean annual temperature* (3.6$^o$C; 276.8K)

$T_{wt}$ : top water temperature (K)

$T_{wb}$ : bottom water temperature (K)

$U$ : wind speed (m·s$^{-1}$)

$U_d$ : mean water droplet (water flow) speed of free fall (m·s$^{-1}$)

$U_{eff}$ : effective wind speed (m·s$^{-1}$)

$V$ : ice volume (m$^3$)

$X_{rs}$ : ice-rockwall interface, rockwall surface (0 m)

$X_{rw}$ : rockwall mean annual temperature depth (2.1 m)

$\alpha$ : ice cascade albedo (0.5)

$\Delta T_w$ : water temperature variation between the top and the bottom of the rockwall (K)

$\rho_a$ : air density at standard atmospheric pressure (1.29 kg·m$^{-3}$)

$\rho_i$ : ice density (880 kg·m$^{-3}$)

$\sigma$ : Stephan-Boltzmann constant (5.67x10$^{-8}$ W·m$^{-2}$·K$^{-4}$)

$\sigma_{tot}$ : total uncertainty, ice cascade volume estimation

$\sigma_{1,2,3,4}$ : uncertainty 1 to 4

%IF : percentage of ice withheld onto the rockwall (%)

# CHAPITRE 1: INTRODUCTION

## 1. CADRE GÉNÉRAL ET PROBLÉMATIQUE

Les glaces de paroi sont des formations superficielles de glace qui se forment chaque hiver sur certaines falaises rocheuses à la faveur du gel progressif des eaux de ruissellement souterrain, hypodermique ou de surface (Gauthier 2008). Dans le nord de la Gaspésie (Québec, Canada), certaines glaces de paroi peuvent atteindre jusqu'à 4 m d'épaisseur et accumuler plus de 3000 m$^3$ de glace (Fig. 1.1) (Gauthier 2008; Gauthier & al. 2012). Plusieurs d'entre elles sont localisées en bordure de la route qui ceinture la Gaspésie. Certaines se forment sur des falaises situées au-dessus de talus d'éboulis de 30 à 40 degrés d'inclinaison se terminant à quelques mètres de la route (Fig. 1.1C). L'écroulement des glaces de paroi est un risque naturel méconnu de la communauté scientifique, mais connu depuis au moins 1940 par les employés responsables de l'entretien des routes du nord de la Gaspésie (Gauthier 2008; Gauthier & al. 2012). Le 4 mai 1987, le Ministère des Transports du Québec (M.T.Q., centre de service de Sainte-Anne-des-Monts) a lancé un programme d'inventaire des mouvements de masse affectant les routes du nord de la Gaspésie (Gauthier 2008; Gauthier & al. 2012; Girard & Hétu 1994; Hétu & al. 1994). Depuis cette date, une patrouille circule jour et nuit pour relever les dépôts des divers mouvements de masse (chute de blocs de glace, avalanche de neige, chute de pierre, écroulement rocheux, glissements de terrain, coulées de débris). Chacune des interventions pour libérer et nettoyer la chaussée est inscrite dans une base de données. En 2000, la base de données a été informatisée, et en 2006, on y dénombrait déjà 232 chutes de blocs de glace (Fig. 2A, 2B et 2C) (Gauthier 2008; Gauthier & al. 2012). Deux de ces événements causèrent des accidents de la route. Avec un débit journalier moyen variant entre 500 et 5000 automobilistes et entre 200 et 500 camionneurs en 2004, la gestion du risque de chute de blocs de glace est un réel défi pour les autorités responsables. Le manque de connaissance scientifique sur le sujet complique le travail du contremaître responsable de l'entretien des routes tant sur le plan de la gestion du personnel que celui des équipements.

Outre cette problématique, l'intérêt pour l'alpinisme et l'escalade de glace en Amérique du Nord est en croissance et le nombre de traumatismes rapportés depuis 1951 a

considérablement augmenté (American and Canadian Alpine Club 1999). Sur les 200 à 400 accidents signalés chaque année, 20% ont été causés lors de la pratique de l'escalade de glace. En France, où la pratique de ce sport est pleinement développée, le constat est similaire : 148 interventions de secours, 47 blessés graves et 22 décès ont été rapportés entre 2000 et 2006 (Montagnat & al. 2010). Les principales causes de ces accidents sont l'inaptitude du grimpeur, son manque d'expérience, un mauvais jugement ou l'occurrence d'un risque naturel comme une avalanche de neige, la chute d'un bloc de glace ou l'effondrement complet d'une structure de glace.

Les premières études connues portant sur les glaces de paroi remontent au milieu des années 1990. Les travaux de Girard & Hétu (1994) et Hétu & al. (1994) relatent l'occurrence de 232 chutes de blocs de glace tombées sur les routes du nord de la Gaspésie. Tous ces événements sont survenus au printemps entre 1987 et 1993. Certains d'entre eux se sont produits à la suite d'un cycle gélival journalier. D'après les travaux de Groleau (1994) et ensuite ceux de Gauthier (2008) et Gauthier & al. (2013), l'écroulement des glaces de paroi est également un processus géomorphologique et écologique important. La récurrence saisonnière, la magnitude et l'intensité du processus favorisent la mobilisation d'important volumes de débris rocheux et le maintien de couloirs exempts de végétation arborescente (Fig. 1.2D). Mais, c'est à partir de 2004 que des travaux portant spécifiquement sur la formation, la fonte et l'écroulement des glaces de paroi furent réellement entrepris (Bianchi 2004; Gauthier 2008; Gauthier & al. 2012; Montagnat & al. 2010; Weiss & al. 2011).

Les travaux de Bianchi (2004), Gauthier (2008) et Gauthier & al. (2012) ont relevé l'existence d'au moins deux types de glaces constituant les glaces de paroi : les glaces de ruissellement ou stalactites de glace et les glaces d'accrétion. La formation des stalactites de glace a abondamment été décrite et caractérisée tant en laboratoire (p.ex. Maeno & al. 1994a; Maeno & al. 1994b; Makkonen 1988; Short & al. 2006; Szilder & Lozowski 1994; Ueno 2007) qu'en milieu naturel (p.ex. de Bruyn 1997; Knight 1980; Laudise & Barns 1979; Montagnat & al. 2010). Cependant, le second type de glace n'a encore fait l'objet d'aucune investigation. La présence d'autres types de glace comme les croûtes de glace de neige ou l'évolution de la microstructure de ces divers types de glace durant la période de fonte n'ont pas été décrites. Bianchi (2004), Gauthier (2008) et Gauthier & al. (2012) ont

également identifié deux types de glace de paroi : les cascades de glace issues du gel des eaux d'une chute (écoulement de surface persistant) et les carapaces de glace résultant du gel des eaux d'une résurgence d'eau souterraine (écoulement intermittent). Une nomenclature et une classification des divers types et structures de glace doivent être établies pour éviter une redondance de termes et une meilleure cohérence entre les travaux à venir.

Entre 2007 et 2009, le suivi de deux glaces de paroi dans les Alpes françaises par Montagnat & al. (2010) a permis de démontrer qu'il était possible de simuler la croissance surfacique des glaces de paroi à l'aide d'un modèle simple de transfert de chaleur par conduction. Le modèle considère que l'eau s'écoule entre une couverture de glace s'épaississant et la paroi rocheuse. L'eau est à $0^{o}C$ et la surface extérieure du couvert de glace est à la température de l'air. L'approximation est valable, mais la croissance des glaces de paroi est beaucoup plus complexe. Une modélisation basée sur le bilan d'énergie des glaces de paroi est requise pour définir le rôle de tous les flux de chaleur impliqués dans le processus de croissance et de fonte des glaces de paroi. Les travaux de Gauthier (2008) et Gauthier & al. (2012) ont démontré que la fonte et la dynamique d'écroulement des formations de glace émanant du gel des eaux d'une chute (cascades de glace) divergeaient considérablement de celles issues du gel des eaux d'une résurgence d'eau souterraine (carapace de glace). Les cascades de glace tendent à fondre rapidement et se fragmenter sous l'effet d'une augmentation du débit tandis que les carapaces de glace semblent plutôt fondre lentement sur place avant de s'effondrer subitement. Ils ont également mis de l'avant le rôle probant de l'exposition au rayonnement solaire sur la fonte et le démantèlement accéléré des glaces de paroi. Des travaux portant sur ces deux types de glace de paroi et sur l'effet de l'exposition directe ou indirecte au rayonnement solaire sont nécessaires pour préciser le rôle du flux de chaleur sensible transporté par l'eau liquide sur les falaises et celui du bilan radiatif.

Enfin, diverses variables hydrométéorologiques ont été proposées pour expliquer la fonte et l'écroulement des glaces de paroi (Bianchi 2004; Gauthier 2008; Gauthier & al. 2012; Montagnat & al. 2010; Weiss & al. 2011) :

• une augmentation de la température de l'air au-dessus du point de fusion de la glace;

• une température maximale de l'air élevée;

• des écarts de températures majeurs et plus spécifiquement une diminution brutale de la température en dessous de $0^{\circ}$C;

• le niveau d'exposition au rayonnement solaire;

• une augmentation du débit.

Dans le but de développer une capacité prédictive, Gauthier (2008) et Gauthier & al. (2012) ont proposé l'utilisation des degrés-jours positifs (DJ) cumulés à partir du 1$^{er}$ mars de chaque année afin de suivre l'évolution de la hausse des températures au-dessus de $0^{\circ}$C. Il a été démontré que le nombre de DJ positifs cumulés avant l'écroulement d'une glace de paroi donnée était relativement restreint. Ces dernières années, des chutes de blocs de glace se sont produites en hiver et d'autres au début de la période de formation. Certains de ces événements ont atteint la route. Le développement d'un modèle permettant d'intégrer ces événements est requis pour assurer une gestion de l'aléa durant toute la saison froide. Gauthier & al. (2012) ont également proposé l'utilisation d'un modèle logistique à plusieurs variables (DJ, température maximale et minimale, précipitation liquide) pour cibler les périodes les plus à risque. Le modèle est adéquat, mais tout comme le suivi des DJ, il ne permet pas la prévision des événements automnaux et hivernaux. De plus, les travaux de Weiss & al. (2011) ont clairement démontré qu'une diminution brutale de la température de l'air était susceptible d'entrainer des contraintes mécaniques internes suffisantes pour favoriser l'ouverture de fractures et l'effondrement de certaines structures de glace instables comme les formations de glace suspendues. Des variables représentant les redoux hivernaux et les écarts de température doivent être intégrées dans le développement d'un modèle de prévision des chutes de blocs de glace sur les routes du nord de la Gaspésie.

4

**Figure 1.1.** Glaces de paroi dans la vallée de Mont-Saint-Pierre (A); glace de paroi #20 (voir figure 1.3B) à l'ouest du village de Manche d'Épée (B); la route 132 à l'ouest du village de Mont-Saint-Pierre (C).

**Figure 1.2.** Chutes de blocs à l'ouest du village de Mont-Saint-Pierre (A) et entre Marsoui et La Martre (B et C). Deux semaines après l'écroulement d'une glace de paroi en milieu forestier dans la vallée de Mont-Saint-Pierre (D).

## 2. OBJECTIFS

Le principal objectif de la thèse est de fournir une base de connaissance complète sur ce processus géophysique et d'en expliquer les processus de formation, de croissance, de fonte et de désintégration. Cet objectif fondamental est d'une grande portée pratique car son atteinte devrait permettre d'améliorer la gestion du risque de chutes de blocs de glace sur le réseau routier du nord de la Gaspésie. Indirectement, il est également question d'aider les professionnels de la montagne et les glaciéristes à améliorer leur capacité d'évaluation du risque d'instabilité associé au démantèlement des glaces de paroi. Pour ce faire, la thèse s'appuie sur les objectifs spécifiques suivants :

• Localiser toutes les glaces de paroi potentiellement à risque pour le réseau routier nord-gaspésien;

• Caractériser les divers types de glace constituant les glaces de paroi et décrire leurs mécanismes de formation;

• Proposer une classification des glaces de paroi et de leurs structures;

• Développer une méthode pour estimer les volumes de glace accumulés sur les falaises;

• Dresser le bilan d'énergie des glaces de paroi;

• Simuler la croissance et la fonte des glaces de paroi à l'aide d'un modèle thermodynamique basé sur le bilan d'énergie;

• Évaluer l'importance des divers flux de chaleur responsables de la croissance et de la fonte des glaces de paroi;

• Développer et tester l'efficacité de modèles simples pour simuler l'évolution volumétrique des glaces de paroi;

• Identifier les variables météorologiques responsables de la fonte, de la déstabilisation et de l'effondrement des glaces de paroi;

• Développer une méthode de prévision des chutes de blocs de glace.

## 3. TERRITOIRE À L'ÉTUDE

Le territoire à l'étude s'étend sur la Rive-Nord de la péninsule gaspésienne entre les villes de Matane et de Manche d'Épée (Fig. 1.3A). Entre Sainte-Anne-des-Monts et Manche d'Épée, la route 132 est enclavée sur presque toute sa longueur entre le littoral de l'estuaire du Saint-Laurent et les versants raides qui forment l'escarpement côtier (Fig. 1.3B). Les falaises de l'escarpement côtier sont préférentiellement orientées vers le nord. Le secteur à l'étude comprend également une portion de la route 198 (environ 6,5 km) entre le village de L'Anse-Pleureuse et l'extrémité sud du lac du même nom. Dans ce secteur, la route 198 est coincée entre le lac à L'Anse-Pleureuse et une série de versants abrupts d'orientation sud-ouest pouvant atteindre 350 mètres de dénivelé. La géologie des falaises dans le nord de la Gaspésie est dominée par des lits plissés de roches sédimentaires de l'Ordovicien moyen et supérieur (schiste argileux, grès lithique, dolomie, calcaire silteux) (Brisebois & Nadeau 2003). Ces roches hautement fissiles présentent un réseau de discontinuités très dense (Hétu & Vandelac 1989). Cette découpe d'origine tectonique et géomorphologique favorise l'infiltration des précipitations et facilite les écoulements d'eau dans le massif rocheux (Domenico & Schwartz 1990; Driese & al. 2001; Mah & Wyllie 2004; McKay & al. 2005; Moore 1988; Solomon & al. 1992; Walkinshaw & Santi 1996). À 23 km au sud de Matane, la route 195 longe sur environ un kilomètre une falaise dynamitée de 10 m de hauteur et orientée vers le sud. L'escarpement est composé de mudstone et siltstone lités (Brisebois & Nadeau 2003). Il est surmonté d'une couche de sable et de gravier stratifié d'origine fluvioglaciaire facilitant la percolation et les écoulements hypodermiques (Veillette & Cloutier 1993).

La plupart des versants donnant sur les routes 132 et 198 sont couverts par une végétation dense et arborescente. Par endroits, des couloirs étroits (< 30 mètres) et de longueurs variables (entre 30 et 250 mètres) fragmentent le couvert végétal. La plupart de ces couloirs sont dominés par des abrupts rocheux quasi verticaux de 5 à 60 mètres de hauteur où se forment des glaces de paroi. La pente de ces couloirs avoisine les 30 degrés et se termine fréquemment à moins d'une dizaine de mètres de la route. À de nombreux endroits, des talus détritiques segmentent les versants forestiers sur plusieurs centaines de mètres (Fig. 1.1C). La pente de ces talus est généralement courte (<100 m), abrupte (>30$^{\circ}$) et surmontée de falaises rocheuses pouvant atteindre une centaine de mètres de hauteur. Localement, des

glaces de paroi se forment sur ces escarpements. Enfin, des glaces de paroi peuvent également se former sur des falaises dynamitées situées directement en bordure de la route. Généralement, ces falaises s'élèvent à moins de 15 mètres de hauteur. Au total, 60 glaces de paroi ont été localisées sur cette portion du territoire à l'étude (Fig. 1.3B). Sur ce nombre, 22 ont été identifiés comme étant problématiques (à risque) par le M.T.Q..

Le climat de la région est caractérisé par des hivers froids avec un minimum moyen en janvier de -13,7$^o$C (Canada 1971-2000; Gagnon 1970). L'influence maritime de l'estuaire du Saint-Laurent assure des précipitations annuelles moyennes de près de 1000 mm réparties également sur l'ensemble de l'année. Le tiers de ces précipitations tombe sous forme de neige de la mi-novembre à la fin avril. Des précipitations automnales liquides relativement élevées (près de 200 mm pour octobre et novembre) assurent la recharge en eau des sols et des massifs rocheux avant l'hiver. L'excédent d'eau accumulé à l'automne ruisselle sur la surface de plusieurs parois rocheuses. À partir du mois de novembre, la température moyenne quotidienne descend sous le point de congélation. Cet abaissement graduel de la température permet aux eaux de ruissellement et aux résurgences de geler sur les falaises. L'accumulation de glace sur les falaises se poursuit généralement durant tout l'hiver (Gauthier 2008).
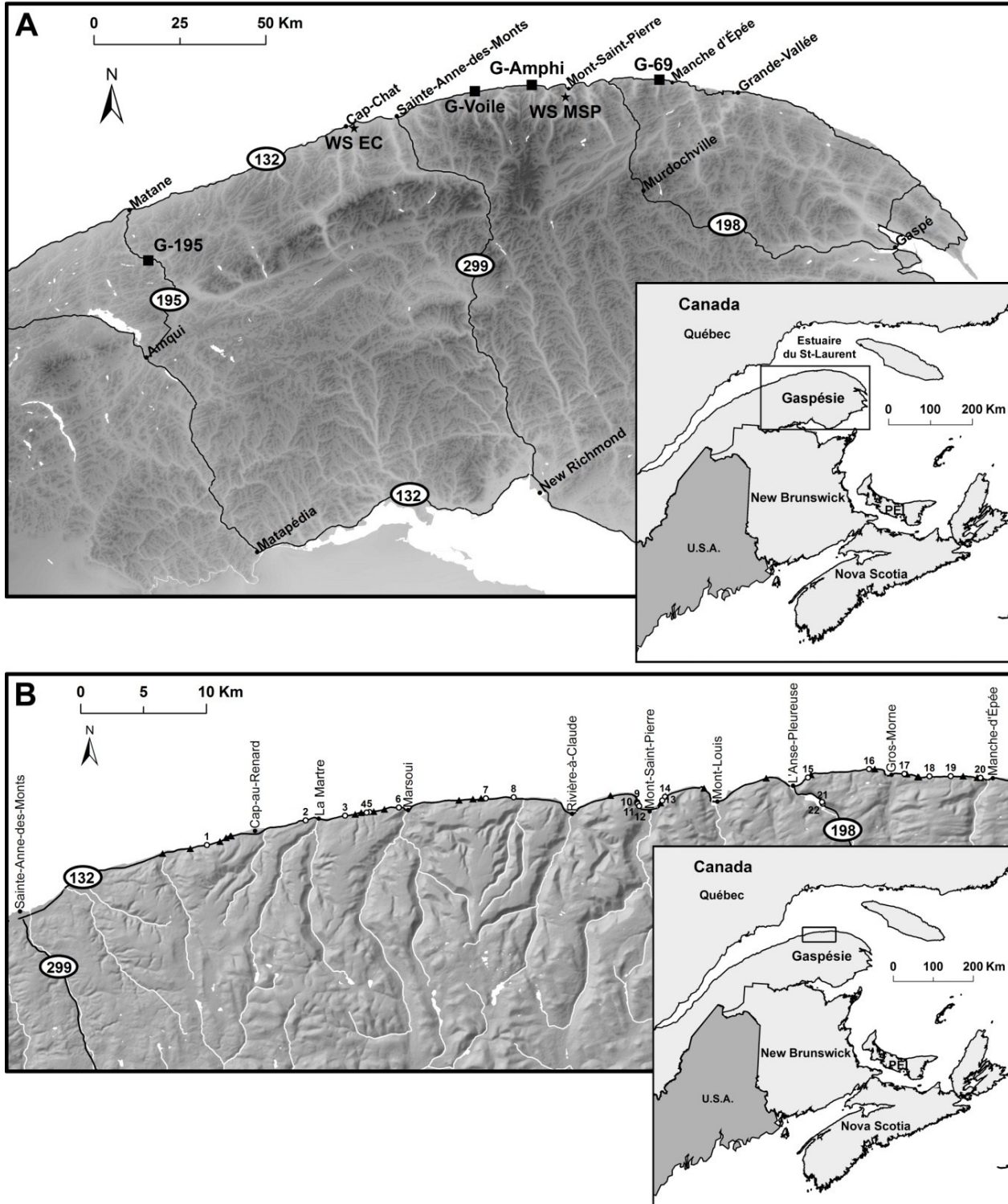
**Figure 1.3.** Localisation des sites d'étude et des stations météorologiques en Gaspésie (A) et localisation des 60 glaces de paroi (triangles noirs et cercles blancs) situées le long des routes 132 et 198 dans le nord de la Gaspésie (B). N.B. : les cercles blancs numérotés représentent les 22 glaces de paroi les plus problématiques pour le Ministère des Transports du Québec.

# 4. MÉTHODOLOGIE

## 4.1. CARACTÉRISATION GLACIOLOGIQUE

Depuis l'hiver 2006-2007, une vingtaine de glaces de paroi dispersées sur le territoire à l'étude ont fait l'objet d'un suivi photographique systématique à chacune des visites sur le terrain. (Gauthier 2008; Gauthier & al. 2012; Gauthier & al. 2013). En parallèle, des observations qualitatives (p.ex. : mécanismes de croissance de certaines structures de glace, source du ruissellement) et des mesures morphologiques et géomorphologiques (p.ex. : estimation du volume de glace au télémètre, orientation et inclinaison moyenne des falaises) ont également été effectuées. Des caméras automatiques Reconyx ont été installées à la base de quatre glaces de paroi afin de suivre et documenter leur croissance, leur fonte et leur dynamique d'écroulement. Les sites G-Amphi et G-69 ont fait l'objet d'un suivi photographique constant depuis l'automne 2006 jusqu'à la fin de l'hiver 2011 (Fig. 1.3B). Les sites G-Voile et G-69 ont été suivis durant l'hiver 2010-2011 (Fig. 1.3B). Chacune a été photographiée selon un intervalle variant entre une minute et une heure durant toute la durée de la saison froide. Au total, plus de 75 000 photographies ont permis de mieux comprendre les mécanismes de croissance et de fonte des glaces de paroi.

Les falaises et les glaces de paroi des sites G-195, G-Voile, G-Amphi et G-69 ont été balayées au LiDAR terrestre. Initialement, la surface des quatre falaises a été balayée en septembre 2010 alors que les débits étaient à leur plus faible niveau. À l'hiver 2010-2011, 29 balayages ont été répétés durant la période de croissance et de fonte des glaces de paroi. L'objectif était de modéliser la surface de ces glaces de paroi et d'estimer les volumes de glace accumulés en comparant les images acquises au cours de l'hiver avec celles acquises en septembre. La description de l'appareil et les détails de la méthode utilisée sont décrits en détail dans la section méthodologie des articles présentés aux chapitres 4.2 et 4.3.

Enfin, à l'hiver 2010-2011, des échantillons de diverses structures de glace ont été récupérés : trois stalactites de glace, trois accrétions de glace, deux croûtes de glace de neige et deux blocs de glace échantillonnés durant la période de dégel au cœur de deux glaces de paroi aux caractéristiques hydrologiques différentes : l'une issue du gel d'une chute d'eau sur une falaise et l'autre issue du gel d'une résurgence d'eau souterraine. Tous

ces échantillons ont fait l'objet d'une caractérisation au tomodensitomètre et d'une analyse cristallographique sous lumière polarisée croisée.

### 4.1.1. Tomodensitométrie

L'ensemble des échantillons a été balayé au tomodensitomètre Siemens SOMATOM Sensation 64 du Laboratoire multidisciplinaire de scanographie pour les ressources naturelles et le génie civil de l'Institut National de la Recherche Scientifique (Centre Eau, Terre et Environnement, Québec, Canada) (Fig. 1.4D). La théorie et les techniques sont décrites en détail par Hounsfield (1973) et Knoll (1989) et les détails sur le type d'appareil utilisé dans cette étude sont décrits par Boespflug & al. (1994), Calmels & Allard (2004) et Duchesne & al. (2009).

Essentiellement, la technique est basée sur les principes de la radiographie. Le CT-scan (tomographie assistée par ordinateur) permet de générer une série d'images constituées de 1024 x 1024 pixels suivant une échelle de 4096 teintes de gris représentant chacune une variation de la densité de 0,1%. La résolution spatiale du CT-scan est de 0,1 mm pour les sections transversales et 0,5 mm pour les sections longitudinales. La résolution finale des unités volumiques (ou voxels) est de 0,1 x 0,1 x 0,5 mm (0,005 mm$^3$). Ces paramètres permettent de reproduire des images 3D des structures balayées avec une résolution moyenne de 0,2 mm.

La densité (ou radiodensité) est calculée en terme d'intensité tomographique traduit en Unité Hounsfield (HU) (Hounsfield 1973):

$$HU = 1000 \times \frac{\mu_x - \mu_{eau}}{\mu_{eau}} \qquad (1.1)$$

où $\mu_{eau}$ est le coefficient d'absorption linéaire de l'eau et $\mu_x$ le coefficient d'absorption linéaire de la matière balayée au CT-scan. L'échelle de HU peut être traduite en densité apparente suivant une relation linéaire où $-1000$ HU correspond à la densité de l'air (1.2754 kg·m$^3$) et 0 HU est la densité de l'eau pure (1000 kg·m$^3$) sous des conditions de température et de pression normales (0$^o$C et 100 kPa). La densité apparente calculée avec

cette technique demeure une estimation, mais elle peut aisément être utilisée comme base de comparaison entre les diverses structures de glace balayées au CT-scan. Enfin, la porosité (n) ou le pourcentage de vides dans les échantillons de glace a été estimée en considérant la densité de la glace pure sans vide ($\rho_{glace}$) à $0^o$C (917 kg·m$^3$) :

$$n = \left(\left(\frac{\rho_{glace}}{\rho_x}\right) - 1\right) \times 100 \qquad (1.2)$$

où $\rho_x$ est la densité apparente des diverses structures de glace balayées au CT-scan.

### 4.1.2. Cristallographie

Les analyses cristallographiques des divers échantillons de glace ont été effectuées au Laboratoire de Glaciologie et Géophysique de l'Environnement (Centre national de la recherche scientifique, Université Joseph-Fourrier, Grenoble, France). Les détails de la technique et toutes les étapes d'analyse sont décrits par Durand & al. (2006).

En résumé, la technique requiert le dégrossissage à la scie à ruban des échantillons de glace suivant les axes perpendiculaires et transversaux à la direction présumée de croissance des structures de glace échantillonnées. Ces derniers sont ensuite fixés sur une lame mince de verre et coupés au microtome jusqu'à l'obtention d'une lame mince de glace de 0,3 à 0,2 mm d'épaisseur (Fig. 1.4A). L'épaisseur de la lame mince de glace est un paramètre important puisqu'elle permettra d'isoler les cristaux (ou grains) de glace. L'objectif est d'obtenir une surface de glace d'une épaisseur égale ou inférieure à celle des cristaux afin d'éviter une superposition de ces derniers et améliorer la qualité des mesures d'orientation des grains. Les lames minces de glace sont photographiées sous une lumière polarisée croisée (Fig. 1.4B). Cette étape permet d'effectuer une analyse qualitative de la forme, la disposition et de la taille des grains. Elle permet aussi d'évaluer la qualité de l'échantillon : un bon échantillon doit présenter des limites (frontières) bien définies entre les cristaux. Au total, 32 lames minces ont été préparées et photographiées sous lumière polarisée croisée.

L'étape suivante consiste à numériser les échantillons à l'aide d'un analyseur automatique des textures (fabriques) de glace (AITA) (Fig. 1.4C). Les images générées avec l'AITA

révèlent, sous une gamme de teintes de couleur choisie, l'orientation spatiale de l'axe-C des cristaux de glace. La direction de croissance de l'axe-C d'un grain de glace est perpendiculaire à la direction de croissance ou de nucléation du cristal de glace dans son environnement (p.ex. Durand & al. 2006; Montagnat & al. 2010). Le résultat de la distribution des orientations des axes-C est représenté dans un diagramme de Schmidt. Les analyses de texture ont été effectuées à l'aide des algorithmes disponibles dans une boite à outils MATLAB développée par Durand & al. (2006). Les treize meilleures lames minces représentant chacune des différentes structures de glace échantillons et suivant les deux axes de découpe (perpendiculairement et parallèlement à la direction de croissance) ont été balayées sous l'AITA et leurs textures analysées dans MATLAB.

**Figure 1.4.** Affinage d'une lame mince de glace au microtome (A). Photographie des cristaux de glace sous lumière polarisée croisée (B). Analyseur automatique des textures de glace (C). Échantillons de divers types de glace à l'aide d'un Scanographe SOMATON Sensation de Siemens (D). Station météorologique WS-MSP dans la vallée de Mont-Saint-Pierre (E). Station météorologique G-Voile : enregistreur de données, girouette et anémomètre (F), enregistreur de données et capteur de température dans son boîtier antiradiation (G), installation du pyranomètre sur son support (H) et pluviomètre (I).

15

## 4.2. INSTRUMENTATION ET DONNÉES MÉTÉOROLOGIQUES

Les données météorologiques proviennent des six stations présentes sur le territoire (Fig. 1.3A). La station WS-EC est localisée près de la côte de l'estuaire du Saint-Laurent à deux kilomètres à l'est de Cap-Chat. Elle est opérée par Environnement Canada depuis octobre 1996 (Canada 2000-2012)(Canada 2000-2012)(Canada 2000-2012). Les températures (moyenne, minimale et maximale), les précipitations totales, la vitesse et la direction du vent constituent l'essentiel des données horaires et quotidiennes disponibles à cette station. La station WS-MSP est située dans la vallée de Mont-Saint-Pierre à trois kilomètres de la côte (Fig. 1.3A). Cette station enregistre les données horaires et pluri-horaires de température de l'air, de pression atmosphérique, d'humidité relative, de précipitations liquides et solides, de hauteur de neige, de vitesse et direction du vent et de rayonnement direct, diffus et réfléchi depuis novembre 2009. Les sites G-195, G-Voile, G-Amphi et G-69 correspondent aux quatre glaces de paroi équipées de stations micro-météorologiques (Fig. 1.3A). Elles sont dotées à la fois d'équipement de mesures météorologiques conventionnels (p.ex. température de l'air, vitesse et direction du vent, humidité relative, pression atmosphérique) et hydrométéorologiques spécifiques au besoin de l'étude des glaces de paroi (p.ex. sondes pour mesurer la température de l'eau de ruissellement, à la surface des parois rocheuses et en profondeur, piézomètre pour mesurer les hauteurs d'eau). Ces dernières ont été installées à l'été 2009 et sont demeurées en opération jusqu'en juin 2011. La description de chacune des installations hydrométéorologiques associée à chacun de ces sites est détaillée dans la section méthodologie des articles présentés aux chapitres 3 et 4.

## 4.3. INVENTAIRE DES CHUTES DE BLOCS DE GLACE

En 1987, le M.T.Q. (centre de service de Sainte-Anne-des-Monts) a lancé un programme d'inventaire des mouvements de masse affectant la route 132 entre Ste-Anne-des-Monts et Manche d'Épée et un petit tronçon de la route 198 au sud de L'Anse-Pleureuse (Fig. 1.3). Chacune des interventions pour dégager et nettoyer la chaussée est inscrite dans une base de données. Dans le cadre de cette étude, les données couvrant la période 2000 à 2012 ont été utilisées. De plus amples détails sur ces données sont fournis dans la section méthodologie de l'article présenté au chapitre 5.

# CHAPITRE 2: CARACTÉRISATION GLACIOLOGIQUE ET CLASSIFICATION DES DIVERS TYPES ET STRUCTURES DE GLACE

## 1. TYPES DE GLACE ET MICROSTRUCTURES

Les glaces de paroi sont constituées de quatre types de glace : la glace de ruissellement (Fig. 2.1A et 2.1B), la glace d'accrétion (Fig. 2.1D et 2.1E), la glace de neige (Fig. 2.1C) et la glace de regel. Ces dernières ont été classifiées en fonction de leur mécanisme de formation, leur morphologie (structure externe) et leur microstructure interne (densité et cristallographie).

Durant les premiers stades de croissance, la glace de ruissellement et la glace d'accrétion forment l'essentiel des structures constituantes des glaces de paroi. Par la suite, des accumulations de neige sur ces structures de glace peuvent se transformer en croûte de glace de neige. Éventuellement, lorsque toutes ces structures croissent et fusionnent, elles vont former une seule entité de glace massive. Avec l'évolution des températures et les nombreux cycles de gel-dégel printaniers, la structure interne de la glace des glaces de paroi se métamorphose et une glace dite de regel apparait.
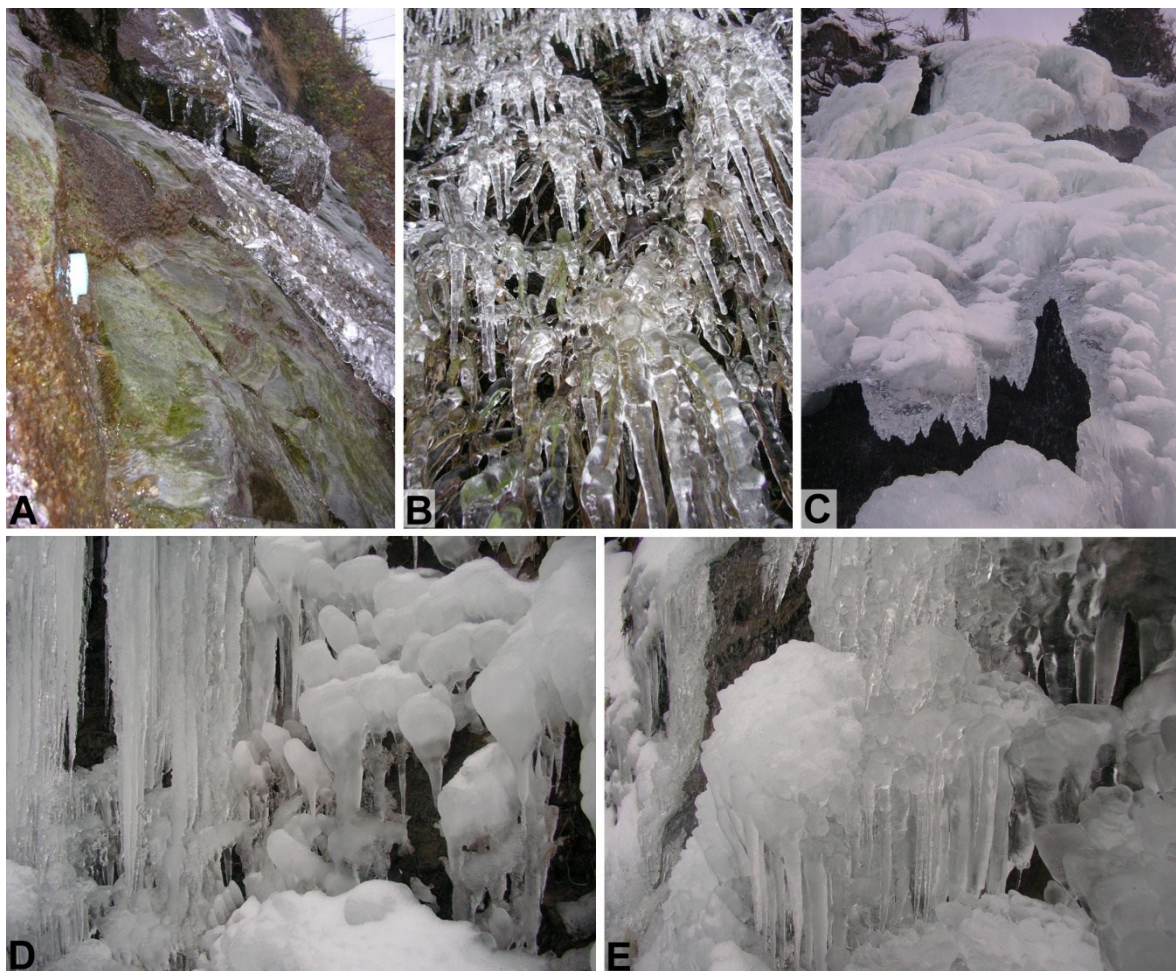
**Figure 2.1.** Glace de ruissellement : pellicule de glace (A) et stalactites de glace (B); croûtes de glace de neige (C); stalactites et accrétions de glace (D); accrétions de glace (E).

## 1.1. GLACE DE RUISSELLEMENT

Les glaces de ruissellement constituent les structures de glace dominant l'ensemble des formations de glaces de paroi (Gauthier 2008; Gauthier & al. 2012; Gauthier & al. 2013; Montagnat & al. 2010). Elles sont issues du gel des eaux de ruissellement sur des structures surplombantes, verticales et sub-verticales (p.ex. paroi rocheuse, structures de glace, branches) (Fig. 2.1A et 2.1B).

Le gel de l'eau de ruissellement donne naissance à deux formes de glace : les pellicules de glace (Fig. 2.1A) et les stalactites de glace (Fig. 2.1B et 2.1D). La première se forme lorsque l'eau ruisselle et gèle sur un plan incliné. Elles forment alors une pellicule de glace massive dont la surface est ondulée. Sur une structure peu inclinée, la morphologie et les

19

mécanismes de formation s'apparentent fortement à celle des aufeis (Schohl & Ettema 1986; Schohl & Ettema 1990; Streitz & Ettema 2002). Dans le cadre de cette étude, ce type de structure de glace n'a pas été échantillonné. Cependant, lorsqu'elles se forment sur des plans fortement inclinés, les mécanismes de croissance se rapprochent davantage de celui des stalactites de glace (Ueno 2003; Ueno 2004; Ueno 2007).

La morphologie et les mécanismes de formation des stalactites de glace ont largement été décrits et étudiés en laboratoire (Kharitonsky & Gonczarowski 1993; Maeno & al. 1994a; Maeno & al. 1994b; Makkonen 1988; Ogawa & Furukawa 2002; Short & al. 2006; Szilder & Lozowski 1994; Szilder & Lozowski 2000; Ueno 2003; Ueno 2004; Ueno 2007) et en milieu naturel (de Bruyn 1997; Gauthier 2008; Gauthier & al. 2012; Knight 1980; Laudise & Barns 1979; Lliboutry 1964; Makkonen 2000; Montagnat & al. 2010).

En résumé, il a été rapporté que la croissance d'une stalactite de glace débute avec la formation d'un petit nucleus résultant du gel d'une gouttelette pendante. Ce nucléus va croitre et s'allonger vers le bas pour former un long cristal de glace au centre de la structure (Fig. 2.2E). L'eau de ruissellement sur le pourtour de la stalactite favorisera une croissance radiale autour des cristaux centraux. L'excédent d'eau formera une gouttelette pendante au bout de la stalactite qui en gelant participera au processus d'élongation longitudinale de la stalactite. Durant le gel de cette gouttelette, de petites bulles d'air peuvent demeurer emprisonnées dans la structure de la stalactite (Fig. 2.2A, 2.2D et 2.2H).

Sur le diagramme de Schmidt de la coupe transversale d'une stalactite, deux distributions ressortent (Fig. 2.2F) : l'une dans la direction horizontale représentée par une zone dense sur l'axe X près de 90$^o$ et l'autre suivant la direction verticale distribuée le long de l'axe Y (Montagnat & al. 2010). La première représente l'orientation préférentiellement horizontale de l'axe C des longs cristaux (grains) allongés au centre de la stalactite. Le second démontre que l'orientation de l'axe C des petits grains allongés distribués radialement autour des cristaux centraux est principalement verticale. Ces résultats démontrent que les stalactites de glace tendent à croître longitudinalement, du haut vers le bas, suivant la direction de croissance des longs cristaux centraux et radialement, du centre de la stalactite vers l'extérieur, suivant la direction de croissance des cristaux distribués en périphérie.

20

Ce mécanisme de formation des stalactites donnera naissance à une glace translucide, dense et peu poreuse (Fig. 2.1A, 2.1B, 2.2A, 2.2D et Tab. 2.1). La morphologie externe présente de douces ondulations d'environ 1 cm de longueur entre les crêtes (Ueno 2007). Le taux de croissance de ces structures est très variable et peut varier de quelques millimètres par jour à une trentaine de centimètres par jour (Laudise & Barns 1979). Il est plus rapide lorsque les températures sont très froides et sous un faible régime hydrique (Maeno & al. 1994b; Makkonen 1988). En situation d'instabilité apparente (exposition au vent) et des températures froides ($<< 0^{o}$C), les stalactites présenteront une structure plus rugueuse avec des ondulations marquées et irrégulières, ainsi qu'une densité apparente moindre causée par la présence accrue de bulles d'air endogènes (Fig. 2.2H, 2.2I et Tab. 2.1, échantillon SGV). Maeno & al. (1994a) ont démontré que la courbure d'une stalactite s'accroit exponentiellement avec la vitesse du vent jusqu'à s'incurver à près de 80$^{o}$ sous des vents de 10 m·s$^{-1}$ (36 km·h$^{-1}$).

**Table 2.1.** Caractérisation densitométrique des divers types de glace de glace de paroi.

| Types de glace | Code échantillon | Volume (cm$^3$) | HUmoyen | Densité apparente (Kg·m$^{-3}$) | Densité apparente moyenne (Kg·m$^{-3}$) | Porosité (%) | Porosité moyenne (%) |
|---|---|---|---|---|---|---|---|
| Stalactites de glace | ST195[1] | 198.00 | -92.89 | 907.23 | | 1.08 | |
| | ST195-2[1] | 135.53 | -92.89 | 907.23 | 904.95 | 1.08 | 1.33 |
| | SGV[2] | 98.82 | -99.74 | 900.39 | | 1.84 | |
| Glace d'accrétion | CF[3] | 589.50 | -100.63 | 899.50 | | 1.95 | |
| | CR[4] | 1113.05 | -162.85 | 837.36 | 866.10 | 9.51 | 5.97 |
| | CS[5] | 91.57 | -138.74 | 861.44 | | 6.45 | |
| Glace de neige | GN-1[6] | 267.55 | -126.02 | 874.14 | 859.80 | 4.90 | 6.68 |
| | GN-2[6] | 193.77 | -154.74 | 845.46 | | 8.46 | |
| Glace de regel | GR-1[7] | 336.28 | -134.57 | 865.60 | 852.90 | 5.94 | 7.54 |
| | GR-2[7] | 211.23 | -160.01 | 840.19 | | 9.14 | |

[1] *Stalactite telle que présentée sur les figures 2.2A, 2.2D et 2.2G.*
[2] *Stalactite telle que présentée sur les figures 2.2H et 2.2I.*
[3] *Accrétion telle que présentée sur les figures 2.3A, 2.3D et 2.3G.*
[4] *Accrétion telle que présentée sur la figure 2.3I.*
[5] *Accrétion telle que présentée sur la figure 2.3H.*
[6] *Croûte de glace de neige telle que présentée sur la figure 2.4.*
[7] *Glace de regel telle que présentée sur la figure 2.6.*
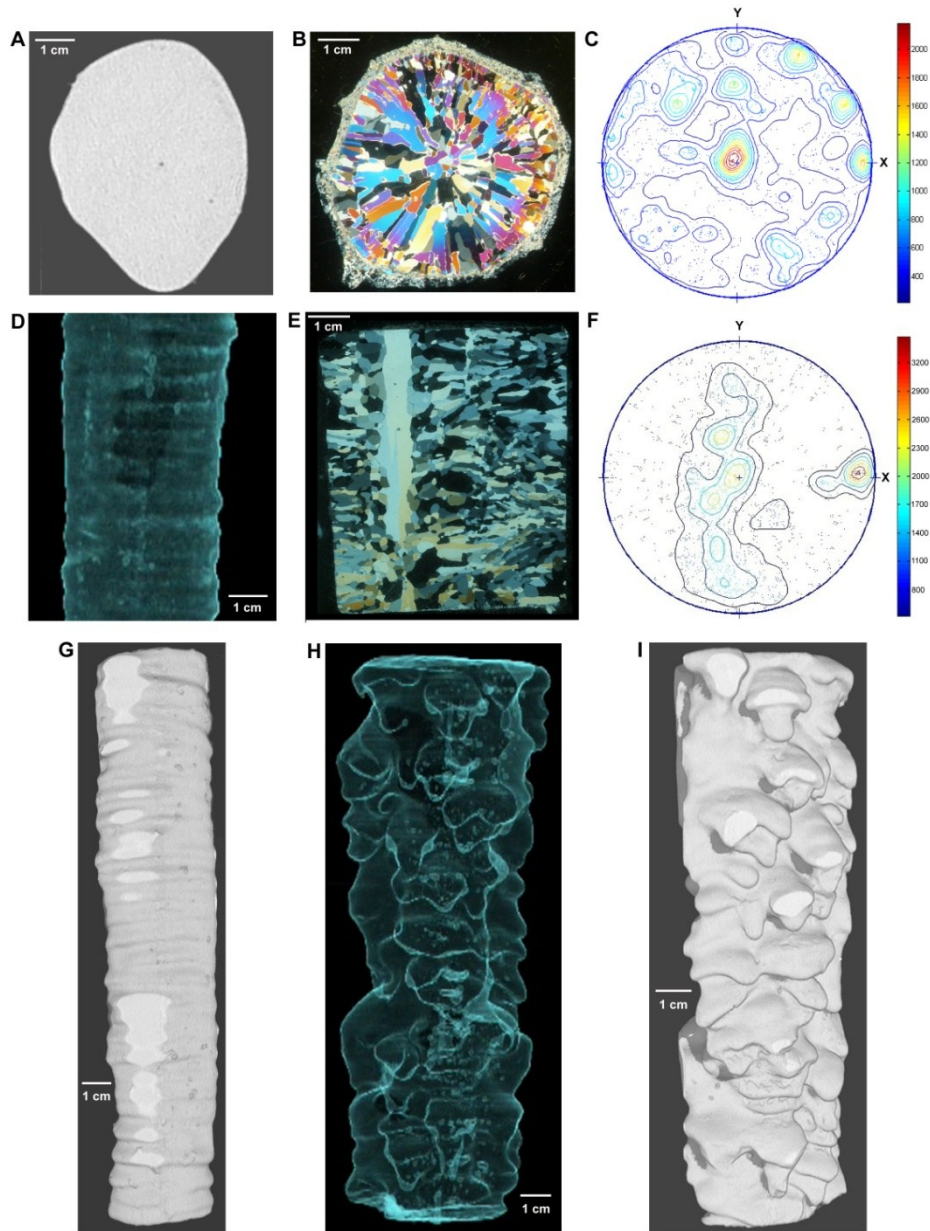
**Figure 2.2.** Morphologie, tomodensitométrie et microstructure des stalactites de glace. Images tomodensitométriques : coupe perpendiculaire bidimensionnelle (2D) (A), images tridimensionnelles (3D) volumiques (D et H), images 3D surfaciques (G et I). Photographie des cristaux de glace sous lumière polarisée, coupe perpendiculaire (B) et coupe transversale (E). Diagrammes de Schmidt (pole) des orientations préférentielle des axes C des cristaux de glace, coupe perpendiculaire (C) et coupe transversale (F).

N.B. : Sur les images tomodensitométriques 2D, les zones sombres ont des valeurs d'unité Hounsfield (HU) très faibles (environ -1000 HU), ils représentent des vides (bulles d'air) dans la structure de glace. Sur les images tomodensitométriques 3D volumiques, les lignes de contour clair représentent des changements abrupts de la densité (contours de la structure externe et bulles d'air endogènes). Les couleurs des photographies sous lumière polarisée croisée exposent la valeur d'orientation de l'axe C des cristaux de glace. Sur les diagrammes de Schmidt, chaque point est la projection de l'orientation de l'axe C d'un cristal de glace (à partir de chaque pixel de la photographie). Les planches E et F ont été adaptés des travaux de Montagnat & al. (2010).

## 1.2. GLACE D'ACCRÉTION

Les accrétions de glace, nommées « choux-fleurs » par les glaciéristes, se forment lorsque des éclats d'eau en suspension dans l'air, provenant principalement des eaux de ruissellement chutant de la falaise, rencontrent un obstacle solide (p.ex. : stalactite ou accrétion de glace, branche, rocher) dont la température est sous le point de congélation de l'eau (Fig. 2.3D et 2.3E). Lorsque la gouttelette, généralement en état de surfusion, entre en contact avec l'obstacle, l'eau s'étale et gèle à un rythme défini par les échanges énergétiques (libération de chaleur latente) entre les gouttelettes, l'obstacle solide et l'atmosphère (Lock 1990; Makkonen 2000). Un processus similaire à la formation du givre ou des accrétions de glace durant les épisodes de pluie verglaçante (Fortin & al. 2004; Jones 1996; Macklin & Payne 1967; Macklin & Payne 1969; Makkonen 2000). Si le transfert de chaleur est suffisant pour solidifier toute la gouttelette, une couche de glace poreuse (givre) se forme (croissance sèche). Si le transfert de chaleur est insuffisant, l'excédent d'eau en surfusion s'accumule à la surface de l'accrétion et éventuellement il peut être emprisonné dans la couche de glace pour former une couche de glace spongieuse (croissance humide). Une partie de l'eau peut également être évacuée du système et participer à la formation de stalactites de glace sous l'accrétion. Les accrétions de glace qui s'accumulent sur les parois rocheuses présentent généralement cette caractéristique morphologique (Fig. 2.3D et 2.3E). Pour qu'il y ait accumulation de glace à croissance sèche (Fig. 2.3H), la concentration et la taille des gouttelettes d'eau qui atteignent un obstacle solide doivent être restreintes, les températures doivent être très froides ($<< 0^o$C) et la vitesse du vent doit être élevée pour faciliter les transferts de chaleur entre la couche de glace et l'atmosphère (Makkonen 2000).

Ce mécanisme de croissance favorise la formation d'une glace plus poreuse avec une densité apparente moyenne inférieure à celle des stalactites (Fig. 2.3A, 2.3D, 2.3I et Tab. 2.1). Les axes C des cristaux ne présentent pas d'orientation préférentielle (Fig. 2.3C et 2.3F). Ces observations reflètent bien le mode de déposition et solidification des gouttelettes qui lors de l'impact tendent à geler rapidement sans privilégier une direction de croissance. La présence de grains allongés montre que plusieurs gouttelettes s'étaleront sur la surface de la concrétion avant de geler (Fig. 2.3B, 2.3E, 2.3J et 2.3K). Sur la figure 2.3I, une alternance de couche plus ou moins dense à la surface de la concrétion est apparente.

Ce patron de déposition suggère que la croissance des différentes structures de glace est variable et fortement contrôlée par les conditions météorologiques ambiantes, une observation également rapportée par Montagnat & al. (2010) pour les stalactites de glace. Les bandes noires, plus poreuses, sont formées lorsque la croissance est rapide. La glace présente alors les caractéristiques d'une croissance sèche, soit une glace blanchâtre et poreuse sans glace de ruissellement sous l'accrétion (Fig. 2.3H, Tab 2.1 échantillon CS). La taille des cristaux de glace est limitée par une nucléation accélérée des grains (Fig. 2.3J et 2.3K), une situation qui implique une transition vers des températures plus froides et des vitesses de vent plus élevées.
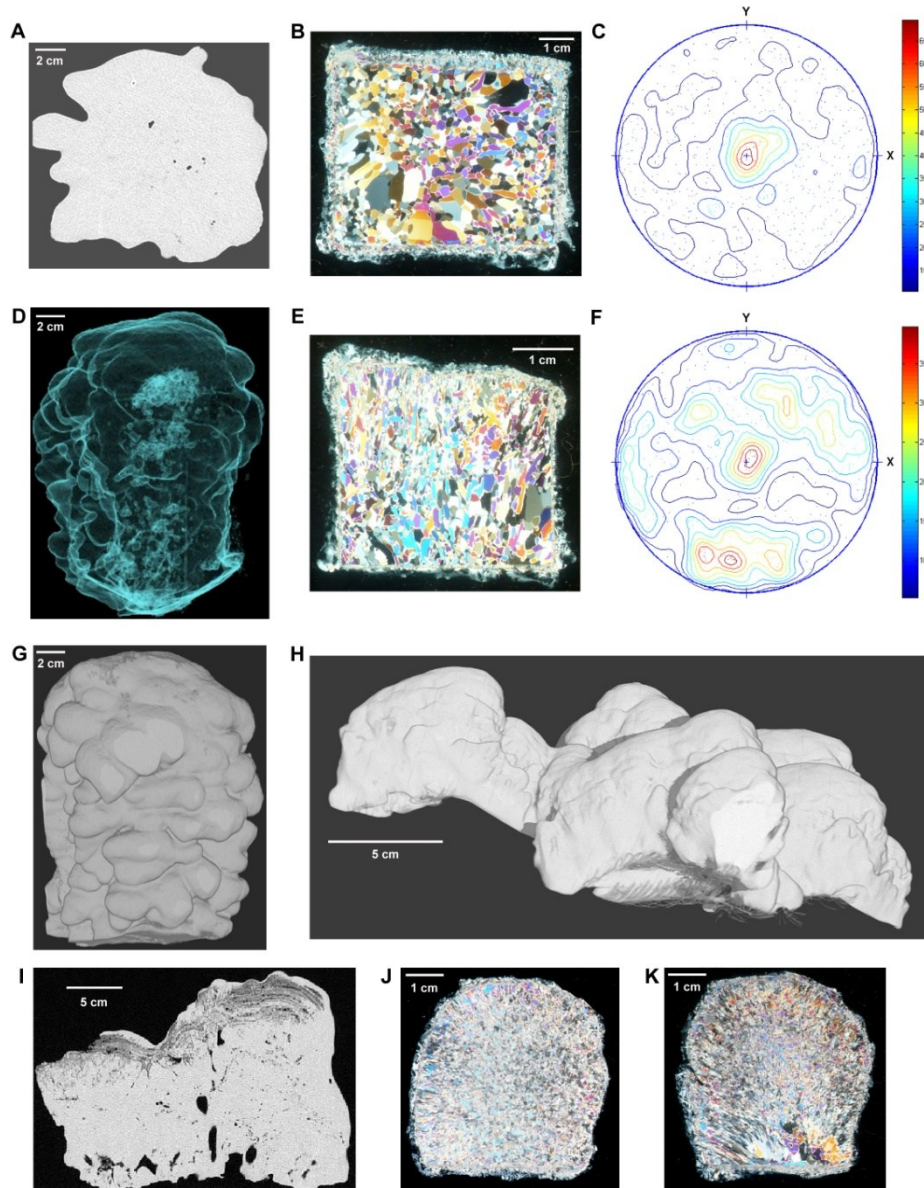
**Figure 2.3.** Morphologie, tomodensitométrie et microstructure des accrétions de glace. Images tomodensitométriques : coupe perpendiculaire bidimensionnelle (2D) (A), image tridimensionnelle (3D) volumique (D), image 3D surfacique (G et H), coupe transversale 2D (I). Photographie des cristaux de glace sous lumière polarisée, coupe perpendiculaire (B et J) et coupe transversale (E et K). Diagrammes de Schmidt (pole) des orientations préférentielle des axes C des cristaux de glace, coupe perpendiculaire (C) et coupe transversale (F).

N.B. : Sur les images tomodensitométriques 2D, les zones sombres ont des valeurs d'unité Hounsfield (HU) très faibles (environ -1000 HU), ils représentent des vides (bulles d'air) dans la structure de glace. Sur les images tomodensitométriques 3D volumiques, les lignes de contour clair représentent des changements abrupts de la densité (contours de la structure externe et bulles d'air endogènes). Les couleurs des photographies sous lumière polarisée croisée exposent la valeur d'orientation de l'axe C des cristaux de glace. Sur les diagrammes de Schmidt, chaque point est la projection de l'orientation de l'axe C d'un cristal de glace (à partir de chaque pixel de la photographie).

## 1.3. GLACE DE NEIGE

Les croûtes de glace de neige sont des unités de glace marginales et superficielles qui couvrent certaines zones restreintes des glaces de paroi (Fig. 2.1C). Ils se limitent aux zones peu inclinées où la neige peut s'accumuler et demeurer suffisamment longtemps pour subir une transformation. À la surface supérieure des croûtes de glace de neige, les cristaux sont plus petits (Fig. 2.4E). Directement en dessous, les cristaux sont plutôt fins et allongés dans la direction des infiltrations d'eau dans le couvert de neige. À la base, les cristaux ont tendance à être de plus grande taille. Les axes C des cristaux ne présentent aucune orientation préférentielle (Fig. 2.4C et 2.4F). Ces observations démontrent qu'un apport d'eau liquide externe (pluie ou éclat d'eau provenant de la source hydrique de la glace de paroi) ou une hausse des températures au-dessus de $0^{o}C$ est requis pour provoquer une fonte partielle des cristaux de neige de la couche extérieure, une fine percolation dans la couche de neige et la formation de gros cristaux de glace au centre et à la base de la couche de neige (p.ex. Colbeck 1979; Colbeck 1982; Colbeck 1983; Maeno & Nishimura 1979; McClung & Schaerer 2006). Enfin, la densité apparente moyenne de ce type de glace est plus faible que celles des accrétions et des stalactites (Tab. 2.1). La porosité plus élevée s'explique principalement par la morphologie irrégulière de la surface constituée de nombreux vides et les nombreux chenaux de percolation non comblés qui perforent et structurent les croûtes de glace de neige.

26
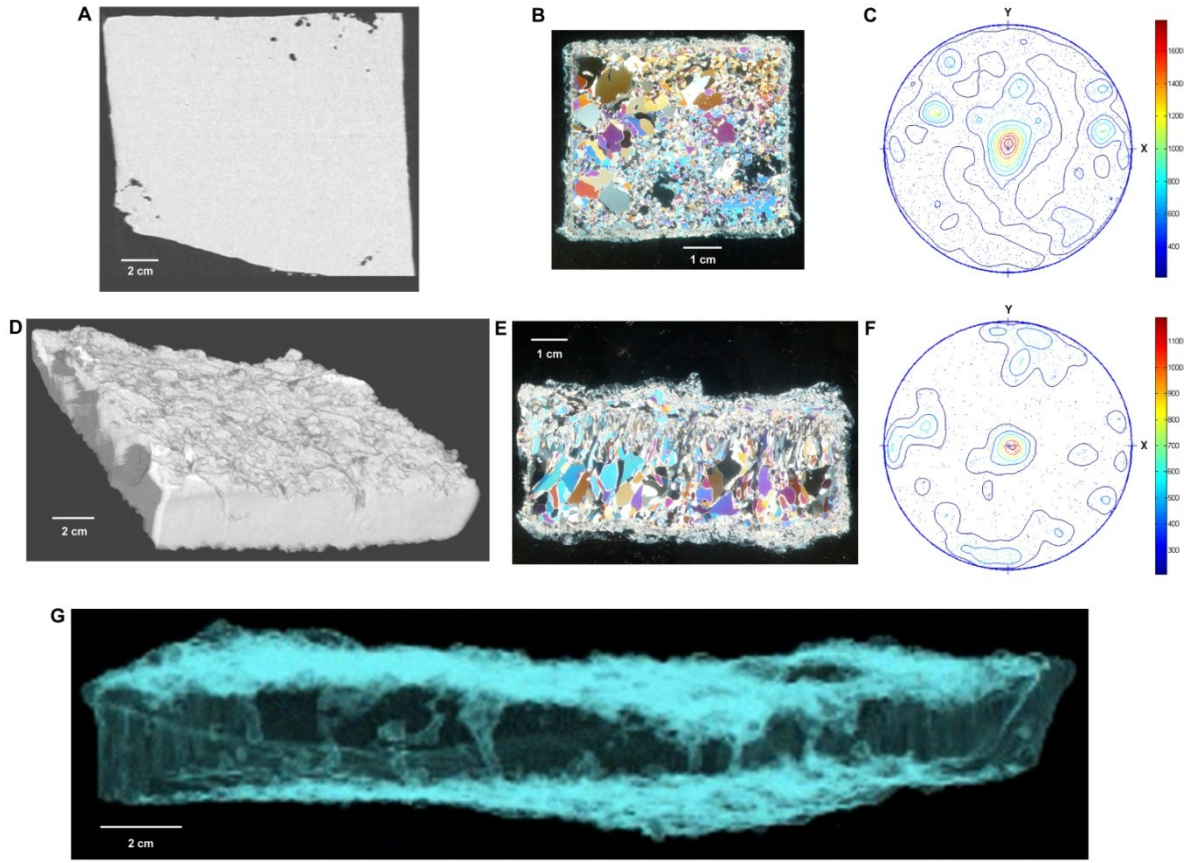
**Figure 2.4.** Morphologie, tomodensitométrie et microstructure des croûtes de glace de neige. Images tomodensitométriques : coupe perpendiculaire bidimensionnelle (2D) (A), image tridimensionnelle (3D) surfacique (D), image 3D volumique (G). Photographie des cristaux de glace sous lumière polarisée, coupe perpendiculaire (B) et coupe transversale (E). Diagrammes de Schmidt (pole) des orientations préférentielle des axes C des cristaux de glace, coupe perpendiculaire (C) et coupe transversale (F).

N.B. : Sur les images tomodensitométriques 2D, les zones sombres ont des valeurs d'unité Hounsfield (HU) très faibles (environ -1000 HU), ils représentent des vides (bulles d'air) dans la structure de glace. Sur les images tomodensitométriques 3D volumiques, les lignes de contour clair représentent des changements abrupts de la densité (contours de la structure externe et bulles d'air endogènes). Les couleurs des photographies sous lumière polarisée croisée exposent la valeur d'orientation de l'axe C des cristaux de glace. Sur les diagrammes de Schmidt, chaque point est la projection de l'orientation de l'axe C d'un cristal de glace (à partir de chaque pixel de la photographie).

## 1.4. GLACE DE REGEL

Au cours de l'hiver, les diverses structures de glace poursuivent leur croissance et finissent éventuellement par se toucher et fusionner entre elles pour former une seule entité de glace massive (Fig. 2.5). Tel que décrit par Montagnat & al. (2010), la microstructure de ces formations de glace s'apparente, dans son ensemble, à celle des stalactites de glace. En effet, lorsque les diverses structures entrent en contact et fusionnent, l'eau est partiellement isolée de l'air extérieur, la croissance se poursuit sur les marges et en surface là où il y a des exfiltrations d'eau (Fig. 2.5). La glace qui se forme est principalement une glace de ruissellement. Avec les cycles de gel-dégel hivernaux et printaniers, les cristaux de glace fondent et recristallisent pour former de gros cristaux sans orientation préférentielle (Fig. 2.6B, 2.6C, 2.6E et 2.6F). Des vides se créent à l'intérieur des structures de glace créant un réseau de microfractures (Fig. 2.6A, 2.6D, 2.6G et 2.6H). Tout comme l'ouverture de fractures à l'échelle d'une glace de paroi (Fig. 2.5D), il est probable que l'apparition de ces microfractures résulte des contraintes mécaniques internes induites par une diminution drastique de la température de l'air et de grandes variations de la température autour du point de fusion de glace (Gauthier 2008; Gauthier & al. 2012; Weiss & al. 2011). Le nombre élevé de vides produit durant cette métamorphose réduit la densité apparente de la glace et accroit sa porosité (Tab. 2.1). Un processus que les adeptes de l'escalade de glace nomment « pourrissement de la glace » (Gadd 2006). Cette métamorphose favorise les infiltrations de l'eau dans la structure, facilite les échanges de chaleur, accélère la fonte et provoque parfois l'effondrement partiel ou généralisé des structures de glace.

28

**Figure 2.5.** Croissance et superposition des accrétions et des stalactites de glace résultant du gel d'une chute d'eau de 75 m de hauteur, Corneille, glace de paroi #10, figure 1.3B (A) et d'une résurgence d'eau souterraine sur une falaise dynamitée de 15 m de hauteur, Les Barrières, glace de paroi #7, figure 1.3B (B). Couverture complète d'une falaise dynamitée, Les Barrières, glace de paroi #7, figure 1.3B (C) et ouverture d'une fracture dans la glace de paroi Les Barrières (D).
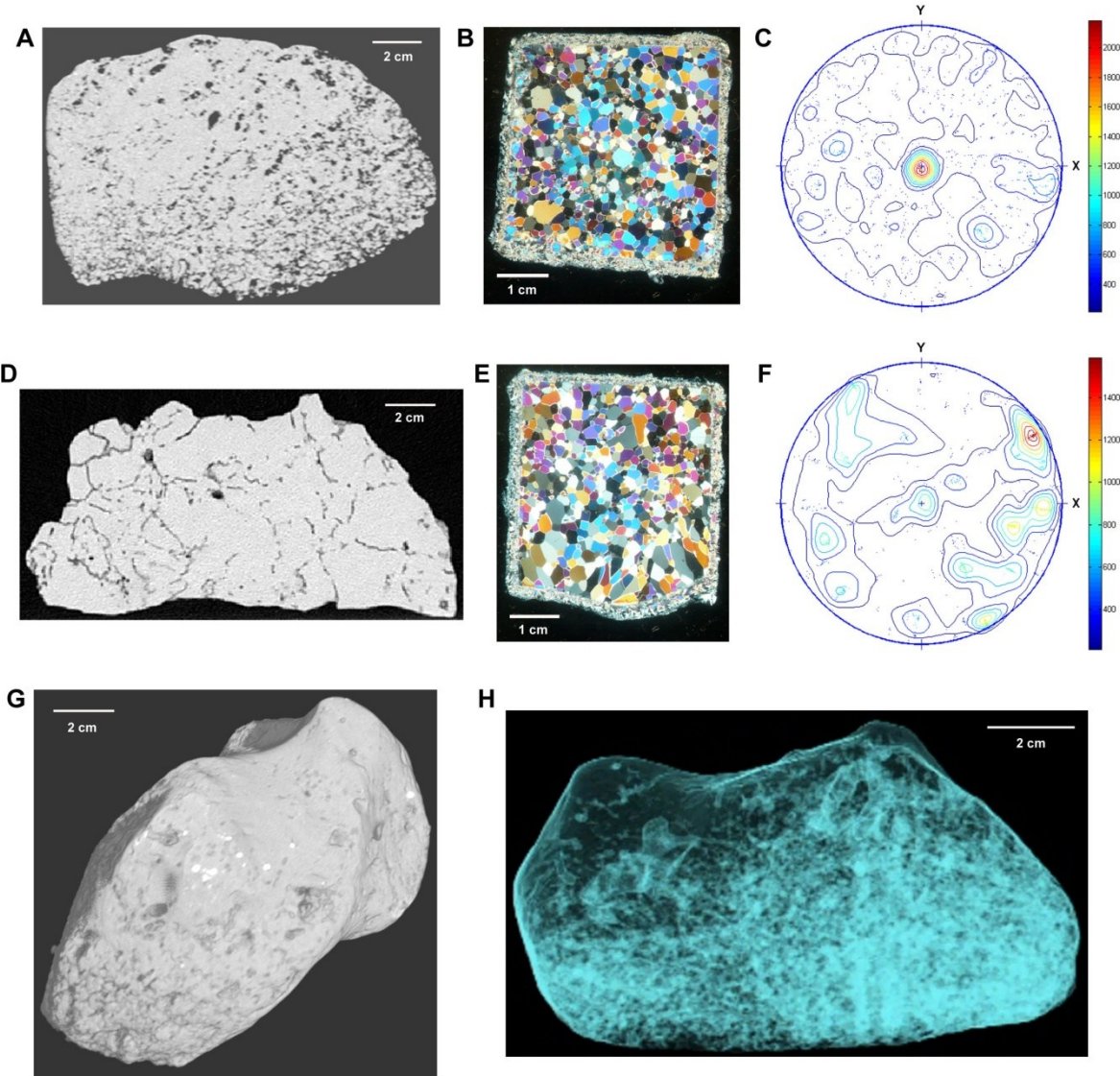
**Figure 2.6.** Morphologie, tomodensitométrie et microstructure de la glace de regel. Images tomodensitométriques : coupes perpendiculaire (A) et transversale (D) bidimensionnelle (2D), image tridimensionnelle (3D) surfacique (G), image 3D volumique (H). Photographie des cristaux de glace sous lumière polarisée, coupe perpendiculaire (B) et coupe transversale (E). Diagrammes de Schmidt (pole) des orientations préférentielle des axes C des cristaux de glace, coupe perpendiculaire (C) et coupe transversale (F).

N.B. : Sur les images tomodensitométriques 2D, les zones sombres ont des valeurs d'unité Hounsfield (HU) très faibles (environ -1000 HU), ils représentent des vides (bulles d'air) dans la structure de glace. Sur les images tomodensitométriques 3D volumiques, les lignes de contour clair représentent des changements abrupts de la densité (contours de la structure externe et bulles d'air endogènes). Les couleurs des photographies sous lumière polarisée croisée exposent la valeur d'orientation de l'axe C des cristaux de glace. Sur les diagrammes de Schmidt, chaque point est la projection de l'orientation de l'axe C d'un cristal de glace (à partir de chaque pixel de la photographie).

## 1.5. AUTRES STRUCTURES DE GLACE

Lorsque les sites de formation des glaces de paroi sont exposés à des conditions météorologiques instables (exposition au vent), la croissance des accrétions et des stalactites de glace peut mener à la formation de structures de glace inusitées comme les « méduses » et les « parapluies » (Fig. 2.7). Ce ne sont pas des formations de glace fréquemment rencontrées. Des conditions hydrologiques et météorologiques particulières sont requises. L'orientation et la morphologie de la falaise doivent favoriser la formation de tourbillons de vent et permettre le soulèvement des gouttelettes d'eau (Fig. 2.7A). La genèse de ces formes débute avec une croissance humide de petites accrétions. L'excédent d'eau est évacué par gravité de la surface de l'accrétion et participe à la formation de stalactites de glace sous la structure. L'exposition des structures au vent favorise une croissance oblique des stalactites (Fig. 2.7C). Éventuellement, ces derniers se joignent pour former des stalactites de glace à plusieurs branches que les glaciéristes nomment « mains de glace » ou « méduses » (Fig. 2.7B). Si l'apport en eau libre est toujours disponible, la croissance se poursuit et les méduses se rejoignent pour former des structures de glace circulaires et creuses qui prennent la forme de « parapluies de glace » (Fig. 2.7D).

**Figure 2.7.** Formation d'une glace de paroi située entre La Martre et Marsoui : tourbillon de vent à la chute d'eau Méduse et formation d'accrétions de glace (A), formation de stalactites de glace recourbées (B), formation des « mains ou méduses de glace » (C), et formation des « parapluies de glace » (D).

## 2. CLASSIFICATION DES GLACES DE PAROI ET MACROSTRUCTURES

Les glaces de paroi regroupent tous les types ou structures de glace se formant sur une paroi rocheuse verticale ou sub-verticale (Fig. 2.8). Elles peuvent être classifiées en fonction de deux critères hydrologiques simples (Bianchi 2004; Gauthier 2008; Gauthier & al. 2012; Gauthier & al. 2013). 1) Les carapaces de glace sont issues du gel d'une résurgence d'eau souterraine ou hypodermique sur une falaise (Fig. 2.9). Ce type de ruissellement sur une falaise est parfois discontinu ou intermittent à l'échelle annuelle. Le débit d'eau entrant sur la falaise est limité par le potentiel d'écoulement hydrogéologique. 2) Les cascades de glace sont issues du gel d'une chute d'eau sur une falaise (Fig. 2.9). Ce sont des écoulements permanents où l'eau est canalisée par un bassin versant dans un système fluvial bien défini : un petit torrent, un ruisseau, une rivière. Le débit hydrique sur la falaise est proportionnel à la taille du bassin versant et il est généralement supérieur à celui des résurgences d'eau souterraine.

La croissance et la fonte de ces deux types de glaces de paroi sont distinctes. La formation des cascades de glace débutera généralement avec la formation d'accrétions et de stalactites de glace en marge de l'écoulement principal (Fig. 2.7). Si le débit décroit suffisamment, une couverture complète de glace peut se former et isoler complètement l'écoulement de l'environnement extérieur. L'augmentation du débit au printemps est une étape importante dans le processus de fonte et de démantèlement de la structure de glace (Fig. 2.9) (Gauthier 2008; Gauthier & al. 2012).

La formation des carapaces de glace débute dès les premiers gels automnaux. Des pellicules, stalactites et accrétions de glace se forment partout où l'eau est disponible sur la surface de la paroi rocheuse (Fig. 2.10). Après quelques jours avec des températures de l'air inférieures à 0°C, toute la surface de la paroi rocheuse où il y a du ruissellement est recouverte de glace. Si la source de ruissellement hydrogéologique ne se tarit pas durant l'hiver, la croissance se poursuit. Puisque la glace recouvre l'ensemble de la paroi rocheuse, le ruissellement, sous forme d'une fine pellicule d'eau, se poursuit entre la glace et la paroi rocheuse aux endroits où la glace n'est pas directement ancrée (gelée) sur la falaise. À de nombreux endroits et à plusieurs reprises au cours de l'hiver, des exfiltrations d'eau font surface et participent au processus de croissance de la carapace (Fig. 2.10). Au printemps,

la hausse des températures initie la fonte et des fluctuations marquées de la température de l'air favorisent la fracturation de la masse de glace (Fig. 2.10) (Gauthier 2008; Gauthier & al. 2012; Montagnat & al. 2010; Weiss & al. 2011). Éventuellement, toute la structure de glace s'effondre avant d'avoir subi une diminution significative de son volume.

Les glaces de paroi peuvent également être classifiées en fonction de deux critères mécaniques (statiques) relatifs à la géomorphologie de la falaise et leurs structures (Fig. 2.8) (Bianchi 2004; Montagnat & al. 2010; Weiss & al. 2011). Les glaces de paroi autoportantes se forment au niveau d'une falaise surplombante (Fig. 2.11C et 2.11D). Deux situations sont possibles : une structure suspendue sans appui au sol (Fig. 2.11D et 2.11D) ou une structure colonnaire avec la base de la structure de glace reposant au sol (Fig. 2.11C et 2.12C). Les structures suspendues sont généralement composées d'un amalgame de stalactites de glace. Si la croissance se poursuit et rejoint le sol où des accrétions de glace se sont développées, une colonne (pilier ou chandelle) de glace est alors formée. Dans les deux cas, leur centre de masse est dirigé directement à leur base et leur stabilité repose essentiellement sur leur résistance mécanique interne. Ces structures présentent une stabilité précaire et sont sujettes à s'effondrer lorsqu'elles subissent des contraintes thermomécaniques importantes causées par des variations brutales de la température (Gauthier & al. 2012; Montagnat & al. 2010; Weiss & al. 2011).

Lorsque les glaces de paroi se forment sur des falaises verticales ou sub-verticales, une partie de leur masse est supportée par la falaise sous-jacente (Fig. 2.11A et 2.11B). Dans le cas d'une falaise présentant un profil irrégulier avec des saillies, certaines sections de la masse de glace peuvent adhérer à la surface rocheuse alors que d'autres présenteront les caractéristiques mécaniques d'une formation de glace autoportante (Fig. 2.11B et 2.12B). Lorsque la falaise présente un profil plus régulier avec une pente moins escarpée, l'ensemble de la surface de glace en contact avec la paroi rocheuse a le potentiel d'adhérer à la falaise (Fig. 2.11A et 2.12A). De telles dispositions structurelles sont beaucoup plus stables et moins susceptibles de s'effondrer lorsqu'elles sont soumises à des contraintes mécaniques internes importantes. Des fractures peuvent s'ouvrir, mais les surfaces de glace adhérente permettront à l'ensemble de la masse de glace de demeurer ancré sur la falaise (Fig. 2.5D et 2.10).
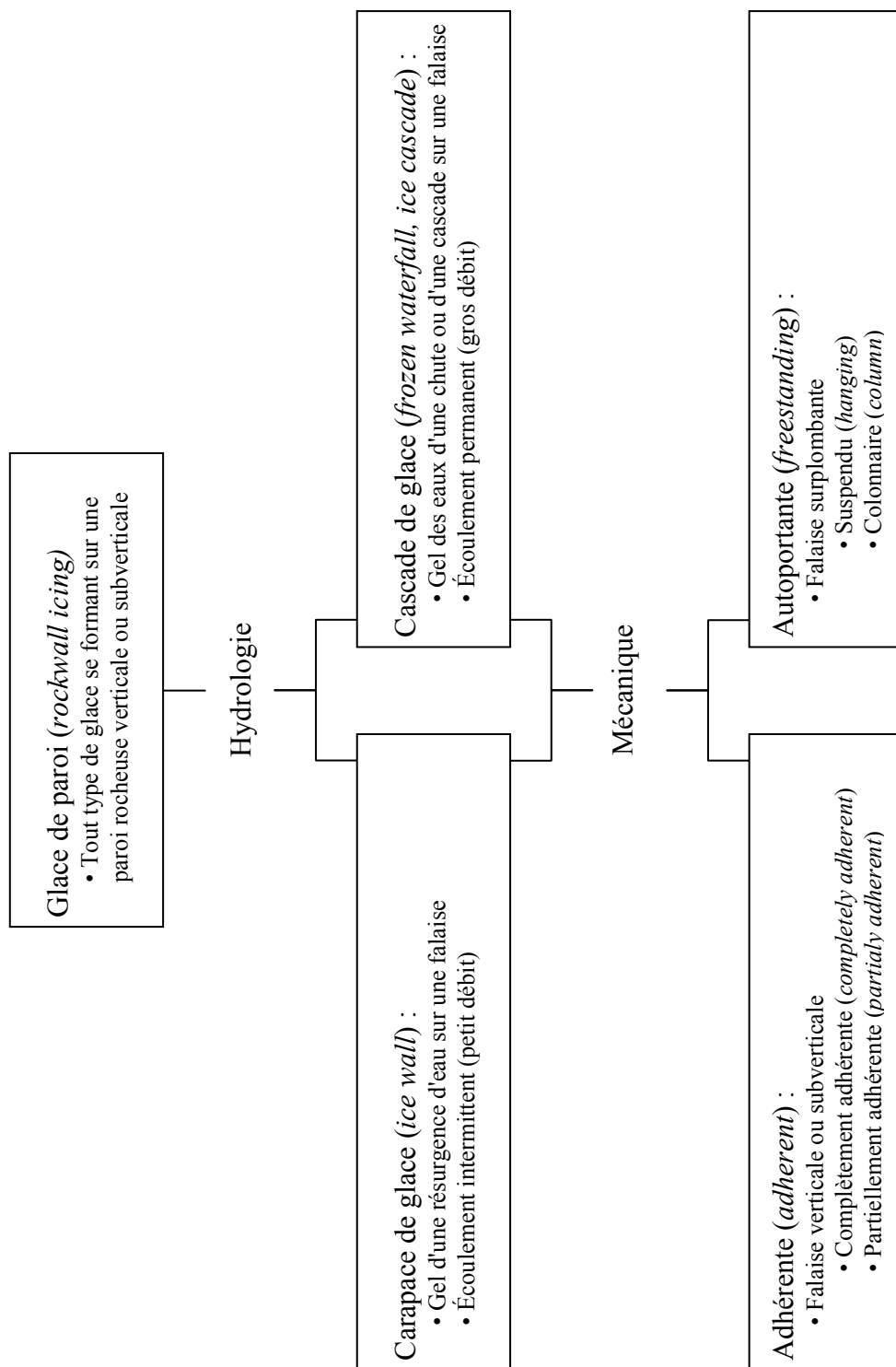
**Figure 2.8.** Classification des glaces de paroi en fonction de critères hydrologiques et mécaniques (statiques).

Glace de paroi (*rockwall icing*)
• Tout type de glace se formant sur une paroi rocheuse verticale ou subverticale

Hydrologie

Cascade de glace (*frozen waterfall, ice cascade*) :
• Gel des eaux d'une chute ou d'une cascade sur une falaise
• Écoulement permanent (gros débit)

Carapace de glace (*ice wall*) :
• Gel d'une résurgence d'eau sur une falaise
• Écoulement intermittent (petit débit)

Mécanique

Autoportante (*freestanding*) :
• Falaise surplombante
• Suspendu (*hanging*)
• Colonnaire (*column*)

Adhérente (*adherent*) :
• Falaise verticale ou subverticale
• Complètement adhérente (*completely adherent*)
• Partiellement adhérente (*partialy adherent*)

**Figure 2.9.** Carapace de glace (#11, Blue Stratos) versus cascade de glace (#10, Corneille).

36
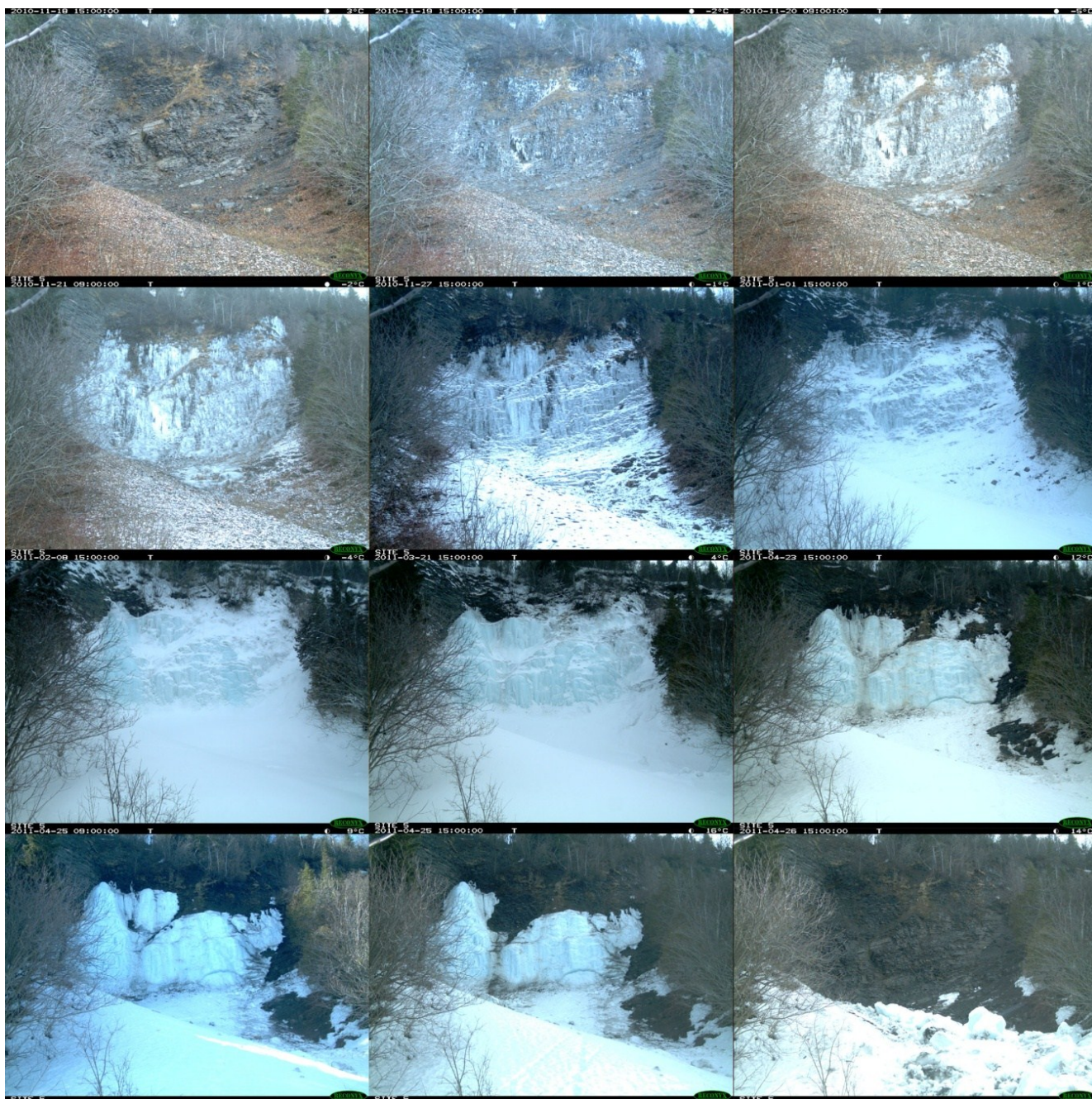
**Figure 2.10.** Suivi photographique de la carapace de glace #8 (G-Amphi), saison 2010-2011. De gauche à droite en partant du haut : 18/11/2010, 19/11/2010, 20/11/2010, 21/11/2010, 27/11/2010, 01/01/2011, 08/02/2011, 21/03/2011, 23/04/2011, 25/04/2011, 25/04/2011 et 26/04/2011.

**A** Complètement adhérente

**B** Partiellement adhérente

**Falaise verticale ou sub-verticale**

**C** Colonnaire

**D** Suspendue

**Falaise surplombante**
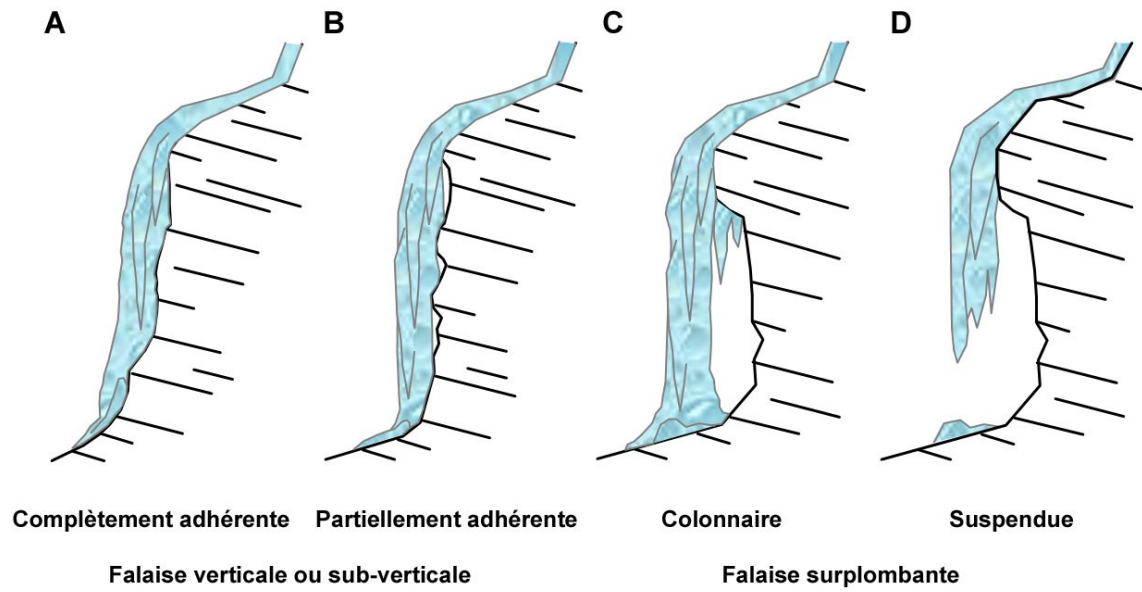
**Figure 2.11.** Classification des glaces de paroi en fonction de critères géomorphologiques et statiques.
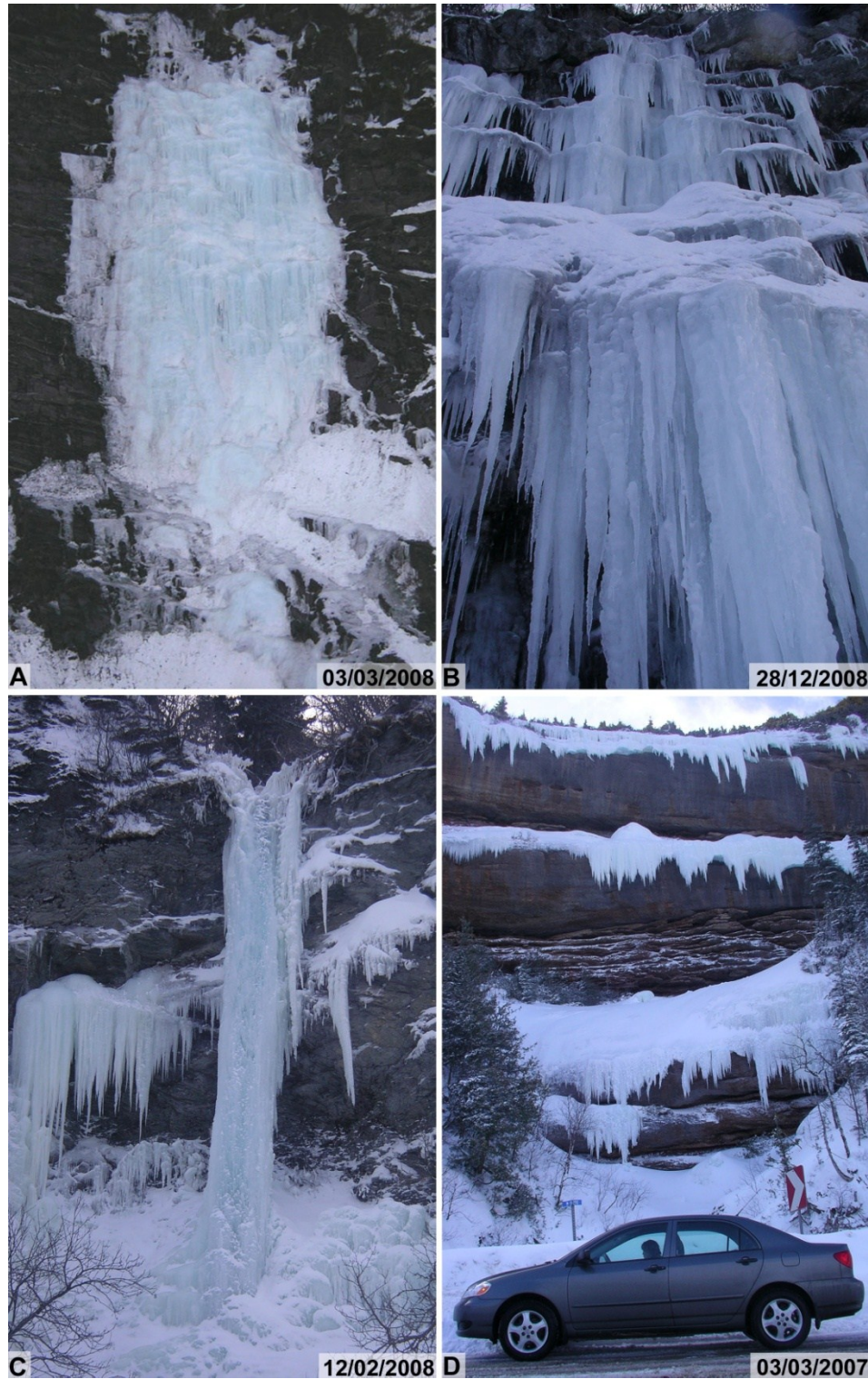
**Figure 2.12.** Quelques macrostructures : carapace de glace complètement adhérente (A), carapace de glace partiellement adhérente (B), cascade de glace colonnaire (C), carapaces de glace suspendues composées d'un amalgame de stalactites de glace (D).

## 3. CONCLUSIONS

La caractérisation des divers types de glaces constituant les glaces de paroi a permis de préciser leurs mécanismes respectifs de croissance. Leurs processus de formation, principalement celui des glaces de ruissellement et d'accrétion, devront être pris en compte lors de la modélisation de la croissance et de la fonte des glaces de paroi. Les critères hydrologiques utilisés dans l'élaboration d'une classification des divers types de glaces de paroi devront également être considérés dans le développement des modèles. Les processus de croissance, de fonte et de démantèlement des cascades et des carapaces de glace semblent suffisamment distincts pour être traités séparément. Par exemple, la croissance et la fonte de ces deux types de glaces de paroi semblent étroitement liées aux variations de la température de l'air, mais celles des cascades de glace semblent également soumises aux variations saisonnières du régime hydrologique. Cette différenciation et celle d'ordre mécanique entre les structures autoportantes et adhérentes devront également être considérées dans l'élaboration d'une méthode d'évaluation du risque de chutes de blocs de glace provenant du démantèlement des glaces de paroi.

40

# CHAPITRE 3: ICE CASCADE GROWTH AND DECAY: A THERMODYNAMIC APPROACH

Francis Gauthier, Maurine Montagnat, Jérôme Weiss, Michel Allard et Bernard Hétu

**Résumé :** Un modèle thermodynamique a été développé pour étudier l'évolution du volume de glace d'une chute d'eau gelée (ou cascade de glace). Le modèle a été élaboré à partir des données hydrométéorologiques recueillies à proximité et validées à partir de mesures du volume de glace estimées à partir d'images acquises au LiDAR terrestre. La cascade de glace se forme sur une falaise de 45 m de hauteur située dans le nord de la Gaspésie (Québec, Canada). La croissance de la cascade de glace peut être divisée en deux étapes. Pendant la première phase, la croissance est principalement contrôlée par la convection de l'air en contact avec l'eau chutant de la falaise. Durant la seconde phase, la cascade de glace recouvre toute la surface rocheuse et l'eau est isolée de l'environnement extérieur. La chaleur est évacuée de l'eau à travers le couvert de glace par conduction. La croissance est alors contrôlée par les variations journalières du bilan radiatif. Au printemps, l'augmentation du flux de chaleur sensible associé à la hausse du débit et le rayonnement solaire reçu à la surface de la glace durant le jour initie et provoque la fonte de la cascade de glace.

**Abstract :** The ice volume evolution of a frozen waterfall (or ice cascade) was studied using a thermodynamic model. The model was developed from meteorological data collected in the vicinity of the waterfall and validated from ice volume measurements estimated from terrestrial LiDAR images. The ice cascade forms over a 45 m high rockwall located in northern Gaspésie, Québec, Canada. Two stages of formation were identified. During the first stage, the growth is mainly controlled by air convection around the flowing and freefalling water. The ice cascade growth rate increases with the decreasing air temperature below 0°C and when the water flow reaches its lowest level. During the second stage, the ice cascade covers the entire rockwall surface, water flow is isolated from the outside environment and ice volume increases asymptotically. Heat is evacuated from the water flow through the ice cover by conduction. The growth is controlled mainly by the conductive heat loss through the ice cover but also by the longwave radiation emitted at the ice surface during the night. In spring, melting of the ice cascade is dependent upon the air convection over the ice surface but also by the sensible heat carried by the increasing water flow and the solar radiation received during the day.

# 1. INTRODUCTION

In northern Gaspésie (Eastern Canada), the regional road is enclosed between a series of relatively high rock walls and the Saint-Laurence estuary. On those cliffs, many waterfalls lead to the formation of ice cascades during the cold season. Each spring, an important number of ice-blocks falls presenting a traffic hazard is reported by the Quebec department of transport (MTQ) (Gauthier 2008; Gauthier & al. 2012; Girard & Hétu 1994; Hétu & al. 1994). Additionally, with the increasing interest for mountaineering and ice climbing in North America, the number of traumatisms reported since 1951 also increased (American and Canadian Alpine Club 1999). Of the 200 to 400 accidents reported each year, 20% were caused during the practice of ice climbing. Although the mechanical (in)-stability of vertical ice cascades has been recently studied in the Alps (Weiss & al. 2011), a better understanding of this natural hazard is still needed.

Recent studies show that air temperature is certainly the main variable controlling the growth and decay of ice cascades (Gauthier 2008; Gauthier & al. 2012; Montagnat & al. 2010). The statistical models developed by Gauthier (2008) and by Gauthier & al. (2012) to predict ice-block falls along the northern Gaspésie road (Eastern Canada) show that rising air temperatures above the melting point is the main variable controlling the ice cascades melt and collapse processes. The model based on melting degree-days calculation yields acceptable correlation coefficients with the occurrences of ice block falls. Montagnat & al. (2010) proposed a simple conductive heat flux model to quantify the evolution of a frozen waterfall of the French Alps. Their model is based on the crude assumption that the water is slowly flowing between the growing ice cover and the rockwall surface. However, observations show that the growth dynamics is much more complex. Ice cascade formation begins first with the growth of a multitude of independent ice stalactites (Gauthier 2008; Gauthier & al. 2012; Montagnat & al. 2010) and with the formation of ice accretions caused by the freezing of water spray around the main water flow (Gauthier 2008; Gauthier & al. 2012). These observations show that the growing and melting processes result from a complex mix of processes common to ice stalactites (e.g. Knight 1980; Laudise & Barns 1979; Maeno & al. 1994b; Makkonen 1988; Short & al. 2006), icings (aufeis) growth (e.g. Hu & al. 1999; Schohl & Ettema 1986; Schohl & Ettema 1990), ice accretions similar to freezing rain accumulation (e.g. Jones 1996; Makkonen 2000) and frazil ice formation (e.g.

Andres 1995; Hanley & Michel 1977; Osterkamp & Gosink 1983; Ye & Doering 2004). Energy balance assessments of those superficial ice formations have already been elaborated by the cited authors, but no specific model has yet been proposed for assessing parameters and simulating the growth and decay of ice cascades.

In this paper, we focus on hydrometeorological data collected around an ice cascade and we propose a two-stage growth and decay model based on observations and data analysis. We are not considering the mechanical destabilization that frequently occurs during large and rapid temperature changes as the results of thermal stresses (Weiss & al. 2011). Instead, we propose an energy balance model based on, and developed from, a large amount of hydrometeorological data collected around a typical north facing ice cascade. It was calibrated from ice volume measurements made from a series of terrestrial LiDAR images. The model clarifies the role of the different heat transfer components involved in ice cascade growth and decay. The following questions are addressed: Is the conductive heat flux coming from the rockwall a major source of heat? Does latent heat flux (evaporation and sublimation) play a significant role in ice cascade thermodynamics? Does all the ice produced in the flowing and free falling water stay in the ice cascade system? Is the sensible heat brought by the flowing water a major energy flux? Does the radiation heat budget play a significant role in the ice cascade growth and decay process? The main objectives of this study are to identify the growth and decay mechanisms, to evaluate the importance of the different heat fluxes controlling the ice cascade growth and decay, and to improve our general understanding of this complex system.

## 2. LOCATION

Field work was done during the 2010-2011 winter on an ice cascade named "Le Voile de la Mariée" (G-Voile) located along the north shore of the Gaspé Peninsula in eastern Canada (Fig. 3.1). The climate of the region is cold temperate with a strong maritime influence. The average daily minimum and maximum temperature in January is -16.1°C and -7.2°C respectively (Environnement Canada 1971-2000; Gagnon 1970). The maritime influence of the Gulf of St. Lawrence provides an average rainfall of about 1000 mm spread evenly throughout the year. One third of this precipitation falls as snow from mid-November to late April. Liquid precipitation during fall is also relatively high with about 200 mm for

October and November. Along the coast, the rockwalls are strongly affected by the wind with only 14% of calm days per year and with a wind speed frequently exceeding 50 km/h (Gagnon 1970; Hétu & Vandelac 1989).

The ice cascade forms on a 45 m high, north facing ($354^{o}$) and almost vertical rockwall (angled at about $80^{o}$) mainly composed of stratified shale, limestone and sandstone (Brisebois & Nadeau 2003). The ice cascade does not show free standing structures such as suspended ice structure or ice column. The water comes from a small stream draining a 1.8 $km^2$ catchment. The mean winter discharge of the stream is around 14 L/s but drops to 6-7 L/s in January and February. The peak event arises during the melt season (over 250 L/s in May 2011).
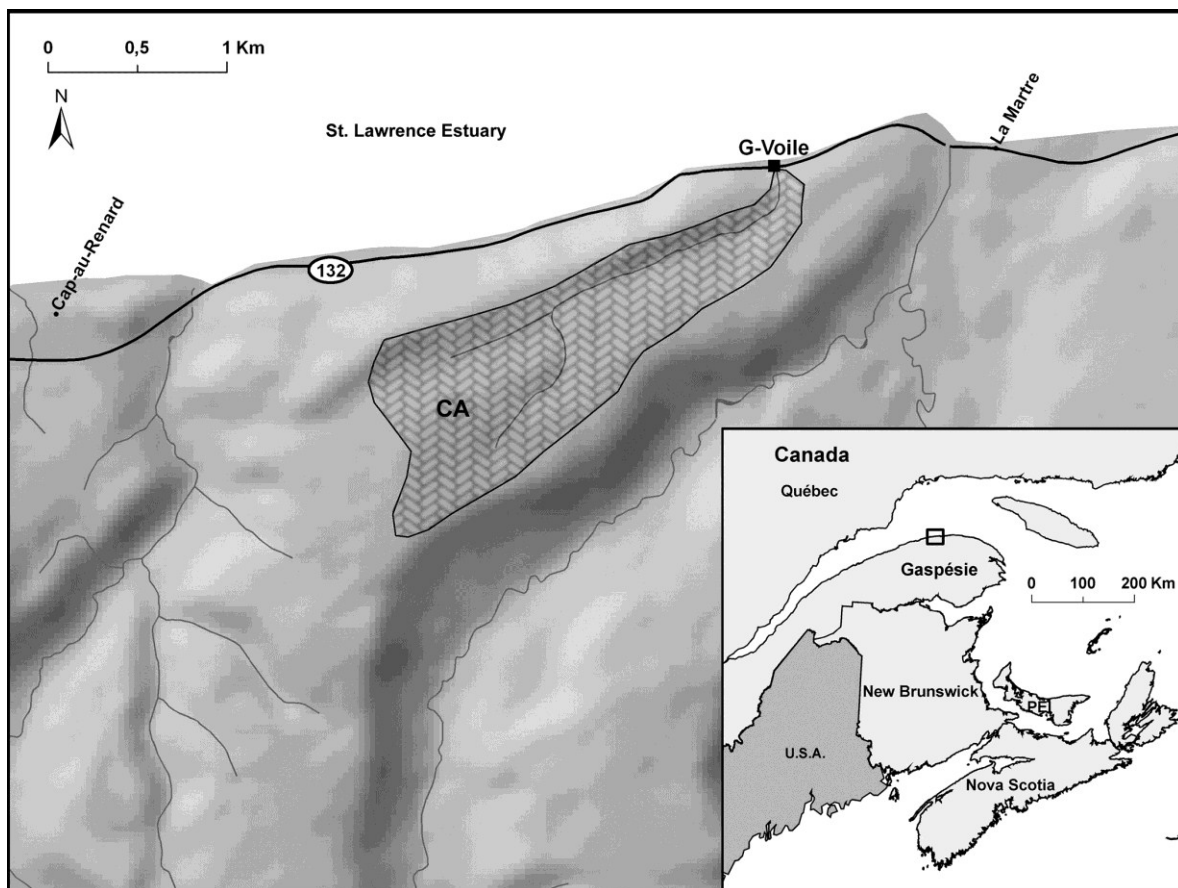


**Figure 3.1.** Location of the "Voile de la Mariée" ice cascade (waterfall) and its catchment (CA).

## 3. MEASUREMENTS

All the different instruments were installed during summer 2009 and tested during winter 2009-2010. The final set up was completed during summer 2010 and the measurements were conducted during the 2010-2011 cold season, from early October to the end of June. Instantaneous measurements were sampled every 10 minutes but we used hourly mean values for data analysis and to develop the model.

### 3.1. INSTRUMENTATION

Two independent and automatic weather stations (Onset: HOBO Micro Station Data Logger, H21-002) were set up around the ice cascade. The first one (WS1) was located at the top of the waterfall (Fig. 3.2). The air temperature, relative humidity, air pressure, precipitation, and solar radiation were measured with a 12-bit Temperature/RH Smart Sensor (S-THB-M002), a Barometric Pressure Smart Sensor (S-BPB-CM50), a 0.2 mm Rainfall Smart Sensor (S-RGB-M002), and a Solar Radiation Sensor (Silicon Pyranometer, S-LIB-M003). The pyranometer was set up at the same vertical angle and orientation as the ice cascade. Its measurement range is from 0 to 1280 $W \cdot m^{-2}$ across a spectral range of 300 to 1100 nm.

The second station (WS2) was located about 50 m east from the middle of the waterfall and at about 4.5 m from the rockwall. The windspeed and rockwall temperature were measured with a Wind Speed and Direction Smart Sensor (S-WCA-M003) and three 12-Bit Temp Smart Sensors (S-TMB-M017). The temperature sensors were fixed on the rockwall surface and embedded 38 cm and 80 cm deep into the rock.

Water pressure and temperature were measured at the top and bottom of the waterfall with two HOBO U20 Water Level Data Loggers (U20-001-04). Unfortunately, the pressure sensor at the foot of the waterfall did not produce reliable data because it was displaced by a storm surge on December 2010. The water temperature measurements were still valid, but the sensor was located about 10 m away from the foot of the waterfall. Air pressure was subtracted from the water pressure measurements. As proposed by The Federal Office of Metrology (METAS), we took into account an altitude air pressure correction factor of the form:

$$P_{wll} = P \left( \frac{(T+0.0065H)}{T} \right)^{5.2561} \tag{3.1}$$

where $P_{wll}$ is the atmospheric pressure at the water level height (Pa), P is the atmospheric pressure at the barometer (Pa), T is the air temperature ($^{o}$C), and H is the height difference between the water level logger and the barometer. The corrected water pressures were then used to develop a discharge calibration curve.

## 3.2. DISCHARGE MEASUREMENTS

Discharge measurements were made using the slug salt injection method (Moore 2005). We used 1 kg of salt diluted in 900 ml of water. The solution was dumped about 50 m upstream from the cascade. Less than 1 m from the top of the waterfall, we measured the electrical conductivity of the stream water using a YSI Handheld Multiparameter Instrument (YSI 556 MPS). All measurements were calibrated to determine the relation between the relative salt concentration and the water electrical conductivity. Moore (2004b, 2004b, 2005) provides a more detailed description of the method.

Under suitable conditions, streamflow measurements made by slug injection can be accurate at about ±5% (Day 1976; Moore 2005). Twenty two measurements were made during the study (between October 2010 and June 2011); 2 to 3 times a month depending on the discharge fluctuation. Four measures had to be eliminated because mistakes were committed during handling. The 16 reliable discharge measurements were kept, ranging from 2.0 to 215.1 L/s, to build the calibration curve (Fig. 3.3). A second-order polynomial relation was the best fit. It is important to note that above the maximum discharge value (215.1 L/s), the calibration curve certainly over estimates the discharge value. However, as the peak discharge comes after the complete melting of the ice cascade, this extrapolation does not affect the results presented in this paper.
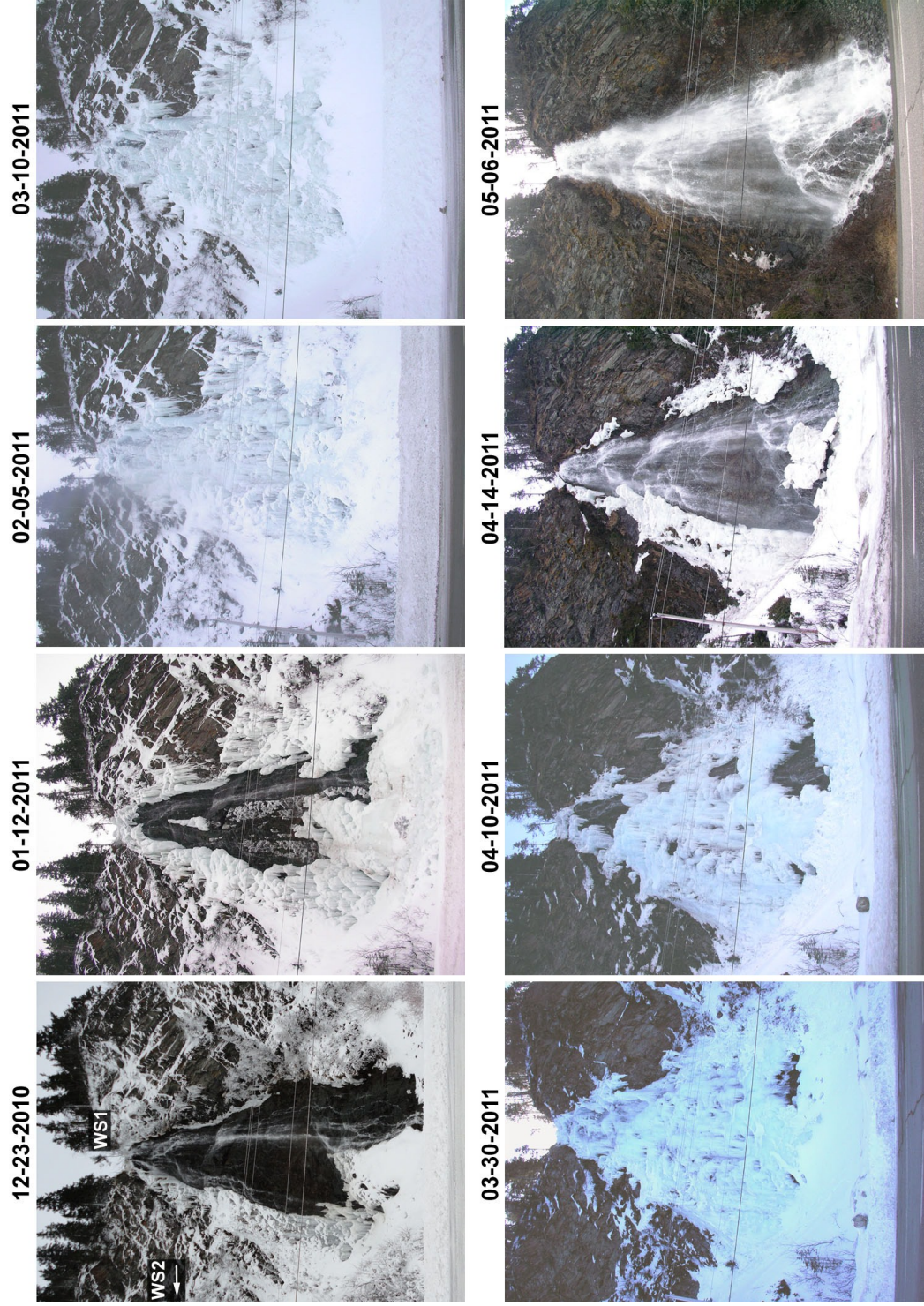
**Figure 3.2.** Ice cascade evolution between December 23$^{rd}$ 2010 and May 6$^{th}$ 2011. Positioning of the weather stations (WS1 and WS2).

47
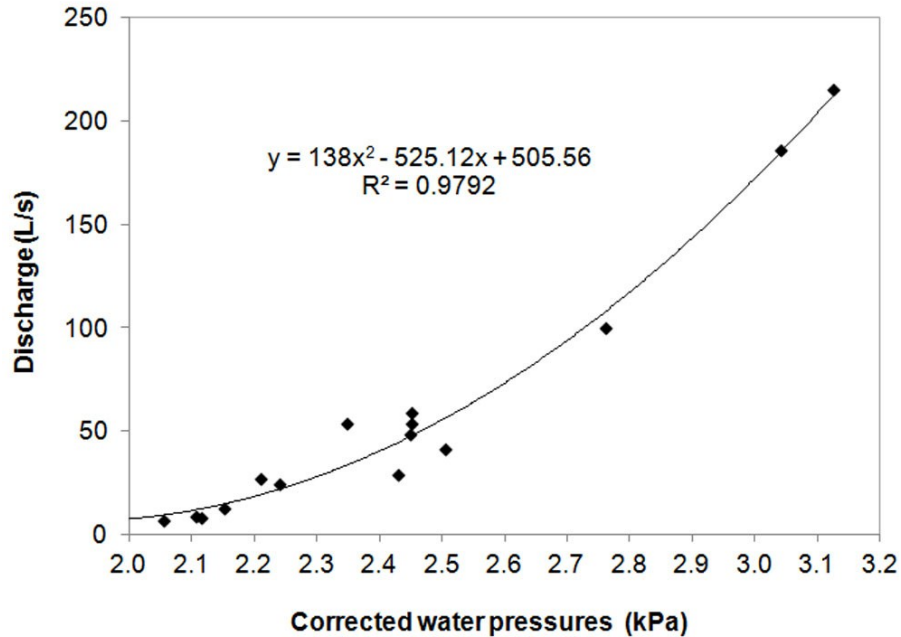
**Figure 3.3.** Discharge calibration curve.

## 3.3. ICE VOLUME EXTRACTION

Ice volume changes due to accretion and decay were estimated using terrestrial LiDAR measurements. The scans were performed using a Leica Scan Station 2. We first scanned the rockwall (waterfall) surface in September 2010 when the water discharge was at its lowest level. Afterward, 11 scans were performed during the ice cascade growing and melting season. The scanner works up to 300 m for a surface albedo of 0.9 and 134 m for a surface albedo of 0.18. The scans were performed at a distance of 30 m from the base of the ice cascade and about 60 m from the top. The laser beam did not penetrate the dry, relatively porous and irregular ice cascade surface as shown by the absence of scatter in the point measurements at the ice surface. The laser beam diameter is about 4 mm and the maximum sampling density is less than 1 mm. The accuracy of the LiDAR is 4 mm in distance and 6 mm in positioning if located at less than 50 m from the scanned surface. The scans were performed using a 5 mm resolution at a distance of 45 m.

The next step consisted in developing high-resolution triangulated irregular network models (HRTINM) from the LiDAR measurements. The HRTINMs were developed using the

Leica Geosystems Software Cyclone 7.1. The registration function in Cyclone was used to merge the point cloud together into the same field of coordinates. The use of 5 fixed survey targets allowed an overlapping precision of less than 5 mm. For a better consistency between HRTINMs, the point clouds were resampled at a 20 mm resolution. We were also forced to trim the HRTINMs to eliminate the bordering vegetation and the snow accumulation at the foot of the ice cascade. Doing so, the calculated ice volume does not represent the total ice accumulation but rather a lower estimate (probably between 80 to 90%). The same surface area was extracted from each HRTINM. At the end, we extracted the HRTINMs volume using the function Mesh Volume in Cyclone 7.1. The given volume is the difference between the HRTINMs and a reference plan (Fig. 3.4). The HRTINMs generated from the September 2010 LiDAR measurements was used as the reference surface topography. The extracted volume from this reference surface was then subtracted from the other calculated volumes. The differences represent the ice volume accumulation at the time of the scan. For a more detailed description of the method, see Rabatel and others (2008) and James and others (2006).

The total uncertainty ($\sigma_{tot}$) can be estimated as follows (Baltsavias 1999; Rabatel & al. 2008):

$$\sigma_{tot} = \sqrt{\sigma_1^2 + \sigma_2^2 + \sigma_3^2 + \sigma_4^2} \tag{3.2}$$

where $\sigma_1$ to $\sigma_4$ represent the different independent processing errors. $\sigma_1$ is the error inherent to the LiDAR itself. $\sigma_2$ is the error in the development of the HRTINM. It corresponds to the point cloud resolution chosen to generate the HRTINM: 20 mm in our case. $\sigma_3$ is the error in the point cloud merging (overlapping) process (5 mm). $\sigma_4$ represents the errors related to the scan surface itself and to the environment. Because of the good climatic conditions during the scanning acquisition process, except for the December 10th scans, the error related to the environment is certainly negligible. On December 10th, a light snowfall reduced the quality of the acquired point cloud image. Many points representing snowflakes had to be removed before the generation of the HRTINM. The few remaining points, too close from the ice surface to be removed, caused a slight overestimation of the ice volume. Furthermore, the error associated with the scan surface is difficult to estimate.

Even if the ice cascade surface was generally dry, some limited zones were lubricated by localized flow on the ice surface. The point cloud resolution over these wet zones was not as high as on the remaining surface. It locally affected the size of the mesh, but we were unable to estimate the exact error associated with this phenomenon. This lead to a minimum uncertainty of 22 mm over the trimmed surface area. This represents a absolute error of 6.5 $m^3$ on the calculated ice volumes or 115% of the smallest calculated ice volume (5.5 $m^3$ on November 26th 2010) to 2.8% of the largest calculated ice volume (231 $m^3$ on March 30th 2011).

The LiDAR measurement only leads to a precise reconstruction of the external shell of the ice cascade. It is not possible to estimate the volume of the voids between the ice cascade and the rock wall, especially if ice melting occurs at the ice and rockwall interface due to a positive sensible heat flux carried by the flowing water.

## 4. HYDROMETEOROLOGICAL CONDITIONS AND ICE CASCADE EVOLUTION

We focus here on the local hydrometeorological conditions in the vicinity of the ice cascade. We also relate the evolving conditions to the ice cascade volume evolution. Figure 3.5 shows the hydrometeorological data recorded during the study. Because the ice cascade is facing north, only diffuse radiation reaches the ice surface during winter. There is still a daily fluctuation, but its order of magnitude is pretty small (Fig. 3.5A). At the end of January (around day 65), the incoming diffuse radiation slowly rises. The waterfall slope aspect allowed a short period of direct solar radiation during late afternoon at the beginning of May, but at that time, the ice cascade has almost entirely disappeared already. Unsurprisingly, the relative humidity remains rather high during the cold months of winter and tends to decrease slightly when the temperature increases in spring (Fig. 3.5B). The wind conditions are almost never completely calm and the frequency of wind events with hourly mean values close or over 10 m/s (36 km/h) is high (Fig. 3.5B). We assume that the wind plays an important role in the sensible heat transfer at the water-air and ice-air interface. We also assume that relatively low humidity favours evaporation-sublimation and heat transfer to the air. Also, presumably, the slowly increasing incoming solar radiation shall transfer energy to the system.
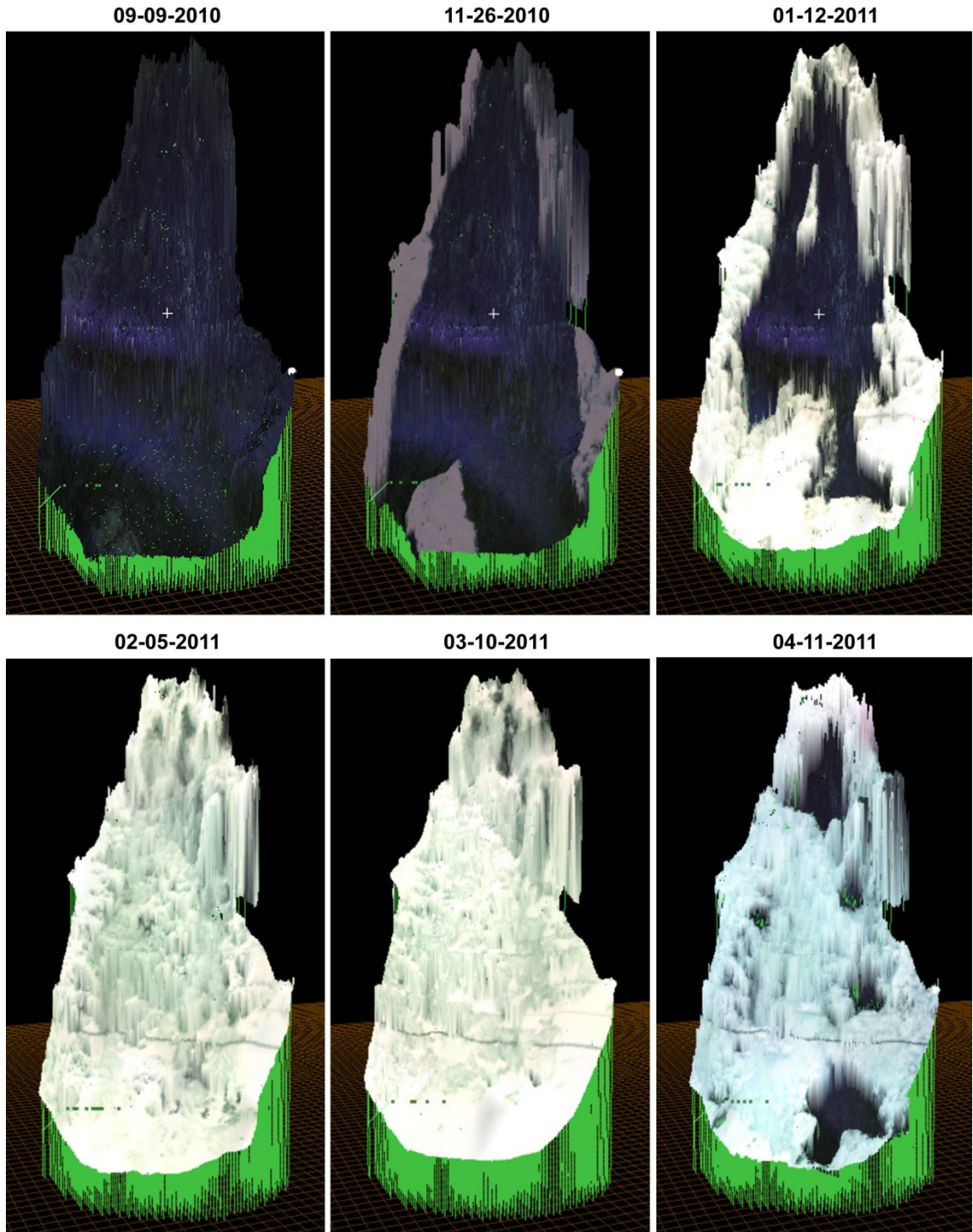
**Figure 3.4.** Computations examples of the volume of the ice cascade during the winter 2010-2011. The volume between the surface topography and the reference plan is computed for each survey date using the function Mesh Volume in Cyclone 7.1. The difference between volume calculation between surveys and the volume of the reference surface topography (09-09-2010) represents the changes in ice volume.

It seems clear, however, that the first sustained air temperatures below the freezing point control the beginning of the ice cascade growing process (Fig. 3.5C). For example, a period of four days (day 4 to 8) with air temperature below 0°C was sufficient to initiate the formation of ice structures on each side of the waterfall (Fig. 3.5C and the LiDAR image of November 26th 2010 on figure 3.4). On the other hand, a drastic increase in temperature around day 28-29 resulted in the melting of the young ice cascade. These observations suggest the calculation of a freezing or melting degree-hours parameter (FDH):

$$FDH = \int_{t_0}^{t} (T_f - T_a)\mathrm{dt} \tag{3.3}$$

where $T_f$ is the freezing point of water and $T_a$ the air temperature. The FDH has been calculated at an hourly time step (t), starting November 15th 2010 at 00h with a minimum value of 0. Similar calculations, but at a daily time step, were previously performed to model the growth of ice cascades in the French Alps (Montagnat & al. 2010) and also to predict the collapse of specific ice walls in Northern Gaspésie (Gauthier 2008; Gauthier & al. 2012). At the beginning of the growing process, FDH shows a significant lag with the measured ice volume accumulation rate (Fig. 3.5E). FDH also responds rapidly to air temperature variations. We think that the fragmentation of the water flow during its freefall increases convective heat transfer with the atmosphere. Under cold temperature (<0°C), ice formed on each side of the waterfall due to cold air convection around the freefalling water droplets, thus producing important ice accretion. When air temperature warms-up (>0°C), melting is controlled by air convection around the static ice formations, thus limiting the melting of ice. This imbalance between ice formation and melting could explain why the FDH does not adequately reproduce the initial growth and decay dynamics.

Although the water temperature is affected by air temperature variations, we cannot at this stage assert if the ice volume evolution is also dependent of these fluctuations. Most likely, the sensible heat flux carried by the flowing water will play a role in the global evolution of the ice cascade. Three ad hoc water temperature measurements made at the beginning of the growing process show that the water at the foot of the waterfall was in a supercooled state (between -0.01°C and -0.06°C ± 0.015°C) even when the air temperature was just below 0°C. These measurements are not in agreement with the bottom water temperature

presented in Figure 3.5C. We think that the logger was located too far away (~10 m) from the foot of the ice cascade to record this information. In steep stream systems, supercooled temperatures (usually with maximum value around -0.04$^o$C) are observed only in frazil production zones such as rapids or riffles (e.g. Stickler & Alfredsen 2009). At the foot of the 45 m high waterfall, a huge amount of frazil ice was observed but it was almost entirely evacuated by the current. Only a little amount of ice seems to accumulate on the branches and the rock structures located around the main water flow path. Ice accretions, similar to freezing rain accumulation (see Makkonen 2000), and ice stalactites are slowly growing on and under those structures (Fig. 3.2).

Even if the discharge is slowly decreasing during this period, the limited amount of liquid precipitation received continues to affect the stream flow, bringing more sensible heat to the system (Fig. 3.5D). But because the ice is mainly formed on the edges of the main waterfall flow, the slowly growing ice structures are not significantly affected by those fluctuations. On the other hand, snow fall events (e.g. 26 cm received on January 26$^{th}$, day 72) can presumably favour the growth process by lowering the water temperature. In this scenario, the melting snowflakes in the water flow might act as ice nuclei.

As soon as the air temperature is maintained under the freezing point of water and discharge reaches its base flow (around 6 to 12 L/s), the ice cascade forms rapidly (Fig. 3.2 and 5). The ice structures on the edges of the main flow gradually grow from the periphery inward to the center of the decreasing flow. Eventually, the ice covers the entire rock wall or waterfall surface. Even if the FDH index still shows a significant lag (around 10 days) with the ice volume evolution, indeed it follows the fast growing trend of the ice cover.

When the ice covers the entire waterfall area, the main water flow is isolated from the outer environment. There is still some external flow on the ice cascade, mainly by exfiltration, but it remains marginal and localized. Observations show that, between January 12 (day 58) and February 5$^{th}$ (day 82), ice formed over the entire waterfall (Fig. 3.2). The transition from a regime controlled by the air-water interaction to the complete isolation of the main water flow is fast (less than 6 days). Between January 18$^{th}$ and 23$^{rd}$ (days 54 to 69), the water temperature at the foot of the waterfall rose by nearly 0.4$^o$C from a supercooled state to +0.34$^o$C (Fig. 3.6). From January 21$^{st}$ (day 67), the water temperature continued to rise

even if the air temperature remained far below $0^o$C (Fig. 3.6). This is a sign that the ice outer shell is completely closed; the isolated water was no longer directly affected by the air temperature. It is important to mention that at the end of December, a deep snow cover had already covered the stream between the ice cascade foot and the location of our water level and temperature logger. Moreover, the only important snow falls in January occurred on the 22$^{nd}$ (day 68) with 12 mm of snow-water equivalent (WE) and the 26$^{th}$ (day 72) with an accumulation of 26 mm (WE). We believe that the only condition responsible for this temperature change is that ice completely covered the waterfall.

Because the ice cover is thin at the beginning of this transition stage, the ice volume accumulation remains substantial. But the growth rate decreases at the beginning of February. This asymptotic behavior had already been observed by Montagnat & al. (2010) on three frozen waterfalls in the French Alps. These observations suggest a transition between a growth dynamics controlled by convective heat exchange between water and the atmosphere to a dynamics where the heat is removed from the flow through the ice cover.

On March 12$^{th}$, 16$^{th}$ and 17$^{th}$ the air temperature rose above $0^o$C and liquid precipitation induced an increase of the discharge above the base level. The effect was not visible on the LiDAR measurement, but we noticed the formation of multiple voids between the ice shell and the rockwall. The ice cascade surface was still intact, but the ice volume suffered a clear and drastic decrease (see the grey arrow, Fig. 3.5). Numerous little holes opened in the ice cascade (see the ice cascade picture taken on March 30$^{th}$ and on April 10$^{th}$, Fig. 3.2). After those events, the air temperature fluctuated around the melting point and the water discharge increased. The ice cascade rapidly melted. And finally, the major rain event of April 5$^{th}$ resulted in a rapid increase of the stream discharge. This sequence of events resulted in a radical dismantling and collapse of the ice cover between April 10$^{th}$ and 14$^{th}$.
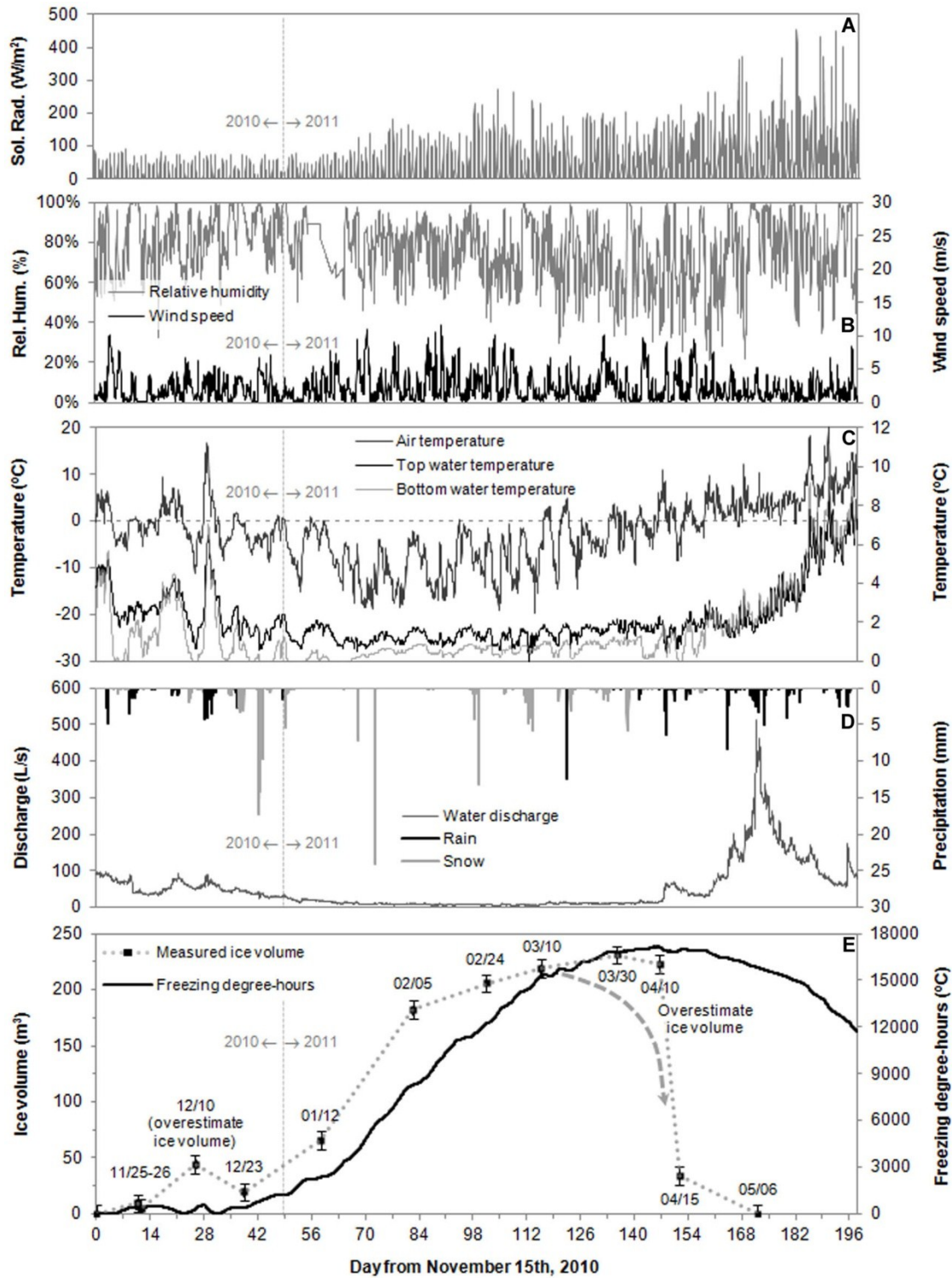
**Figure 3.5.** Global solar radiation (A), wind speed and relative humidity (B), air and water temperatures (C), precipitation and water discharge (D), freezing degree-hours and measured ice cascade volume (E) from November 15th 2010 (day 0) to may 31st 2011 (day 197). N.B.: The gray dashed arrow represents a more probable ice volume evolution.
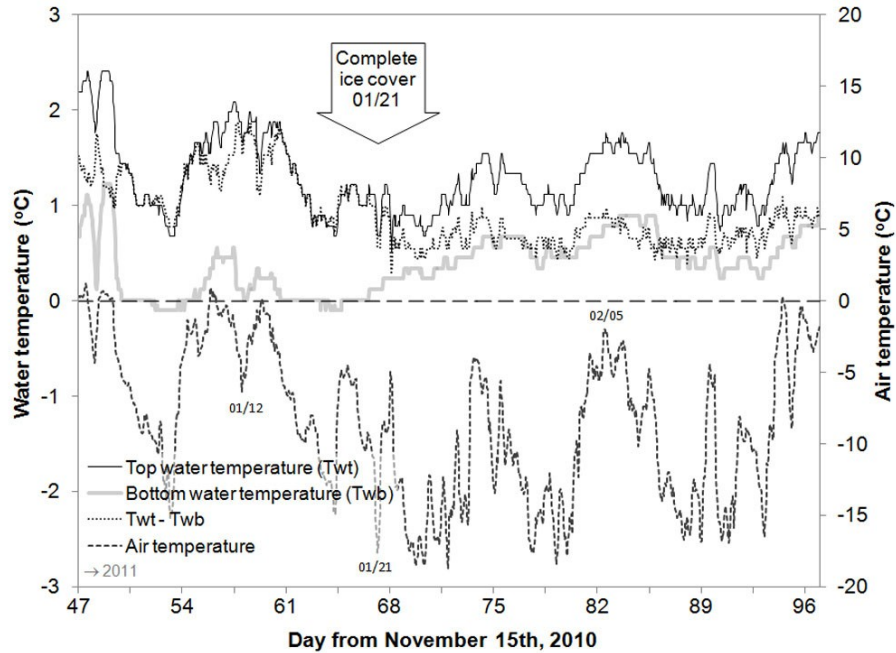
**Figure 3.6.** Air and water temperature evolution during the growing transition phase: from January 1st 2011 (day 47) to February 10th 2011 (day 87).

## 5. MODELLING

The ice cascade growth and decay process is controlled by a series of complex and highly fluctuating factors. The atmospheric conditions (air temperature, radiation and evaporation) affect heat transfers in many directions: from the flowing water and the ice surface to the ambient air, and from the rock wall to the forming ice cascade. Additionally, water temperature, precipitations, discharge, stream flow velocity and their spatial distribution over the rockwall all play a role in the formation of the ice cascade. To better understand the role played by each of these variables, a thermodynamic model (model 1) was designed based on the crude assumption that the water is flowing over an ice cascade fixed to a vertical rockwall (Fig. 3.7). The different components of the energy balance are transferring heat to or from the water flow at a temperature close to the freezing point. As shown below, this model strongly overestimates the amount of ice produced over the cold season. Therefore, we developed a two-stage model (model 2) where the transition from a regime controlled by the air-water interaction to a regime where the isolation effect of the ice-cover is taken into account.

56

## 5.1. MODEL 1

This model is based on energy budget and it applies theoretical considerations inspired mainly by ice stalactites growth models (e.g. Maeno & al. 1994b; Makkonen 1988), river ice and icing growth models (e.g. Ashton 1989; Hu & al. 1999; Schohl & Ettema 1986), ice accretions accumulation models (e.g. Jones 1996; Makkonen 2000) and frazil ice production models (e.g. Hanley & Michel 1977; Ye & Doering 2004). The various heat fluxes associated with water flowing down a vertical and simplified plane (the rock-wall) are presented in Figure 3.7. At any time during the freezing or melting process the energy balance can be written as:

$$0 = Q_{cv} + Q_{evap} + Q_{cc} + Q_{rad} + Q_w + Q_{ice} \tag{3.4}$$

where $Q_{cv}$ and $Q_{evap}$ are the sensible and latent heat flux at the air-water interface, respectively. $Q_{rad}$ is the radiative heat budget. $Q_{cc}$ is the heat brought by conduction from the rockwall to the ice cascade. $Q_w$ is the sensible heat carried by the flowing water and $Q_{ice}$ is the latent heat released during the ice production process (phase change). In this model, we assume that the flowing water around the forming ice is at the freezing point.
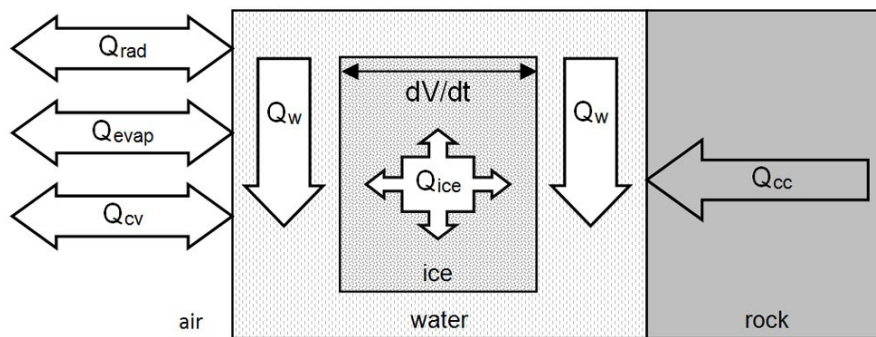


**Figure 3.7.** Schematic illustration of an ice cascade growth and decay model (model 1).

### 5.1.1. Sensible and latent heat flux

As the water falls down on and over the rockwall, air convection around the flow and the falling droplets evacuate or bring energy to the water. The convective heat transfer between the air and the water can be expressed by:

$$Q_{cv} = h_{wa}(T_a - T_f) \tag{3.5}$$

where $h_{wa}$ is a heat transfer coefficient which depends on meteorological conditions, especially the wind speed. The difficulty in determining $Q_{cv}$ is, in fact, in determining $h_{wa}$. The option often taken is to use a bulk aerodynamics approach (e.g. Hock 1998; Hock 2005; Hu & al. 1999; Oke 1987; Wagnon & al. 2003) where $h_{wa}$ can be expressed as follows:

$$h_{wa} \sim \rho_a C_a K_s U \tag{3.6}$$

in which $\rho_a$ is the air density, $C_a$ is the specific heat of the air under constant pressure, U is the wind speed and $K_s$, the bulk-exchange coefficient. Generally, $K_s$ is determined by calculating the relative effect of air buoyancy on the mechanical forces of eddies over a horizontal surface. Such an approach is inapplicable in our case because the heat budget is calculated for water flowing over a vertical plane. We decided to opt for a simplified approach where $K_s$ is adjusted empirically.

We also applied this approach to determine the latent heat flux (e.g. Maeno & al. 1994b; Makkonen 1988):

$$Q_{evap} = h_{wa} \frac{0.622 L_e}{C_w P} (Re_{(T_a)} - e_{(T_f)}) \tag{3.7}$$

where $L_e$ is the latent heat of evaporation at $0°C$, $C_w$ is the specific heat of water, P is the air pressure, R is the relative humidity, $e(T_a)$ and $e(T_f)$ are the saturation water-vapor pressures over water at $T_a$ and $T_f$.

Because $\rho_a$, $C_a$, $L_e$, $C_w$ and $T_f$ are constant and $T_a$, U, P, R and $e(T_a)$ are measurable variables, the only empirical value remains $K_s$. With this approach, we assume that $h_{wa}$ varies (increases) linearly with wind speed.

58

### 5.1.2. Net all-wave radiation

The net radiation of the ice cascade surface is the difference between the incoming and outgoing radiation absorbed and emitted by the surface:

$$Q_{rad} = \big(G(1 - \alpha)\big) + \text{IR} \tag{3.8}$$

where G is the global (direct and diffuse) solar radiation, $\alpha$ is the albedo of ice and IR is the long wave radiation emitted by the ice surface. We are aware that $Q_{rad}$ is probably slightly underestimated by our measurements as the spectral range of measurement of the pyranometer used in the study does not include the incoming long wave radiation. Furthermore, an albedo value for this type of ice is unavailable. The lack of literature on the subject suggests that such measurements have not been realized yet. The albedo of natural ice is highly variable: it can have a value of 0.1 for dirty glacier ice, 0.3 for newly formed sea ice, 0.4 to 0.5 for slush-ice or freezing ice and even around 0.9 for ice covered with fresh snow (e.g. Bolsenga 1969; Hock 2005; Hu & al. 1999; Oke 1987). During the ice cascade growth and decay, the albedo of the ice-water system changes as the initial bluish ice turns to white with time (Fig. 3.2). Consequently, we used a value of 0.5 which represents a qualitative estimation and a mean value for different types of natural ice.

Finally, IR can be written:

$$IR = \sigma a\big(T_a - T_f\big) \tag{3.9}$$

where $\sigma$ is the Stefan-Boltzmann constant and $a$ is the radiation linearization constant (8.1 x $10^7$ K$^3$). In this equation, it is assumed that the emissivity of the ice cascade surface and the environment are both unity (Makkonen 1988; Makkonen 2000).

### 5.1.3. Rockwall conductive heat flux

As shown on Figure 3.6, the conductive heat flux from the rockwall was taken into account:

$$Q_{cc} = k_{rw} \frac{T_{rw} - T_f}{X_{rw} - X_{rs}} \tag{3.10}$$

where $k_{rw}$ is the thermal conductivity of the rock. In this case, the rockwall is a highly fractured assembly of bedded shale, limestone and sandstone (Brisebois & Nadeau 2003).

The thermal conductivity of this type of rock varies from 1.2 $W \cdot m^{-1} \cdot K^{-1}$ for a highly hydrated shale to 2.3 $W \cdot m^{-1} \cdot K^{-1}$ for a dry mudstone – sandstone (Bloomer 1981). It essentially depends on water saturation, rock type and bedding planes. In our case, we assume that the rock mass is highly hydrated and we choose a value of 1.5 $W \cdot m^{-1} \cdot K^{-1}$. $T_{rw}$ corresponds to the mean annual temperature in northern Gaspésie (3.65°C) (Environnement Canada 1971-2000)(Environnement Canada 1971-2000)(Environnement Canada 1971-2000), $T_f$ is the temperature of the rock-ice interface (0°C), $X_{rs}$ is the rock-ice depth interface (0 m) and $X_{rw}$ is the depth at which the rock temperature does not vary from the mean annual temperature (2.1 m). To determine this depth, we measured the rockwall temperature from the surface to 80 cm underneath the surface. After a one-year measurement period, we were able to extrapolate the depth where no temperature change occurs during the whole year. At the end, a constant value of 2.6 $W \cdot m^{-2}$ was calculated for the rockwall conductive heat flux.

### 5.1.4. Energy flux from flowing water

The fifth term in the energy balance equation represents the heat flux carried by the flowing water. This heat flux is very important because it also represents the volume of water available for the production of ice. It can be written:

$$Q_w = \frac{C_w D_{in}(T_{wt} - T_{wb})}{S}$$ (3.11)

where $C_w$ is the specific heat of water, $D_{in}$ is the incoming discharge, $T_{wt}$ and $T_{wb}$ are, respectively, the water temperature at the top and bottom of the waterfall and S is the mean surface area covered by the ice cascade (or the waterfall) on the rockwall.

### 5.1.5. Energy flux released by the freezing water

When the temperature drops below 0°C and a sufficient amount of heat is lost through the environment, ice forms in the flowing water. The latent heat released during the freezing process is:

$$Q_{ice} = \frac{L_f \frac{dM}{dt}}{S}$$ (3.12)

where $L_f$ is the latent heat of freezing (or melting), dM/dt is the ice production rate per unit mass. The energy balance (4) can then be used to estimate the ice production:

$$\frac{dM}{dt} = \frac{-S(Q_{cv}+Q_{evap}+Q_{rad}+Q_{cc})}{L_f} \qquad (3.13)$$

where dM/dt is in $Kg \cdot s^{-1}$. Finally, the volume rate production dV/dt is given by:

$$\frac{dV}{dt} = \frac{\frac{dM}{dt}}{\rho_i} \qquad (3.14)$$

where $\rho_i$ is the density of the ice. The ice density was determined from different ice structures (ice stalactites, ice accretions) sampled directly on the ice cascade and measured by tomodensitometry (e.g. Boespflug & al. 1994; Calmels & Allard 2004; Hounsfield 1973; Knoll 1989). A mean value of 880 $kg \cdot m^{-3}$ was used for calculations. At last, $K_s$ remains the most critical adjustable variable in the model (eq. 3.6).

### 5.1.5. Model 1: Results

Figure 3.8 shows different ice production curves with different values of $K_s$, ranging from 0.0005 to 0.2. By giving $K_s$ a high value, the overall ice production in the cascade follows quite well the FDH curve general shape presented in Figure 3.5E. In this situation, the sensible heat flux and the latent heat flux are the dominant terms in the heat balance. This agrees with what can be expected from the hydrometeorological data analysis where the air temperature evolution represented by the FDH appears to be the main variable controlling the ice cascade growth. Using a small $K_s$ means minimizing the effect of $Q_{cv}$ and $Q_{evap}$ in the ice production process, hence leading to a heat budget mainly controlled by the other terms, especially the sensible heat carried by the flowing water $Q_w$. The increase in ice production after day 164 in this case (Fig. 3.8) is a spurious effect of $Q_w$. During this period, the air temperature, which remained above the melting point, transfers heat to the water, resulting in a water temperature higher at the bottom than at the top of the waterfall. This leads to a negative value of $Q_w$. In fact, it represents the energy transferred to the water by $Q_{cv}$ and $Q_{evap}$ that leaves the system along with the flowing water. This effect is hidden by the high value of $Q_{cv}$ and $Q_{evap}$ when using a high value of $K_s$.

When running the model, we realised that the linear effect of the wind on $h_{wa}$ (eq. 3.6) was incoherent with our observations. During cold but calm days, we observed that the ice cascade was actually forming very rapidly. In the model, a very low value of wind speed tends to lower the $h_{wa}$ value near 0. The result is an underestimated value of $Q_{cv}$ and $Q_{evap}$ during these calm periods. To adjust this effect into the model, we were forced to increase the value of $K_s$. To best fit the changes in measured ice volume, a value of $K_s$ ranging between 0.01 and 0.2 must be used.

The amount of ice predicted with this model is higher than the actual ice volume (see Figures 3.5 and 3.8). If the model is well balanced, then the ice production is well estimated. This implies that in reality, the system must evacuate a large fraction of the ice produced. Only a small fraction of the ice remains fixed to the rockwall. This finding is not surprising and is in close agreement with the production of frazil ice reported in fluvial systems (e.g. Martin 1981; Osterkamp & Gosink 1983; Turcotte & Morse 2011). Frazil ice is produced in rapids with highly turbulent flow and carried away by the current at the foot of the riffles. Frazil ice concentration can reach $10^7$ ice discs per $m^3$ of water and the production rate can reach 100 x $10^6$ $m^3{\cdot}day^{-1}$ in large open water river (Martin 1981; Michel 1971; Osterkamp & Gosink 1983). Sometimes the ice pellets are fixed to the gravel-bed as anchor ice, but they usually form floating frazil flocs, frazil pans or slush which accumulate against booms or static ice covers in low velocities zones. We observed, during low temperature periods, that the water temperature at the bottom of the waterfall was in a supercooled state and that a huge amount of frazil ice was leaving the system. Moreover, by comparing the average amount of ice formed between LiDAR measurements with the discharge, we calculate that no more than 0.5% of the discharge is retained in the system to form the ice cascade (before 21 January 2011). After the complete closure of the ice cover over the rock wall (after 21 January 2011), we found that 0 to 5% of the discharge is retained in the system to form the ice cascade. When we consider the calculated value during the initial growth stage (before January 21st), the energy evacuating the system might be sufficiently high to cause the entire flow to freeze. This behavior may seem unrealistic, but it is actually in agreement with the observations: a high amount of the supercooled slush-like moving water flows away. After the ice completely covers the rockwall, the discharge becomes very low and the flowing water is isolated from the

environment by the thickening ice wall on the cascade face. To adapt the model to those issues, an empirical variable representing the percentage of ice formed and remaining in the system has to be used (%IF).
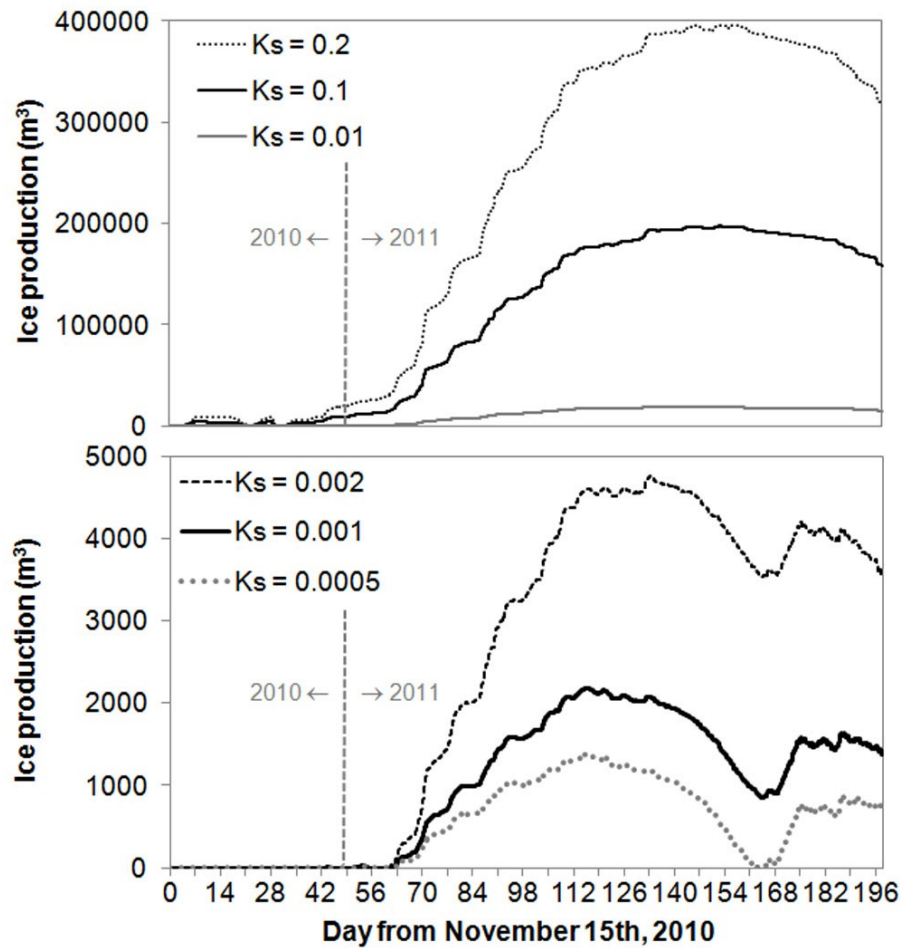


**Figure 3.8.** Calculated ice production (model 1) with different value of $K_s$: from November 15th 2010 (day 0) to May 31st 2011 (day 197).

## 5.2. MODEL 2

As previously mentioned, during the initial stage of the growing process, the water is constantly in contact with the air and the ice only forms at the edges of the water flow. From January 21st (day 67), an ice cover forms over the whole rockwall surface and the growth dynamics change (Fig. 3.2 and 3.6). The ice cover isolates the flowing water from the outer environment. A convective sensible heat transfer at the water-air interface does not apply anymore to this new situation. To improve the efficiency of the model, we now propose a two-stage model. Figure 3.9 presents a schematic illustration of this second model.

### 5.2.1. Model 2: Stage 1

During the first stage (day 0 to 66), the flowing water is directly in contact with the atmosphere (Fig. 3.9). The same heat budget used in model 1 is applied (eq. 3.4). But this time, we modified the calculation of the heat transfer coefficient ($h_{wa}$):

$$h_{wa} \sim \rho_a C_a K_s U_{eff} \tag{3.15}$$

where $U_{eff}$ represents the effective contribution of the wind:

$$U_{eff} = U + U_d \tag{3.16}$$

where $U_d$ is the droplet (water flow) mean falling speed. The freefalling speed of a raindrop is ranging between 1 and 9 m s$^{-1}$ depending on the size of the droplet (e.g. Atlas & al. 1973; Gunn & Kinzer 1949). After one meter of drop, a large droplet (0.6 cm) can reach the maximum speed of free fall. Since the droplet size and the proportion of the water flow that fragments and fall freely is unknown, we assumed a mean value of 5 m s$^{-1}$ for a 45 m waterfall. Such a constant will reduce the tendency to minimize the role of air convection around the water flow during calm days. Indeed, the wind generated during the free fall of the water flow favors convective heat exchanges with the air. Adding a mean value of the droplet (water flow) falling speed results in a minimum amount of wind speed effect in the calculation of $h_{wa}$. To adapt the model to this improvement, a value of 0.048 was given to $K_s$ to best fit the measured ice accumulation trend and the highest $R^2$ value between the measured ice volumes and those calculated (Fig. 3.10A).

The other variables were not modified. However, we added an empirical constant representing the percentage of ice formed and remaining in the system (%IF = 0.002 or 0.2%) to adjust the model to the ice volume measurement (the value was determined empirically by dividing the mean amount of accumulated ice between each LiDAR measurement):

$$\frac{dV}{dt} = \frac{\frac{dM}{dt}}{\rho_i} * \%IF \tag{3.17}$$

### 5.2.2. Model 2: Stage 2

During the second stage (from day 67 up until the end), the ice covers the whole rockwall and different physical processes are take place. The ice isolates the water flow from the atmosphere. In the model, all the heat is evacuated from the isolated water flow even if occasional exfiltration over the ice cascade is observed and involved in the growing process. The heat budget can now be written as:

$$0 = (Q_{cv} \ or \ Q_{ic}) + Q_{sub} + Q_{cc} + Q_{rad} + Q_{water} + Q_{ice} \tag{3.18}$$

As with the model proposed by Montagnat & al. (2010), we suggest a conductive heat transfer through the ice to the water, keeping in mind that the outside surface temperature of the ice cover ($T_{is}$) tends to $T_a$ and the temperature at the ice-water interface is $T_f$. In this case, we assume a linear gradient of the temperature within the ice cover and the conductive heat transfer flux through the ice ($Q_{ic}$) can be described by:

$$Q_{ic} = \frac{k_{ice}}{I_t}(T_{is} - T_f) \tag{3.19}$$

where $I_t$ is the ice cover thickness and $K_{ice}$ is the thermal conductivity of ice (2.22 W·m$^{-1}$·K$^{-1}$ at 0$^o$C). We calculate $I_t$ at each time step by dividing the calculated ice volume by the mean surface area covered by the ice cascade (S).

$Q_{ic}$ takes effect when ice formation occurs ($T_a < 0^oC$). When $T_a$ is above the melting point of ice, air convection at the ice-air interface favors heat transfer to the ice cascade. The ice surface temperature ($T_{is}$) is at $T_f$ and $Q_{cv}$ can be written:

$$Q_{cv} = h_{ia}(T_a - T_f) \tag{3.20}$$

where $h_{ia}$ is the heat transfer coefficient at the ice-air interface, again calculated as a bulk formulation:

$$h_{ia} \sim \rho_a C_a K_s U \qquad (3.21)$$

where $K_s$ is the bulk exchange coefficient between the air and the ice surface. An empirical value of 0.09 returns the best fit with the measured ice volume values.

Because there is now no more direct interaction between the water and the outside environment, $Q_{evap}$ is replaced by a sublimation heat flux ($Q_{sub}$):

$$Q_{sub} = h_{ia} \frac{0.622 L_s}{C_i P} \left( Re_{(T_a)} - e_{(T_{is})} \right) \qquad (3.22)$$

where $L_s$ is the latent heat of sublimation at 0°C, $C_i$ is the specific heat of ice and $e(T_{is})$ is the saturation water-vapor pressure over the ice at $T_{is}$. Because we assume that $T_{is} = T_a$ when the temperature is below 0°C, $Q_{sub}$ remains null during the freezing period. When the temperature is above 0°C, $T_{is} = T_f$ and sublimation occurs.

Finally, we consider that the other fluxes remain identical as in the first stage. An empirical variable representing the amount of ice retained in the system and participating to the ice cascade growth process is required (%IF). As mentioned previously, no more than 5% of the water mass flux is retained as ice in the system during this period. Hence an empirical value of 0.015 (1.5%) was used for %IF in the ice volume calculation (same forms as in eq. 3.17).

**First stage**
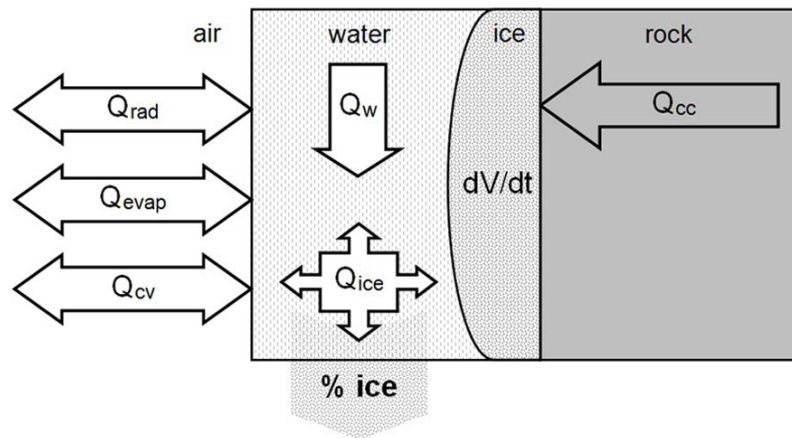


**Second stage**
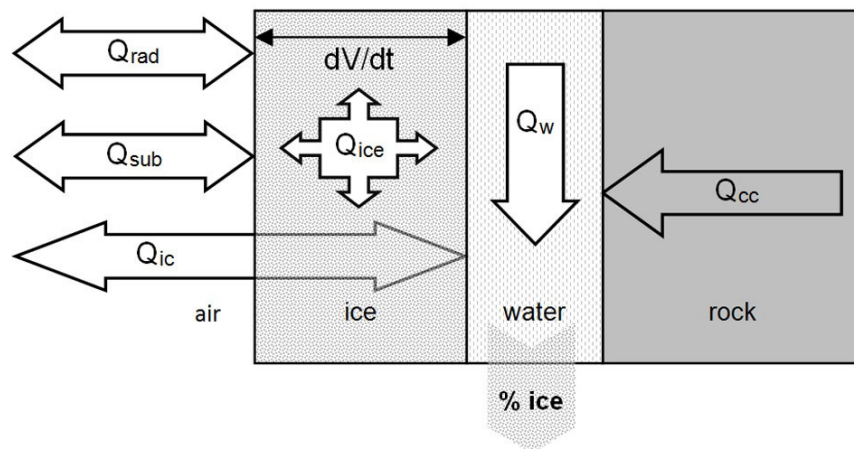


**Figure 3.9.** Schematic illustration of a two-stage ice cascade growth and decay model (model 2).

*5.2.3. Model 2: Results*

Figure 3.10 presents the calculated ice cascade volume evolution given by model 2. In this figure, model 1 is also presented, but with the use of the same %IF as in the first stage of model 2 (0.2%) and with a $K_s$ value of 0.2. Figure 3.11 shows the normalized evolution of the different fluxes for the entire duration of the model run and figure 3.12 presents representative examples of an energy balance during freezing and melting periods for the two different stages of the model.

The results show many differences between the two models. First of all, the use of a constant representing the water freefalling speed ($U_d$) during the early stage of formation has forced the readjustment of $K_s$ from 0.2 to 0.048. The resulting value is now closer to values used to calculate energy exchanges over melting glacier (e.g. Hay & Fitzharris 1988). Except for the ice volume measurement of December 10th, the calculated values are very close to those measured (Fig. 3.10A and 3.10B). After the complete insulation of the water flow by the ice cover on January 21st, both models (model 1 and model 2 – stage 1) overestimate the ice cascade volume. At this stage of formation, the transition between a regime ruled by air convection around the water flow to a regime ruled by conductive heat transfer through the ice cover (model 2 – stage 2) has led to a better representation of the bulk evolution of the ice volume. As previously mentioned by Montagnat & al. (2010), ice cascades show an asymptotic growth behavior when they reach a given thickness. In our case, the ice reached a mean thickness value of 8 cm before such behavior was observed (around day 80). The model also depicts this tendency. Following this slow growing stage, a small increase of the discharge after a 15 mm rain event (between day 116 and 120) accelerated the melting of the ice cover (Fig. 3.5D and 3.5E). The model shows a little decrease during this event, but it is not able to predict the rapid decrease in ice volume associated with the partial collapse of the ice structure (Fig. 3.10A).

During stage 1, $Q_{cv}$ is the dominant flux controlling the ice cascade growth and melt process (Fig. 3.11 and 3.12). Evaporation ($Q_{evap}$) is also carrying heat out of the water, but its contribution remains small. The diminishing energy carried by the flowing water ($Q_w$) is of great importance at the beginning of the growth process. If the discharge remains high, the ice cascade would only form on the edges of the flow and the other heat fluxes are not

efficient enough to freeze the water in the main flow path. The radiation heat flux, mostly the solar diffuse radiation, carries a little heat to the system but it seems to contribute only when the air temperature is close to $0^o$C. The little heat coming from the rockwall appears negligible in comparison with the other fluxes.

The second stage of model 2 follows the asymptotic tendency of the measured ice volume. The use of a conductive heat transfer flux into the ice ($Q_{ic}$) yields a better approximation of the heat exchange between the water and the outside environment. $Q_{ic}$ and $Q_{cv}$ (at the air–ice interface) remain energy fluxes of primary importance (Fig. 3.11 and 3.12). Right after the transition phase, the discharge is still at its lowest level and the diffuse solar radiation received at the ice surface is very low. The ice cascade can pursue its growth rapidly. Even if the heat conduction into the ice is low, the ice is thin and allows a relatively good heat exchange between the thin liquid film and the outside cold air. But as the ice cascade gets thicker, the heat exchange ($Q_{ic}$) also decreases. During this period, the ice cascade is in a delicate equilibrium state. The growth of the ice cascade is now also controlled by the radiative energy balance ($Q_{rad}$), but more specifically by the increasing contribution of direct solar radiation from the end of February (Fig. 3.11 and 3.12). Even if the direct solar radiation is reaching the surface with a high incident angle, the radiative energy budget tends towards positive values favoring heat accumulation at the surface of the ice. This leads to a decrease in the growth rate during cold days but it favors melting when air temperature tends toward zero Celsius (Fig. 3.12). The rising discharge in mid-March increases the amount of sensible heat carried by the flowing film of water ($Q_w$). Our observations show that the ice cascade melts rapidly at the ice–rock interface. As mentioned earlier, we observed massive voids opening between the ice and the rock wall on March 30th and April 10th 2011 (Fig. 3.2). Actually, the increase in discharge began on March 17th 2011 after a 12.5mm rain event (Fig. 3.5D). But, the ice cascade melts and collapses rapidly only after the significant increase of the discharge on April 11th 2011 (Fig. 3.10a and 3.12). The ice volume measured on April 15th 2010 was composed of small residual ice structures standing on the edges of the main water flow. The model trend cannot reproduce the thermo-erosive action of the flowing water and the collapsing process occurring during this fast melting period. At this point, model 2, stage 2 becomes incompatible with the ice formation and melting process. During this last period, some ice

may form around the main flow during a cold spring night but it rapidly melts the following days. The growth and melt processes then return to a regime that is more compatible with the first stage of model 2.
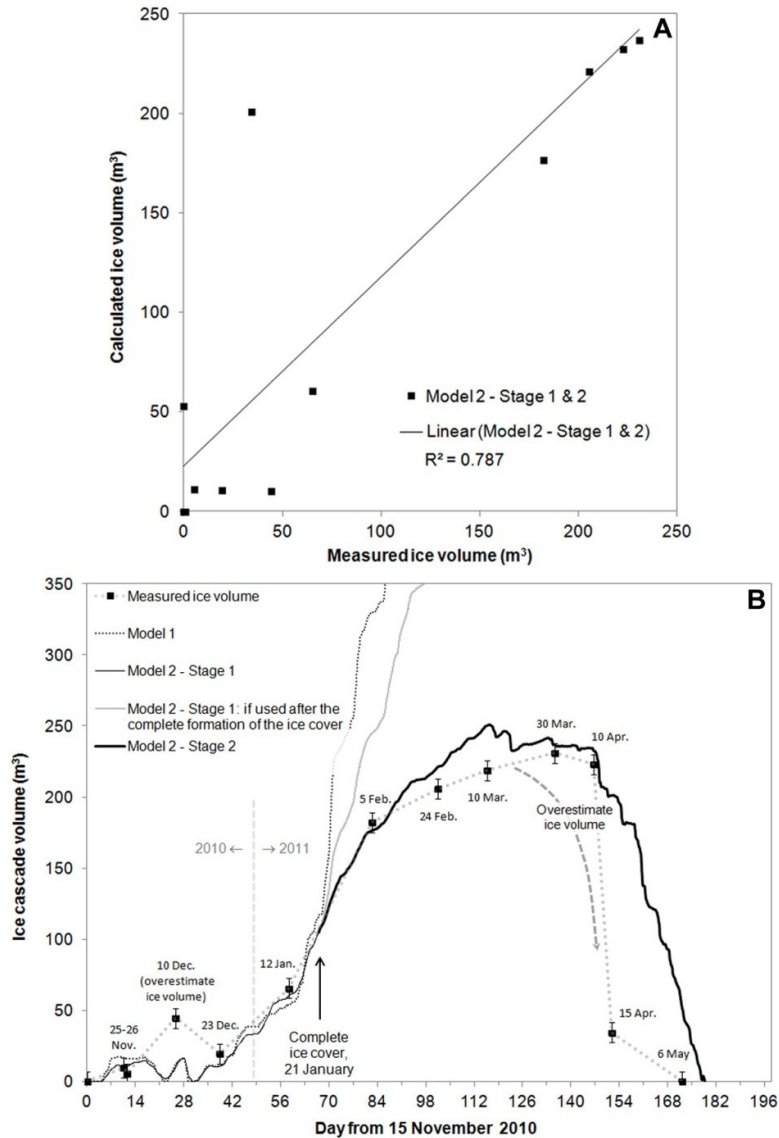


**Figure 3.10.** A) Calculated versus measured ice cascade volume. B) Calculated and measured ice cascade volume evolution. The thin black line is the first stage of the second model from day 0 to day 66 (15 November 2010 to 21 January 2011) (%IF = 0.2%; Ks = 0.048). The gray line is the continuation of the second model's first stage after day 66 (%IF = 0.2%). The thick black line is the second stage of the second model from day 66 to the end of the modelling (21 January 2011 to 31 May 2011) (%IF = 1.5%; Ks = 0.09). The dashed gray arrow represents a more probable ice volume evolution.
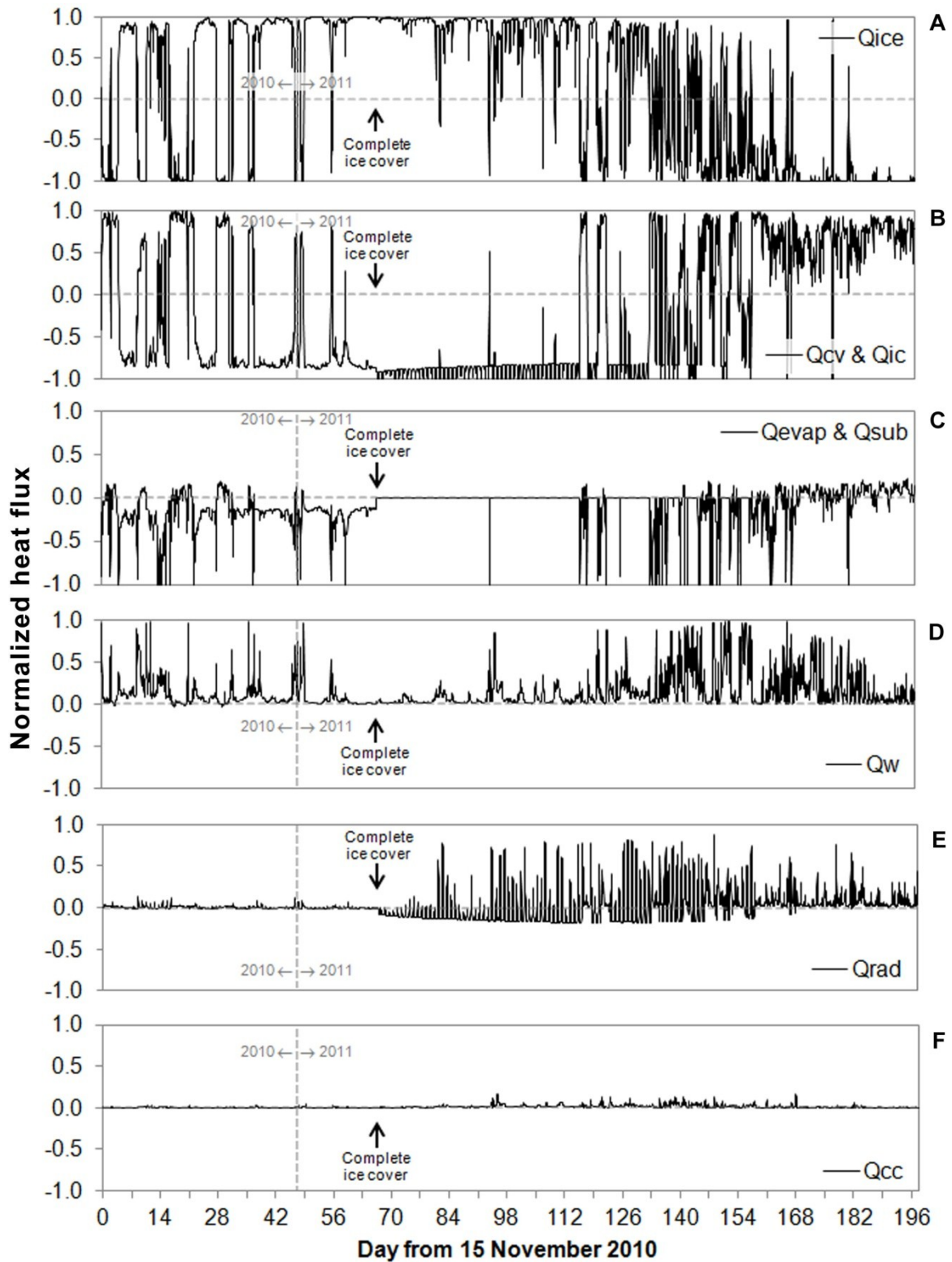
**Figure 3.11.** Normalized heat fluxes comparison during the first and second stages. Each normalized heat fluxes is the ratio between fluxes and the sum of fluxes of the same sign (positive or negative).
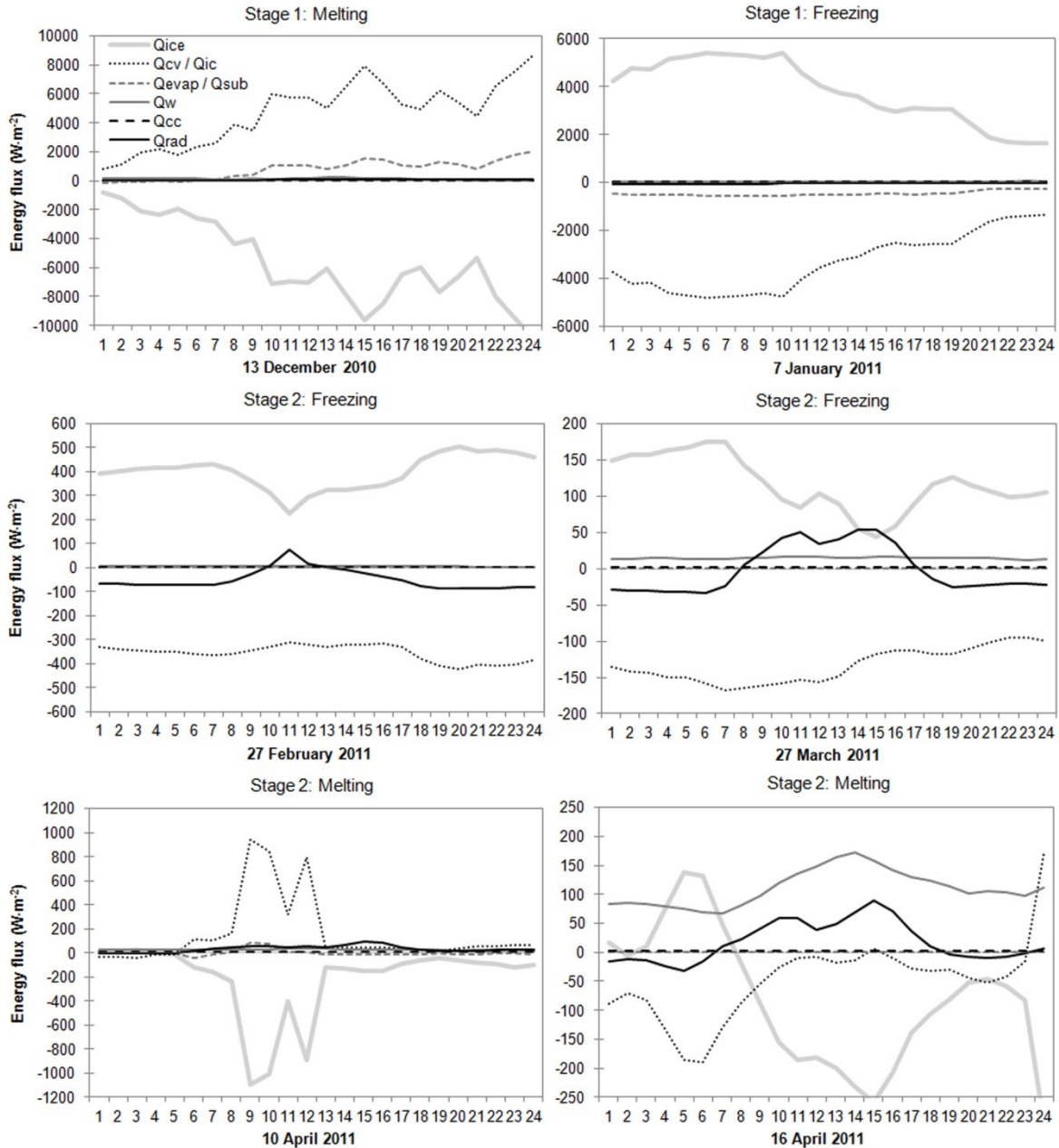
**Figure 3.12.** Examples of 24 hour energy balance during freezing and melting periods for the two-stage modelling. 13 December 2010 was a partly cloudy day with an average air temperature of 9.9°C, a minimum of 1.9°C and a maximum of 16.7°C. 7 January 2011 was a partly sunny day with an average air temperature of −10.3°C, a minimum of −15.2°C and a maximum of −4.3°C. 27 February 2011 was a sunny day with an average air temperature of −16.0°C, a minimum of −19.1°C and a maximum of −13.9°C. 27 March 2011 was a sunny day with an average air temperature of −6.3°C, a minimum of −8.0°C and a maximum of −4.5°C. 10 April 2011 was a partly sunny day with an average air temperature of 3.0°C, a minimum of −1.8°C and a maximum of 6.2°C. 16 April 2011 was a sunny day with an average air temperature of −2.2°C, a minimum of −7.5°C and a maximum of 1.4°C.

### 5.2.4. Model 2: Sensitivity analysis

Three constants ($K_s$, $U_d$ and $\alpha$) were tested to verify the sensitivity of the model to changes in parameters values. The results are presented in figure 3.13. Increasing or lowering the value of the bulk exchange coefficient ($K_s$) by 30% affects the magnitude of the ice volume evolution (Fig. 3.13A). This leads to a difference in the percentage of ice fixed to the rock wall (%IF) of ±0.2%. The same kind of effect is observed when changing the value of the mean freefalling speed of the droplets (or water flow) ($U_d$) down the rockwall (Fig. 3.13B). Lowering $U_d$ from 5 to 3 m s$^{-1}$ leads to an increase of 0.13% of retained ice in the system (%IF) and increasing $U_d$ to 7 m s$^{-1}$ leads to a decrease of %IF of 0.2%. Because, these two factors ($K_s$ and $U_d$) affect the calculation of the heat exchange coefficient ($h_{wa}$) and therefore the convective heat flux ($Q_{cv}$), their revisions mostly change the ice growth and decay curve during the first stage of formation when $Q_{cv}$ is the main heat transfer flux.

Since the radiative heat budget ($Q_{rad}$) has a significant impact during the second stage of formation it is relevant to evaluate the sensitivity to the ice surface albedo ($\alpha$). To verify the effect of $\alpha$ on the ice cascade volume evolution, higher and lower values were tested (0.3 and 0.7) (Fig. 3.13C). These modifications do not cause any changes in the first stage of formation. However, during the second stage, a lower $\alpha$ leads to an underestimation of the ice volume fixed to the rockwall (%IF) of nearly 3%. A higher value for $\alpha$ leads to an overestimation of %IF by 3%. After the complete formation of the ice cover over the rockwall, an $\alpha$ value of 0.3 is clearly insufficient considering the bluish, nearly white, color of the ice cascade (Fig. 3.2). An albedo between 0.5 and 0.7 is certainly much closer to the reality. However, even if the modification of these three parameters changes the magnitude (increase or decrease) of the ice volume evolution curve, it does not affect its shape and general trend.
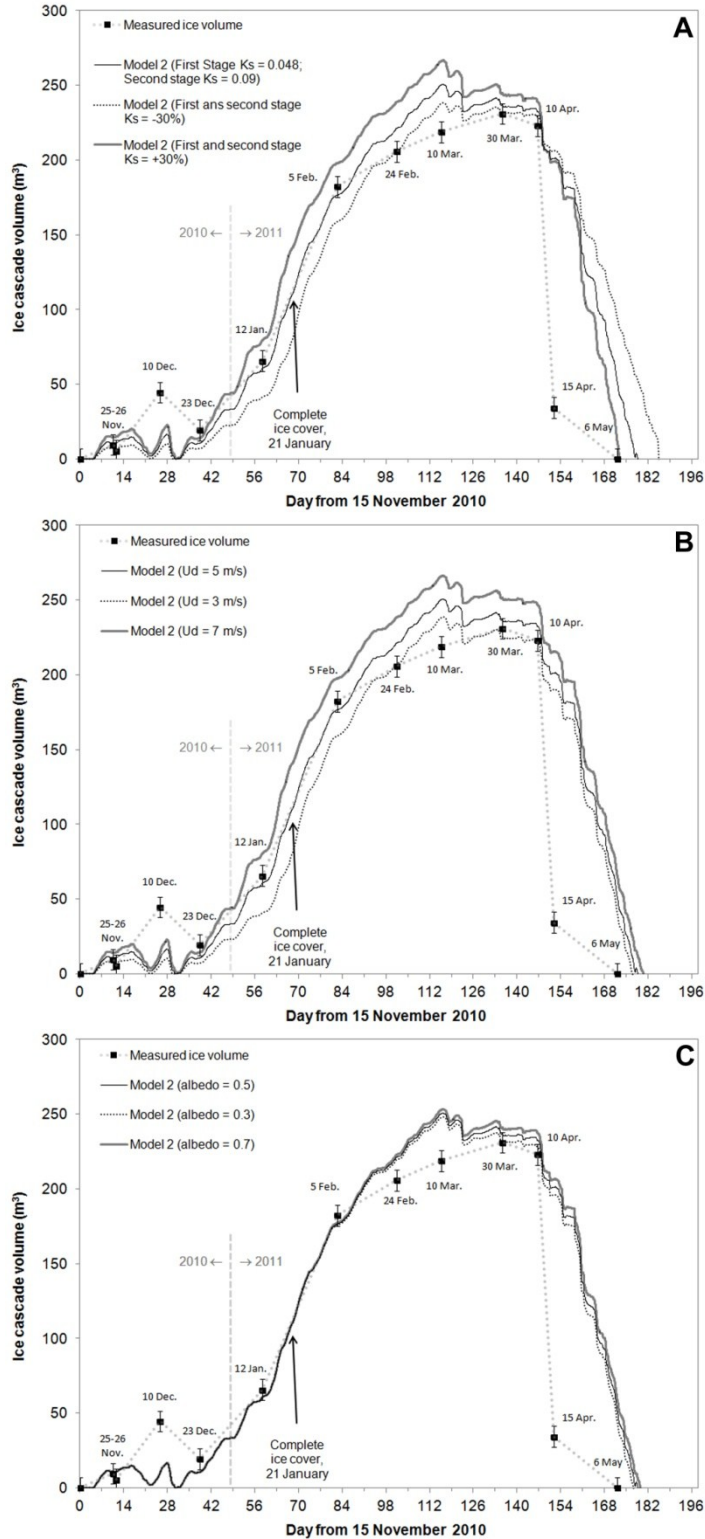
**Figure 3.13.** Calculated and measured ice cascade volume evolution for different value of $K_s$ the bulk-exchange coefficient (A), $U_d$ the water flow or droplet freefalling speed (B) and $\alpha$ the albedo (C).

## 6. DISCUSSION AND CONCLUSIONS

Modelling the ice cascade volume evolution has revealed the importance of the different hydrometeorological variables and energy fluxes. First, the primacy of the convective heat transfer ($Q_{cv}$) in the initial growing stage was confirmed. The temperature gradient between the flowing water near $0^oC$ and the air temperature supports the freezing degree-hours (FDH) calculation. Even if the FDH curve shows a significant lag with the measured ice volume, it shows the same general trend. It might eventually be used to model other kind of rockwall icings or to predict their collapse (Gauthier 2008; Gauthier & al. 2012).

The linear dependency between the convective heat transfer coefficient ($h_{wa}$) and the wind speed (U) is of utmost importance. Unlike many thermodynamic models developed to simulate the growth of ice stalactites (Maeno & al. 1994b; Makkonen 1988), icing and river ice formation (Ashton 1989; Hu & al. 1999; Schohl & Ettema 1986; Schohl & Ettema 1990) or glacier melt models (e.g. Hock 1998; Hock 2005; Munro 1989; Wagnon & al. 2003), the present model is adjusted by introducing a variable representing the mean freefalling speed of the water flow ($U_d$). This adjustment provides a better representation of the physical processes involved in the formation of ice accretions around the main water flow after the freezing of water spray, a general process similar to freezing rain accumulations (Gauthier 2008; Gauthier & al. 2012; Jones 1996; Makkonen 2000). Furthermore, since a very high percentage of the ice produced during the freefall of the water flow is evacuated at the base of the frozen waterfall, an ad-hoc constant representing the percentage of ice fixed to the rockwall and participating to the ice cascade volume evolution (%IF) had to be added to the model. The values of %IF were fixed empirically from the ratio between the discharge and the mean amount of ice produced between each LiDAR measurements. At last, this constant was proven to be stable and the model is robust to parameters change.

During the initial growth stage, the model also reveals the relative importance of the latent heat flux ($Q_{evap}$). This flux, mainly controlled by the relative humidity, is significant when the air temperature is slightly below zero and the relative humidity is low. Under these conditions, $Q_{evap}$ greatly favors ice formation. The low mean annual air temperature in northern Gaspésie leads to a low conductive heat flux ($Q_{cc}$) emanating from the rockwall.

This flux remains low and trivial in our case, but it might play a more relevant role in warmer climates such as in the Alps or Western America where ice is sporadically forming during winter. The diminishing water flow at the beginning of winter favours the growth of the ice cascade. Conversely, in spring, the increasing discharge ($Q_w$) becomes a major heat source during the ice cascade melting process. These observations are consistent with the results obtained by Maeno & al. (1994b). They showed that ice stalactites tend to grow faster under low discharge regime. Furthermore, the relevance of the sensible heat flux carried by the flowing water ($Q_w$) may not be significant under low discharge regime; as in the case of ice walls growth which forms after the gradual freezing of ground-water seepage on a cliff.

Finally, one of the major findings is the critical role of the radiation budget ($Q_{rad}$) after the isolation of the water flow by a complete ice cover. While the radiative heat transfer ($Q_{rad}$) intake is insignificant during the initial growth stage, it becomes a major source of heat during the second stage. This transition between a system controlled by air convection ($Q_{cv}$) to one controlled by a conductive heat transfer flux through the ice ($Q_{ic}$) changes the physical growth process. The growth rate is reduced during the day when direct solar radiation is received at the ice surface. As the solar radiation increases in spring, the growing and melting process becomes highly controlled by this intake.

To our knowledge, this paper is the first to expose an energy balance model for this kind of ice formation. Moreover, the two-stage model proved to be relevant to simulate the ice cascade volume general tendency. However, further studies should be conducted to evaluate the accuracy of the empirical variables and constant values used in existing models: the ice cascade albedo, the heat exchange coefficient expressed in terms of the bulk exchange coefficient, and the percentage of ice produced and evacuated from the system, to mention just a few. Furthermore, the models would need to be validated in different environmental conditions (e.g. slope aspect, low discharge regime, other climate regimes, ...).

# CHAPITRE 4: ICE WALLS GROWTH AND DECAY: METEOROLOGICAL ANALYSIS AND MODELLING

Francis Gauthier, Michel Allard and Bernard Hétu

**Résumé :** La croissance et la fonte de trois carapaces de glace ont été analysées et modélisées au cours de l'hiver 2010-2011. Ces formations de glace se forment à la suite du gel des résurgences d'eau sur une falaise : deux carapaces sont exposées au nord et l'autre au sud. Trois modèles ont été développés à partir des données météorologiques recueillies à proximité de chacune d'entre elles. Ils ont été ajustés et validés à partir des volumes de glace estimés à l'aide d'une série d'images acquises au LiDAR terrestre. Un modèle thermodynamique est d'abord proposé et ensuite comparé avec deux modèles simplifiés. Le premier est issu du calcul des degrés-heures de gel (DHG) et le second est une combinaison de ce modèle avec le bilan radiatif (Qrad). La modélisation thermodynamique a révélé que la perte thermique par convection entre l'eau de ruissellement et l'atmosphère est le principal flux de chaleur responsable de la croissance et de la fonte des carapaces de glace exposées au nord. L'évolution de la carapace de glace exposée au sud est fortement dépendante de la variation quotidienne du Qrad. Enfin, le modèle des DHG parvient à simuler adéquatement l'évolution des carapaces de glace orientées au nord. L'ajout de Qrad à ce modèle améliore considérablement ses performances. Il s'est avéré être le meilleur pour simuler la croissance et la fonte des trois carapaces de glace.

**Abstract :** The growth and decay of three ice walls was surveyed and analyzed during the winter of 2010-2011. The ice walls form on a cliff due to the freezing of seeping ground water: two on north-facing rockwalls and one over a south-facing blasted cliff. Ice walls growth and decay models were developed from meteorological data collected in their immediate surroundings. Terrestrial LiDAR images were used to estimate the volumes of ice formed or lost and validate models results. A complete energy balance model is first proposed and compared with two simplified models. The first one is a freezing degree-hours model (FDH), and the second one is a model that combines the FDH and the radiation heat budget (Qrad). Both models reveal that heat loss from air convection from the seeping water to the atmosphere is the dominant heat transfer flux responsible for the north-facing ice walls growth and decay. Solar radiation also plays a major role for melting of these ice walls. In return, the overall evolution of the south-facing ice wall is more dependent of the daily variation of Qrad. When the air temperature is cold, the ice forms mostly during the night while solar radiation favours its melting during the day. When the temperature rises above 0°C, solar radiation remains the main heat flux responsible for the melting of the south facing ice wall. In summary, the FDH model adequately describes the dynamics of north facing ice walls but remains inappropriate to simulate the south-facing ice wall's growth and decay. Adding Qrad to the FDH model improves it performance and proves to be the best model to simulate the dynamics of ice walls evolution.

# 1. INTRODUCTION

Recent works presented statistical (Gauthier 2008; Gauthier & al. 2012), physical (Montagnat & al. 2010) and mechanical (Weiss & al. 2011) analysis of the dynamics of various ephemeral ice formation on cliff faces. These ice structures grow from the freezing of liquid water that seeps or streams over rocky cliffs. The growth of these structures begins with the formation of ice stalactites and ice concretions. Continuous negative air temperatures (expressed as a "freezing potential") lead to a rapid growth rate at the beginning of the cold season (Montagnat & al. 2010). As the ice structures aggregate together, the water flow between the ice covers and the rockwall becomes isolated from the atmosphere. The volume of ice produced then decreases asymptotically and reaches a maximum. Mechanical stress induced by a rapid cooling of the air over several hours to temperatures below $-10^{\circ}$C can generate fractures in the ice and trigger the collapse of unstable ice structures such as freestanding or hanging ice formations (Gauthier & al. 2012; Weiss & al. 2011). Conversely, the accumulation of positive air temperatures (known as the "melting or positive degree-days") controls the ice melting process (Gauthier 2008; Gauthier & al. 2012). When the ice that is anchored on the rockwalls looses sufficient strength to maintain its structure, ice walls ultimately collapse.

Each spring, in northern Gaspésie, (Québec, Canada) a series of ice-block falls is reported by the "Ministère des Transports du Québec" (MTQ) (Gauthier 2008; Gauthier & al. 2012; Girard & Hétu 1994; Hétu & al. 1994). In addition, as the interest for mountaineering and ice climbing increases in North America, the number of traumatisms reported since 1951 increased as well (American and Canadian Alpine Club 1999). Indeed, 20% of the 200 to 400 accidents reported each year occur during the practice of ice climbing. Despite that, the physical and mechanical behaviour of vertical frozen waterfalls was only recently studied in the Alps (Weiss & al. 2011) and in northern Gaspésie (Gauthier 2008; Gauthier & al. 2012) and existing knowledge on the geographical and hydrometeorological variability of the processes controlling the formation and melting process remains limited. One reason is the complexity of the mass and heat transfer involved in their growth and decay processes.

Rockwall icings can be classified according to two hydrological criteria: frozen waterfalls (or ice cascade) when they originate from the freezing of surface runoff over a cliff face,

and ice walls when they come from the freezing of underground water seeping on a cliff (Bianchi 2004; Gauthier 2008; Gauthier & al. 2012). In the first case, the discharge, generally higher, depends on the size of the catchment and is highly variable over time (Dingman 2008; Domenico & Schwartz 1990; Gauthier 2008; Gauthier & al. 2012). The formation of ice walls comes from ground-water (underground and/or subsurface) seepage with lower discharge. Gauthier (2008) and Gauthier & al. (2012) observed that frozen waterfalls generally melt and dislocate earlier in spring than the ice walls. They also show that south facing rockwall icings (ice walls and frozen waterfalls) also tend to collapse earlier than north-facing ice formations. Finally, these ice formations can also be classified according to a geomorphic or static point of view. They can form over a subvertical rockwall with a centre of gravity resting onto the supporting wall or rather over a vertical or overhanging rockwall with a centre of gravity supported at their base (Bianchi, 2004).

To our knowledge, no previous work has specifically focused on the growth and decay of ice walls. In this paper, we present hydrometeorological data collected at three ice wall sites with different geomorphic features and different slope aspects. We also propose a growth and decay thermodynamical model and two simplified models elaborated from analysis of observations and field data. We are not considering the mechanical destabilisation that frequently occurs during large and rapid temperature changes (Weiss & al. 2011). We rather propose an energy balance model based on, and validated from, an important amount of hydrometeorological data collected at the ice wall formation sites. The thermodynamical modelling will clarify the role of the different heat transfer components involved in ice wall growth and decay. We also compared the model with two simplified ones: a temperature index or freezing (melting) degree-hours model based on a relationship between the freezing point of water and the temperature of the air; and a temperature index model combined with the radiative heat budget. The validation of the models is achieved by comparing the simulated and measured ice volumes extracted from a series of terrestrial LiDAR images acquired throughout the 2010-2011 winter season. The objective is to improve our understanding of ice formations growth and decay mechanisms under various conditions in order to facilitate the development of an ice wall collapse forecasting method.

## 2. STUDY SITES

The study was done during the 2010-2011 winter on three distinct ice walls (Fig. 4.1). Two of them, G-69 (Loup-Garou) and G-Amphi (Sans nom), are located along the north shore of the Gaspé Peninsula. The northern Gaspésie escarpments are mostly composed of highly fractured and bedded shale and sandstone covered by a thin layer (less than 1 m) of regolith (Brisebois & Nadeau 2003; Veillette & Cloutier 1993). The other studied ice wall, G-195, is located along road 195, 23 km south of Matane. Along the Matane river valley, cliffs are essentially composed of bedded mudstone and siltstone covered by fluvioglacial deposits composed of stratified sand and gravel (Brisebois & Nadeau 2003; Veillette & Cloutier 1993).

The region's climate is characterized by a temperate and cold maritime climate. The winters are cold with an average minimum temperature in January of -13.7 °C (Gagnon 1970; Environment Canada from 1971 to 2000). The maritime influence of the Gulf of St. Lawrence provides an average rainfall of about 1000 mm evenly spreaded throughout the year, one third of which falls in snow from mid-November to late April. The liquid precipitation in the fall is also relatively high with about 200 mm for October and November. Along the coast, rockwalls are well exposed to the wind with only 14% of calm days per year and with wind speeds frequently exceeding 50 km/h (Hétu and Vandelac, 1989; Gagnon, 1970).

The G-69 ice wall forms over a north-facing ($10^o$), 70 m high, steep rockwall (between $70^o$ and $80^o$) (Fig. 4.2). The absence of trees on the rockwall margin favours the exposition of the ice wall to the wind. At its maximum size, the ice wall grows up to 55 m high, 13.5 m wide and can accumulate up to a meter thick of ice in some locations. G-Amphi also faces north ($345^o$), but it grows on a 35 m relatively low angle rockwall (between $60^o$ and $65^o$) (Fig. 4.2). This ice wall looks well supported by the rockwall. Fringes of trees are present on both sides. The ice wall covers an area of approximately 750 square meters (30 m high and 25 m wide) and can reach thicknesses of up to 1.5 m. The G-195 ice wall forms on a small (10m) south-facing ($176^o$) almost vertical blasted cliff ($75^o$). The rockwall is located very close to the roadside and is well exposed to solar radiation. Considering the ice wall on the right of the picture only (Fig. 4.2, G-195), the ice covers the entire length of the cliff

and extends up to 6 m in width with thicknesses reaching 0.4 m in some places. All of them form from the freezing of underground and subsurface water resurgence. In the middle of winter, they don't show any freestanding structures (e.g. ice stalactites). They cover the rockwall as a uniform ice shell made of a complex aggregation of ice stalactites and ice concretions.
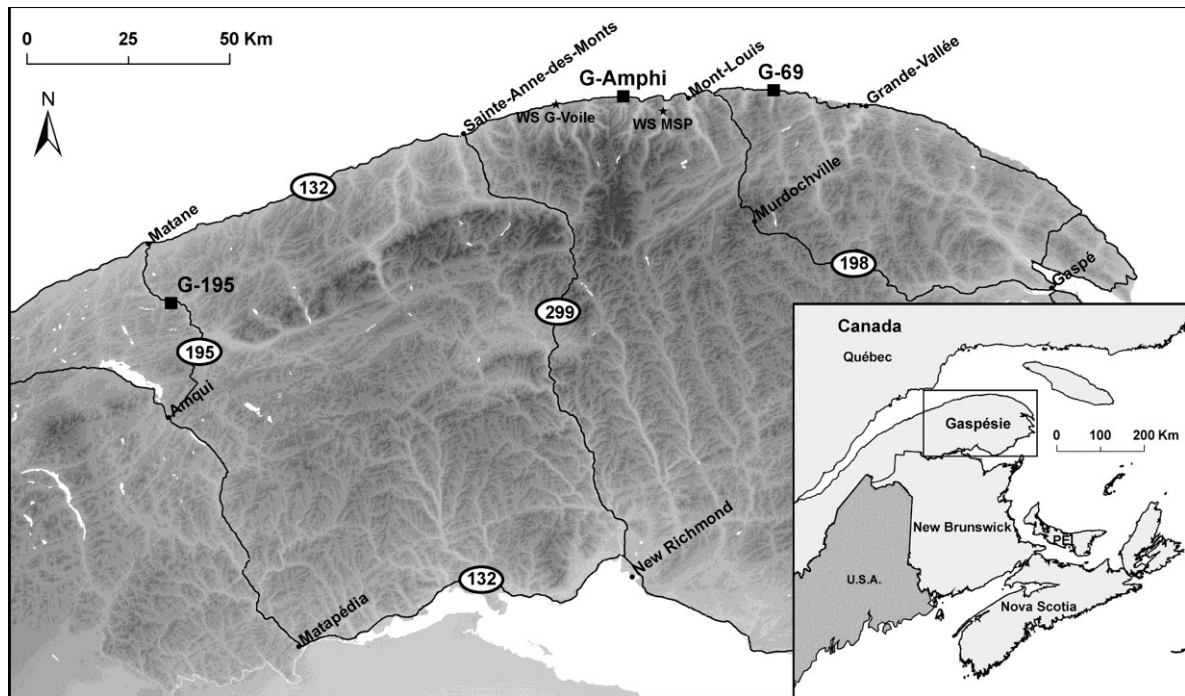


**Figure 4.1.** Study sites (G-69, G-Amphi and G-195), the Mont-Saint-Pierre (WS MSP) and the Voile de la Mariée (WS G-Voile) weather station location.
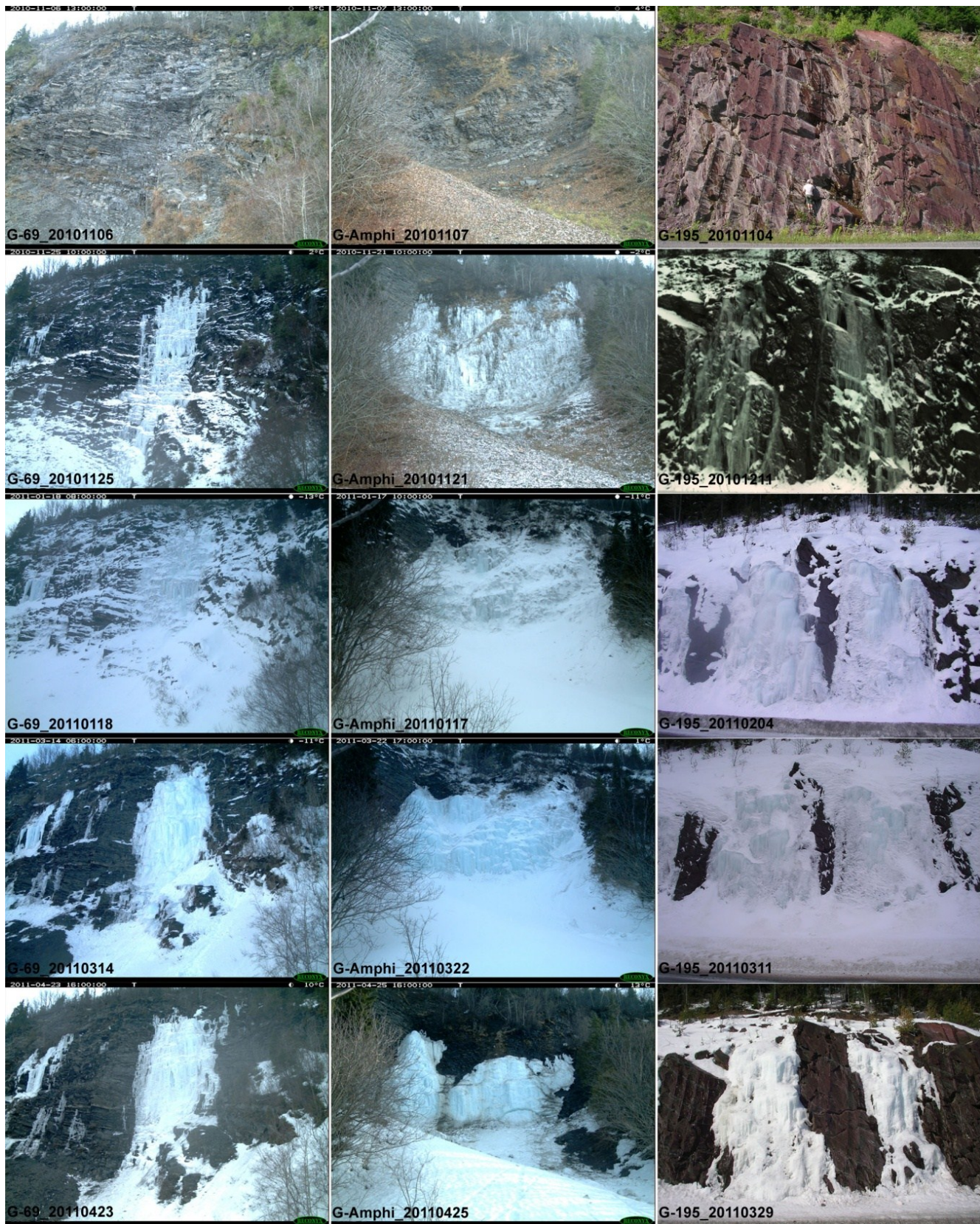
**Figure 4.2.** Ice walls (G-69, G-Amphi and G-195) evolution during the winter 2010-2011.

# 3. MEASUREMENTS

All the instrumentation was installed during the summer of 2009 and tested during the 2009-2010 winter season. The final setup was completed during the summer of 2010 and the measurements were conducted during the 2010-2011 cold season, from early October to the end of June. Instantaneous measurements were sampled at every 10 minutes but we used hourly mean and total precipitation values for the analysis of the data and to develop the model.

## 3.1. METEOROLOGICAL INSTRUMENTATION

Two independent and automatic weather stations (Onset: HOBO H21-002 Micro Station Data Logger and Campbell CR10X Data Logger) located near the coast of the St. Lawrence estuary at 4.5 m from a vertical rockwall (WS G-Voile) and in the Mont Saint-Pierre Valley, 3 km from the coast (WS-MSP) (Fig. 4.1) provided the general meteorological measurements. The first one (WS G-Voile) was equipped with a Wind Speed Smart Sensor (S-WCA-M003), a Relative Humidity Smart Sensor (S-THB-M002), a Barometric Pressure Smart Sensor (S-BPB-CM50) and three 12-Bit Temp Smart Sensors (S-TMB-M017). The temperature sensors were fixed to the rockwall surface and 38 cm and 80 cm deep underneath the surface. The Campbell weather station (WS-MSP) was equipped with a TE525 Tipping Bucket Rain Gage coupled with CS705 Snowfall Conversion Adapter.

An automatic weather station (Onset: HOBO H21-002 Micro Station Data Logger) was also installed at the top of each of the three ice wall sites. Three 12-Bit Temperature Smart Sensors (S-TMB-M017) were used to measure the air and the rockwall temperatures. The air temperature sensor was placed in a Solar Radiation Shield (RS1). The cable from the two other temperature sensors were stuck onto the rockwall surface using mastic epoxy glue while the head of the sensors were inserted in a hole at 1 cm and about 30 cm from the rockwall surface. Those temperature sensors where located at the first top quarter of the rockwall, approximately around where the resurgences seemed to appear. The temperature given by the one cm rockwall temperature sensor represents a close match to the water temperature at the entrance of the system. The solar radiation was measured with a Solar Radiation Sensor (Silicon Pyranometer, S-LIB-M003). The pyranometer was installed at the same vertical angle and orientation as the ice wall. Its measurement range is from 0 to

1280 W·m$^{-2}$ over a spectral range of 300 to 1100 nm. Finally, the ice-rock interface temperature was measured with a TidbiT v2 Water Temperature Data Logger (UTBI-001) bolted to the rockwall surface at 3 to 5 meters from the bottom of the ice walls. The recorded temperature by this sensor is a good estimation of the water temperature at the exit of the ice system.

Unfortunately, the ice-rock temperature sensor and the one cm rockwall temperature sensor at G-69 were damaged by a falling tree before the beginning of the study and the 35 cm rockwall sensor was damaged after only one month worth of measurements. This caused a 7 days interruption in the solar radiation measurements between the 15$^{th}$ and the 22$^{nd}$ of December. For modeling purposes, we therefore used an estimated radiation value corresponding to the mean pyranometer value 14 days before and after this period. During the melting process and immediately before the G-Amphi ice wall collapsed, both the rockwall temperature sensor and pyranometer stopped working properly for two short periods of 3 to 4 days between the 7$^{th}$ and 10$^{th}$ of April and again between the 22$^{nd}$ and the 25$^{th}$. Here, we also used a rough radiation value corresponding to the mean pyranometer value 14 days before and after these periods.

### 3.2. ICE WALLS EVOLUTION

Automatic digital cameras (Reconyx PC90) were installed at each study site to monitor ice cover evolution. Ten pictures were taken daily from 08:00 to 17:00. Unfortunately, the camera at G-195 was stolen at the beginning of the study. Two videos were generated from this data for ice walls G-69 (Vid. 4.1) and G-Amphi (Vid. 4.2)[1]. They show the global ice walls evolution with two pictures a day (8h00 and 15h00 for G-69 and 9h00 and 15h00 for G-Amphi) starting November 15$^{th}$ 2010 and ending May 13$^{th}$ 2011.

### 3.3. ICE VOLUME EXTRACTION

The ice volume was calculated using terrestrial LiDAR measurements. The first step consists in developing a high-resolution triangulated irregular network model (HRTINM) from the LiDAR measurements. Then, by comparing successive HRTINMs it is possible to extract the ice volume change between measurements (Fig. 4.4). The HRTINMs are

---

[1]Electronic supplementary material (videos): 29924vid4-1.avi and 29924vid4-2.avi

calculated from LiDAR measurements performed using a Leica Scan Station 2 and the Leica Geosystems Software Cyclone 7.1. Details concerning LiDAR specifications and ice volume extraction steps are described in chapter 3.

A total of 27 scans were done during the rockwall icings growing and melting season (10 at G-69, 8 at G-Amphi and 9 at G-195). The scans were performed at 30 to 50 m from the base of the ice walls and about 60 to 100 m from the top using a 5 mm resolution at 45 m. Point clouds were not scattered in depth on the ice walls surfaces. They were resampled at a 20 mm resolution and trimmed to eliminate the bordering vegetation and the snow accumulation at the foot of the ice walls. We extracted the same surface area from each point clouds. The calculated ice volume does not represent the total ice accumulation but rather a lower estimate (probably between 80 to 90%). At the end, we extracted the HRTINMs volume using the Mesh Volume function in Cyclone 7.1. The given volume is the difference between the HRTINMs and a reference surface (Fig. 4.4). The reference surfaced used was obtained by the extraction of a HRTINM from the scan of the almost dry rockwall's surface in September 2010. The differences represent the ice volume accumulation at the moment of the scan. For a more detailed description of the method we recommend Rabatel & al. (2008) and James & al. (2006).

The total uncertainty ($\sigma_{tot}$) can be estimated as follows (Baltsavias 1999; Rabatel & al. 2008):

$$\sigma_{tot} = \sqrt{\sigma_1^2 + \sigma_2^2 + \sigma_3^2 + \sigma_4^2} \qquad (4.1)$$

where $\sigma_1$-$\sigma_4$ represent the different independent processing errors described in chapter 3. Because the climatic conditions during the scanning acquisition process were good, except for December 10th scans, the error related to the environment ($\sigma_4$) is probably negligible. On December 10th, a minor snowfall reduced the quality of the acquired point cloud images. Many points representing snowflakes had to be removed before the generation of the HRTINM. The few remaining points, too close from the ice surface to be removed, caused a slight overestimation of the ice volume. Furthermore, the error associated with the scan surface is difficult to estimate. Even if the ice wall surface was generally dry, some limited zones were lubricated by localized flow on the ice surface. The point cloud

resolution over these wet zones wasn't as high as on the remaining surface. It locally affects the size of the mesh, but we were not able to estimate the exact error associated with this phenomenon. This leads to a minimum total uncertainty of 21 mm (G-195), 22 mm (G-Amphi) and 22.5 mm (G-69) on the cut surfaces areas. This represents a minimum absolute error of 1 m$^3$ (G-195), 9.4 m$^3$ (G-Amphi) and 15.8 m$^3$ (G-69) on the calculated ice volume. Additionally, the LiDAR measurement only leads to a precise reconstruction of the external shell of the ice walls. Even if the space between the ice covers and the rock surface seems insignificant (less than 1 or 2 mm where there is water flow), especially during the growing process, it remains impossible to estimate the total volume of the void between the ice walls and the rock wall surface. Visual inspection did not convince us that larges voids had formed during the melting process or before the collapse of the ice walls. We believe that this method yields the most precise measurements of the ice walls volumes.
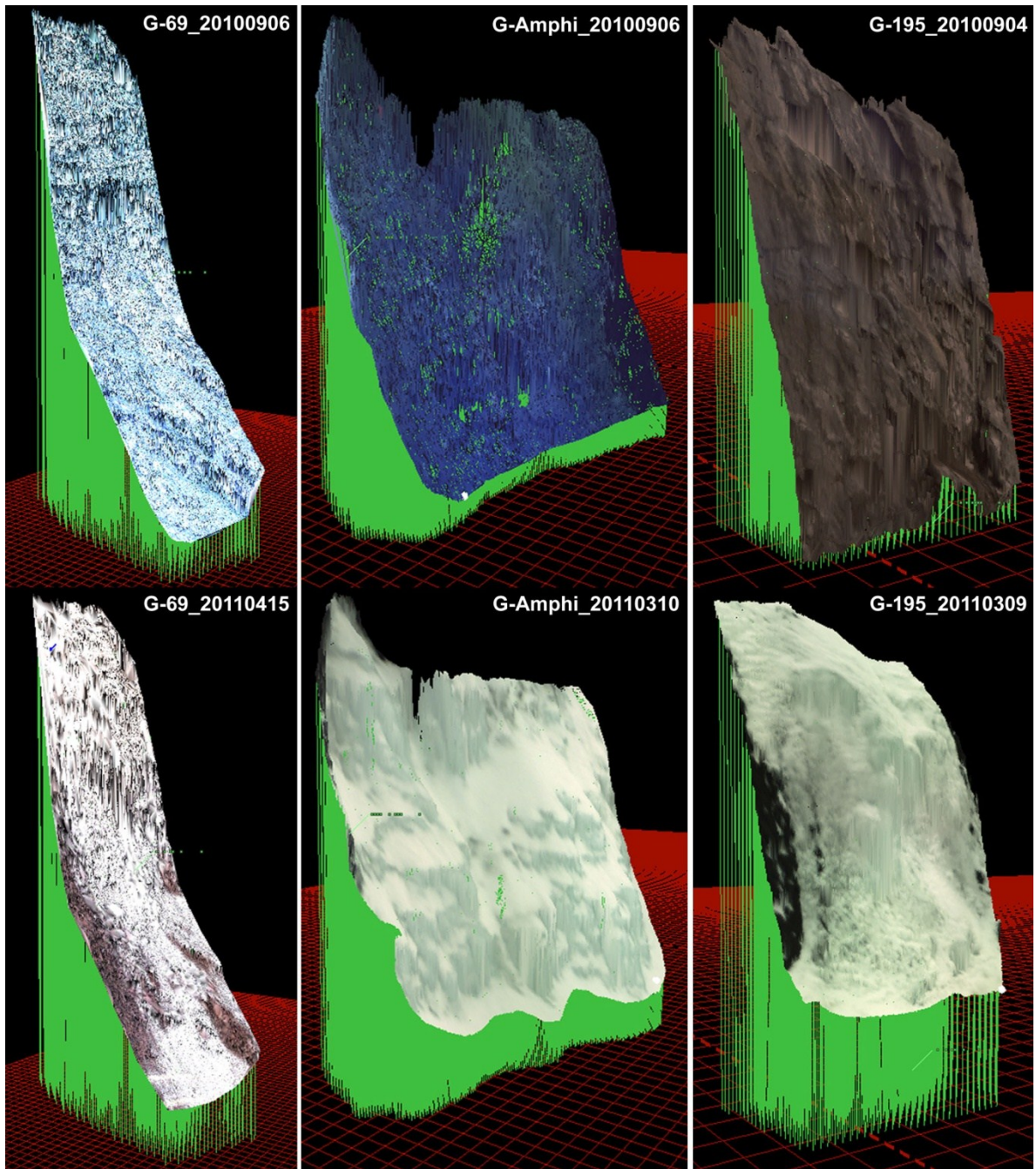
**Figure 4.3.** Examples of the computation of the ice walls volume for the three study site (G-69, G-Amphi and G-195). The volume between the reference plan (September 4th and 6th 2010) and the icy surface topography is computed for each date using the Mesh Volume function in Cyclone 7.1. The difference between the volume calculation on a given date and the volume of the reference surface topography gives the volume of ice.

## 4. METEOROLOGICAL CONDITIONS AND ICE WALLS EVOLUTION

We focus here on presenting the meteorological conditions in relation with the ice volume evolution of the ice walls. Figure 4.4 shows the liquid and solid (in water equivalent) precipitation recorded at the WS MSP weather station. The wind speed and relative humidity recorded at the WS G-Voile weather station are also presented. Figures 4.5, 4.6 and 4.7 present the data collected in the vicinity of the three studied ice walls. The dotted line between the measured ice volumes represents a linear hypothetical ice volume evolution. The path is clearly fluctuating more than what is presented. For example, between the ice volume measurements of November 26th, December 10th and 23rd there are two short periods where the ice covers disappeared completely (see the shaded surface in figures 4.5 and 4.6, and the videos 4.1 and 4.2 in the supplementary data).

At the beginning of the ice growing season, the rain events (days 20-21 and 28-31) are well synchronized with the periods without ice (Fig. 4.5, 4.6 and 4.7). But, the correspondence between liquid precipitations and the late season rain events (day 140 and later) is not as obvious. Based on these observations, the role of precipitations remains unclear. Warm liquid precipitation combined with the runoff water should increase the melting rate of the ice walls. In spring, it might accelerate the snowmelt and increase the ground-water and liquid runoff discharge over the ice walls. After December 23rd (day 38), two major snow events (day 42 and 72) seem to correspond with an increasing growth rate period. It's possible that the snow accumulation over some ice structures participates in the ice wall growing process: the presence of snowflakes favours the crystallization process and the remaining snow re-crystallizes and forms thin crusty layers of ice over some ice ledges.

The relative humidity remains pretty high during the cold months of winter and it tends to decrease slightly when the temperature increases in spring (Fig. 4.4). Wind conditions are almost never completely calm and the frequency of events with hourly wind speed mean values close or over 10 m/s (36 km/h) is high along the coast (Fig. 4.4). It's not clear at this stage how these meteorological variables influence the ice walls evolution. But we suspect that the wind plays an important role in the sensible heat transfer at the water-air and ice-air interface. We also assume that a relatively low humidity will favour evaporation-sublimation and heat transfers to the air. Because the G-69 and G-Amphi ice walls are

facing north, only diffuse radiation is reaching the ice surface during winter (Fig. 4.5 and 4.6). There is still a daily fluctuation, but the order of magnitude is pretty low. At the end of January (around day 65), the incoming diffuse radiation slowly rises. Little direct solar radiation is received in the middle of the morning at G-69. But the incoming radiation comes at a high incident angle. Because the G-Amphi ice wall is located between fringes of trees, no direct solar radiation is ever received. There's no doubt that the direct solar radiation received on the G-195 ice wall is affecting its evolution (Fig. 4.7). But it remains tricky to relate ice volume changes to variations in solar radiation. Two daily ice volume estimates would be required to correlate the effect of the daily solar variation on the ice wall global evolution, one in the morning and one during late afternoon.

The falling air temperature below 0°C initiates ice wall growth processes (Fig. 4.5, 4.6 and 4.7). Indeed, as soon as the air temperature drops under $0^{\circ}$C, ice forms on the rockwalls. The ice walls growth begins with the formation of many individual ice stalactites, ice crusts issued from the freezing of water runoff over sub-vertical rock faces and ice concretions (see figure 4.2 and videos 4.1 and 4.2 in the supplementary data). Bianchi (2004), Gauthier (2008), Gauthier & al. (2012) and Montagnat & al. (2010) all give a good description on how those structures grow, evolve and eventually merge into a massive macrostructure of ice. Under low discharge, as observed over the studied ice walls, the water first flows over the rockwall and around the different structures. During this early stage of formation, the water is constantly in contact with the atmosphere. As the structures grow and merge together, the flowing water is gradually isolated from the outside environment. However, several events of water overflow and runoff over the outside surface of the ice walls were observed even when the ice wall covers the entire rockwall surface. At G-195, we observed that ice mainly forms during the night and seems to remain steady during the day, an effect that wasn't observed on the two north-facing ice walls. When the ice structures are still thin and fragile, the ice can rapidly vanish if the temperature rises above the melting point. Because air temperature fluctuations highly control the formation of ice, calculating the freezing degree-hours (FDH) can adequately describe the ice walls evolution (Montagnat and others, 2010):

$$FDH = \int_{t_0}^{t}(T_f - T_a)\mathrm{dt} \tag{4.2}$$

where $T_f$ is the freezing point of water and $T_a$ the mean hourly air temperature. The FDH was calculated with an hourly time step (t), starting November 15th, 2010 at 00h00 with a minimum value of 0.

At the beginning of the growing process, the FDH shows a little lag with the measured ice volume accumulation. The rapid ice growth and decay at the beginning of the ice wall formation can hardly be described by this parameter. When the air temperature constantly remains under zero, ice forms rapidly. An almost linear ice volume evolution is observed. During this fast growth stage, the FDH follows the ice volume linear growth tendency. Around mid-march (day 120), the ice walls growth rate slightly decreases (Fig. 4.5, 4.6 and 4.7). An asymptotic growth behavior is noticed, especially at G-69. A similar behavior could have been observed at G-Amphi, but no LiDAR measurements were performed after March 30th. The gray dash arrow on Figure 4.6 represents a more probable ice volume evolution. During this period, the air temperature oscillates around the melting point and the FDH tends to level off. Unlike what Montagnat & al. (2010) observed on a frozen waterfall of the French alps, the FDH doesn't show a linear tendency during this late season stage. Rather, it seems to follow an asymptotic tendency.

The temperature at the ice-rock interface and at the rockwall surface (1 cm) closely follows air temperature fluctuations at the beginning of the growing process (Fig. 4.6 and 4.7). The ice is thin or absent and heat is transmitted to the rockwall. At 35 cm, the temperature at the interface also follows air temperature fluctuations but with a smaller amplitude (Fig. 4.5, 4.6 and 4.7). These effects are even more noticeable on the G-195 rockwall where the fluctuations are accentuated by a greater exposure to solar radiations (Fig. 4.7). As soon as a thick ice cover is formed, the surface and inside rock temperature fluctuations rapidly decrease (around December 25th, day 42) (Fig. 4.6). This effect is also noticeable on the G-195 ice wall (Fig. 4.7). After this stage, the rockwall and ice-rock interface temperatures drop below zero. Even if our observations show that water still flows in some places between the ice cover and the rockwall, this phenomenon reveals that ice locally forms directly on the rockwall. In addition to resting on the ledges and the cragginess of the rockwall, it suggests that the ice walls are also supported by the formation and expansion of ice inside the microstructures of the rockwall surface, i.e. that the ice cover adfreezes to the

rock face. These ice anchors formation could explain the capacity of ice walls to remain solidly attached to rockwalls even after high tensile stresses triggered by large air temperature fluctuations or a rapid cooling of the air.

When the air temperature rises (e.g.: day 118 and 122), the ice-rock interface temperature rises above the melting point and the ice anchors on the rockwall gradually melt (Fig. 4.6 and 4.7). At G-195, those events correspond with the rapid melting and collapse of the ice wall. After that, the rock surface and ice-rock interface temperatures highly fluctuate along with the air temperature and solar radiations (Fig. 4.7). At G-Amphi and G-69, the melting process takes longer. The thick ice cover still absorbs heat and the ice anchors remains strong, thus supporting the ice wall onto the rockwall. At beginning of April (days 137 to 155), a series of rapid air temperature changes ($4,5^{o}$C to $6^{o}$C in 14 to 20 hours) but around $0^{o}$C (ranging from $4.3^{o}$C to $-7.6^{o}$C) provoked the opening of fractures on the G-Amphi ice wall (see the video 4.2 in the supplementary data), but it remained anchored to the rockwall. The low angle cliff on which this ice wall has formed may have increased its stability. On April $17^{th}$ 2011 (day 153), the rockwall temperatures drastically rose. It is possible that an opening has formed above the sensors. The gap in the rockwall temperatures and solar radiation data before and after this event may have been caused by a fracture opening or a slow movement of the ice cover. Alternatively, the sensors wire may have stretched resulting in a dysfunction of the logger. Eventually, the melting of the ice anchors on the rockwall could not support the massive ice covers which resulted in a rapid and complete collapse of the ice walls during the night of April $25^{th}$ 2011, on day 161. The same dynamics occurred before the collapse of G-69 during the night of April $28^{th}$ 2011, on day 164 (Vid. 4.1). It's also possible to observe a slight increase of the water flow after the ice walls collapse. It even seems a little stronger than at the beginning of the freezing process (see the videos 4.1 and 4.2 in the supplementary data).
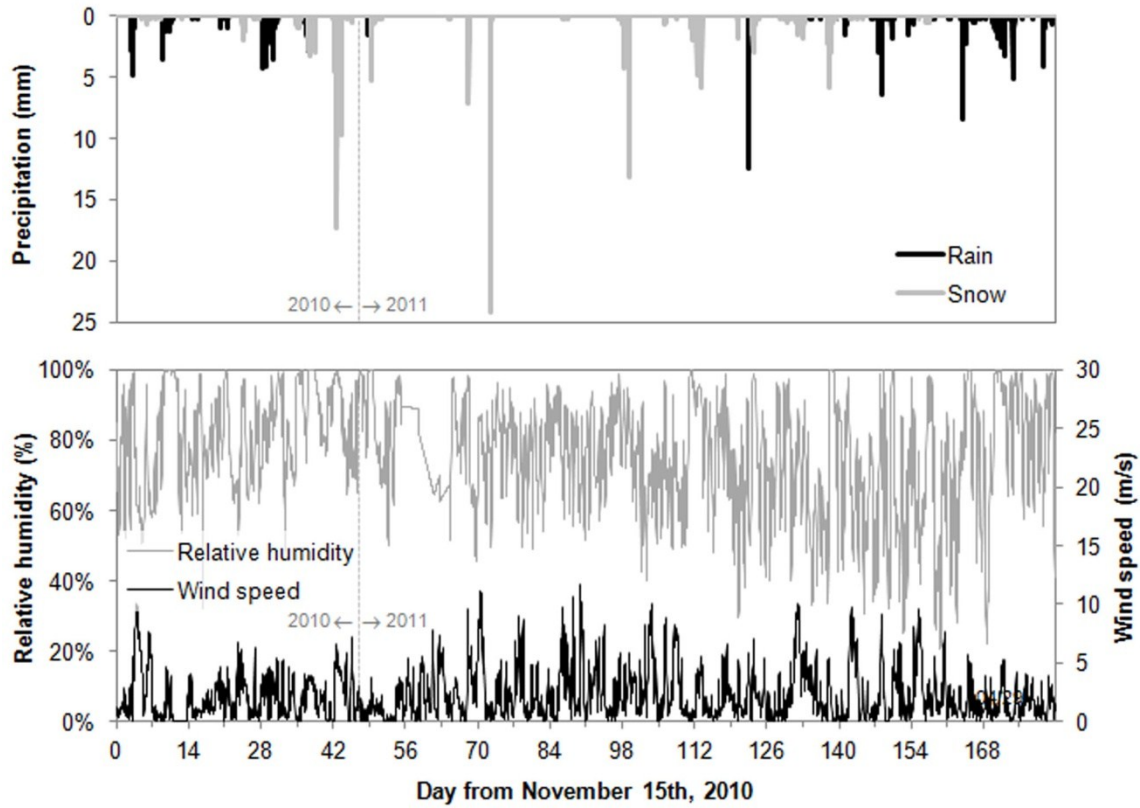
**Figure 4.4.** The total hourly liquid and solid precipitation at the Mont-Saint-Pierre weather station (WS MSP) and the mean hourly relative humidity and wind speed at the Voile de la Mariée weather station (WS G-Voile) from November 15th 2010 (day 0) to may 15th 2011 (day 181).
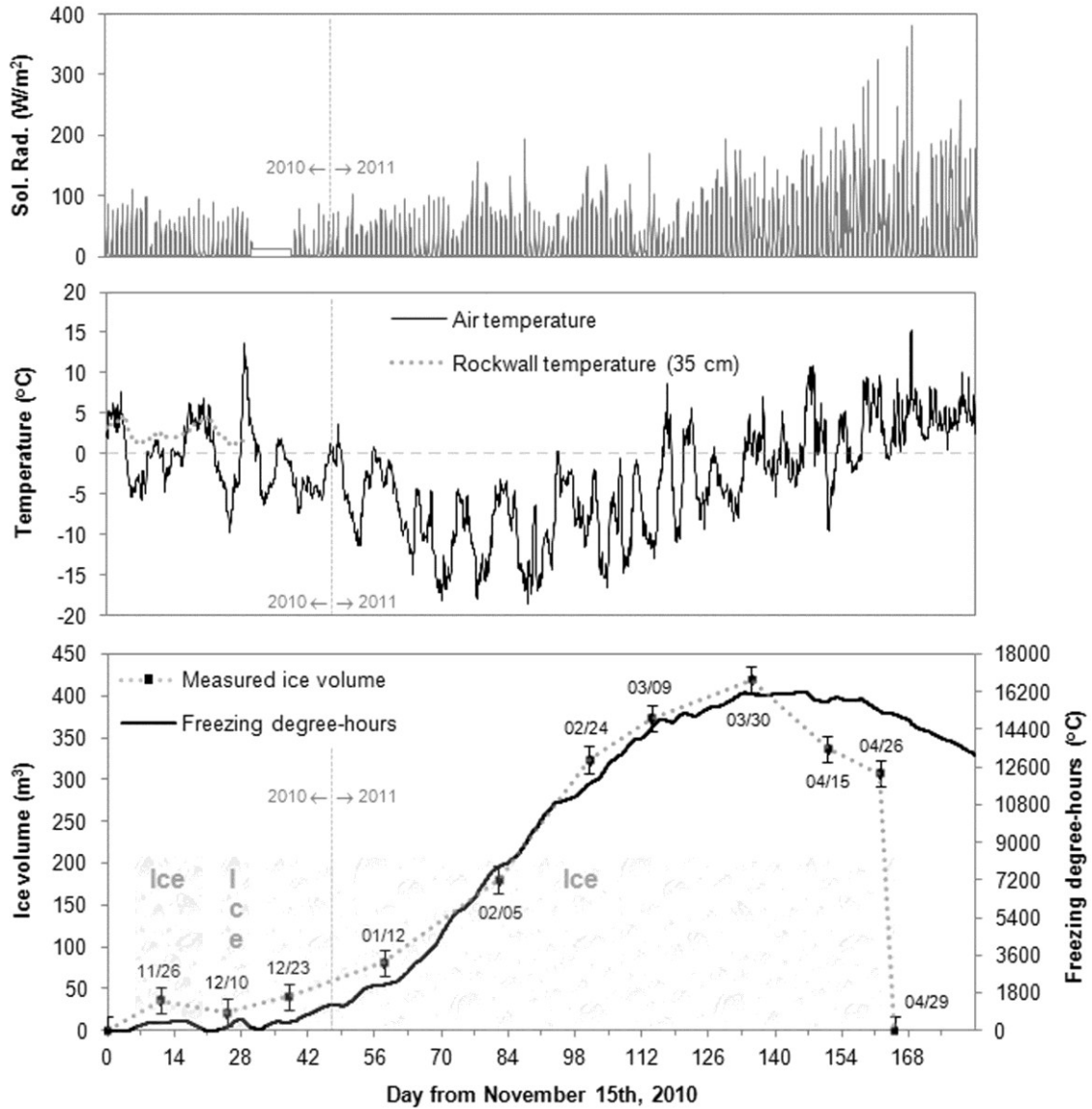
**Figure 4.5.** Measured ice wall volume (G-69), freezing degree-hours, air temperature, rockwall temperature at 35 cm deep and solar radiation in hour from November 15th 2010 (day 0) to may 15th 2011 (day 181). N.B.: The shaded surface represents the time period when the rockwall is covered by ice.
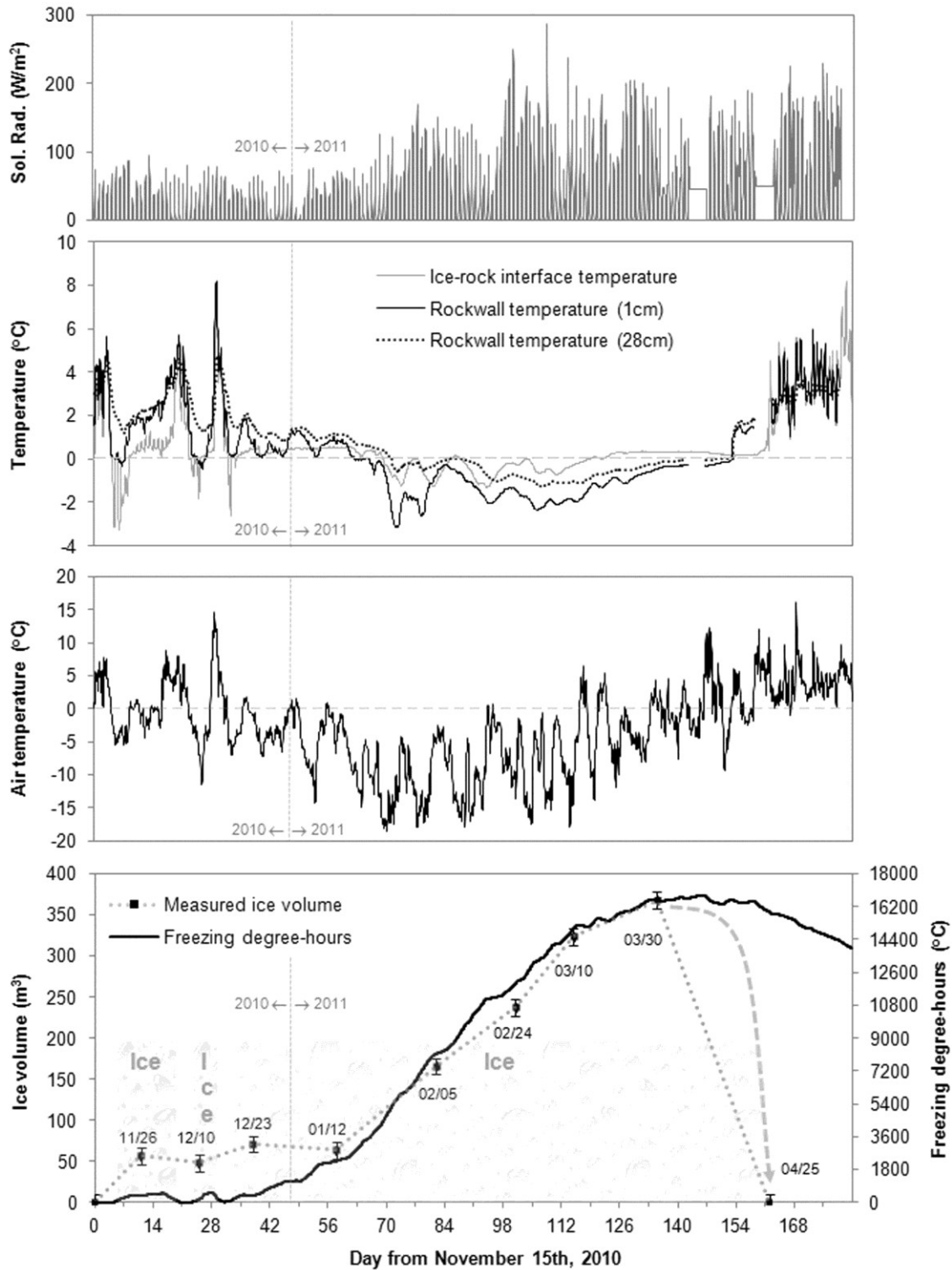
**Figure 4.6.** Measured ice wall volume (G-Amphi), freezing degree-hours, air temperature, ice-rock interface temperature, rockwall temperature at 1 cm and 28 cm deep and solar radiation in hour from November 15th 2010 (day 0) to may 15th 2011 (day 181). N.B.: The shaded surface represent the time period when the rockwall is covered by ice and the gray dash arrow represents a more probable ice wall volume evolution.

94
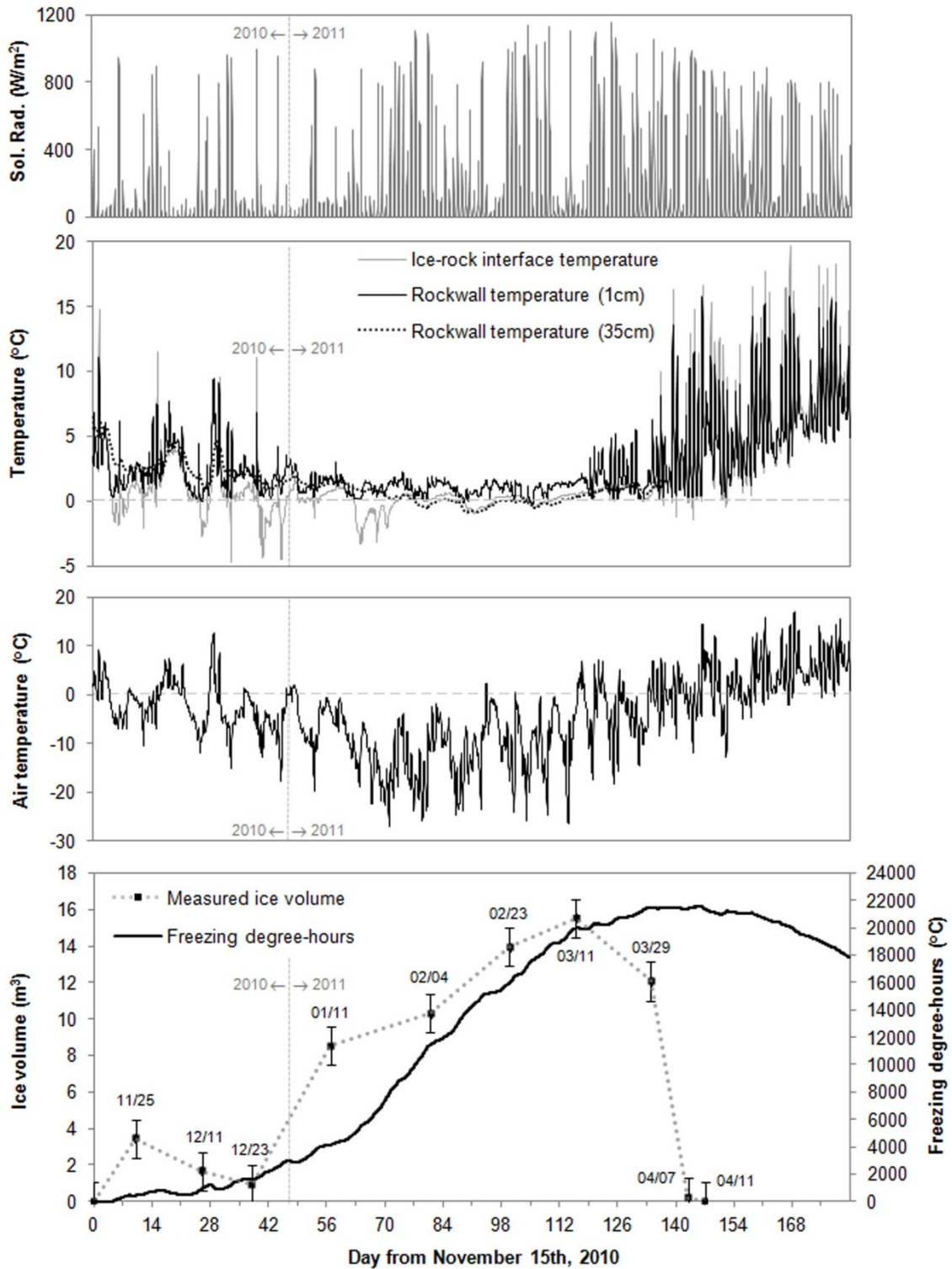
**Figure 4.7.** Measured ice wall volume (G-195), freezing degree-hours, air temperature, ice-rock interface temperature, rockwall temperature at 1 cm and 35 cm deep and solar radiation in hour from November 15th 2010 (day 0) to may 15th 2011 (day 181).

# 5. MODELLING

The ice wall growth and decay process is controlled by a complex and highly fluctuating series of factors: from the atmospheric conditions (air temperature, radiation and evaporation) that affect the heat transfer from the flowing water and the ice surface to the ambient air to the temperature and the heat flux coming from the rock wall and the underlying topography over which the ice wall develops. Furthermore, the water temperature, the precipitations, the flow of water and its spatial distribution over the rockwall all play a major role in the formation of the ice walls.

To better understand the role played by the variables influencing the ice wall growth and decay, we first suggest a thermodynamic model base on the assumption that the entire ice wall evolution is uniform over time. The different components of the energy balance transfer heat to or out of the water flow at a temperature close to the freezing point. We also propose a model based on a simple FDH calculation and one based on an FDH calculation that adds on the radiative heat budget.

The models were optimized by seeking the best coefficient of determination ($R^2$) between the calculated and measured ice volumes. The $R^2$ is frequently used as the sole criterion for assessments of model performances (e.g. Gottlieb 1980; Hock 1999). Additionally, graphic inspection has proved just as useful in determining good empirical constants. The best $R^2$ appeared when the calculated ice volume matched the fast growing and asymptotic ice volume evolution periods (between mid January (day 58) and the end of March 2011 (day 136)).

## 5.1. THERMODYNAMIC MODEL (THERMO)

Here, we propose an energy budget based on theoretical considerations mainly inspired by ice stalactites growth models (e.g. Maeno & al. 1994b; Makkonen 1988), river ice and icing growth models (e.g. Ashton 1989; Hu & al. 1999; Schohl & Ettema 1986), ice accretion accumulation models (e.g. Jones 1996; Makkonen 2000) and frazil ice production models (e.g. Hanley & Michel 1977; Ye & Doering 2004). The different heat fluxes associated with water flowing down a vertical and simplified plane are presented in figure 4.8. In this simplified model, the ice forms in the flowing water and only a fraction of this ice is retained in the system and anchors to the rockwall to contribute to the ice wall volume (V).

The overage is the percentage of ice produced that evacuates the system (% ice in figure 4.8). At any time during the freezing or melting process the energy balance can be written as:

$$0 = Q_{cv} + Q_{evap} + Q_{cc} + Q_{rad} + Q_w + Q_{ice} \qquad (4.3)$$

where $Q_{cv}$ and $Q_{evap}$ are the sensible and latent heat flux at the air-water interface respectively. $Q_{rad}$ is the radiative heat budget. $Q_{cc}$ is the conductive heat brought by the rockwall to the ice wall. $Q_w$ is the sensible heat carried by the flowing water and $Q_{ice}$ is the latent heat release during the ice formation process. In the model, we assume that the flowing water's temperature around the forming ice is close to the freezing point of water ($T_f = 0^oC$).
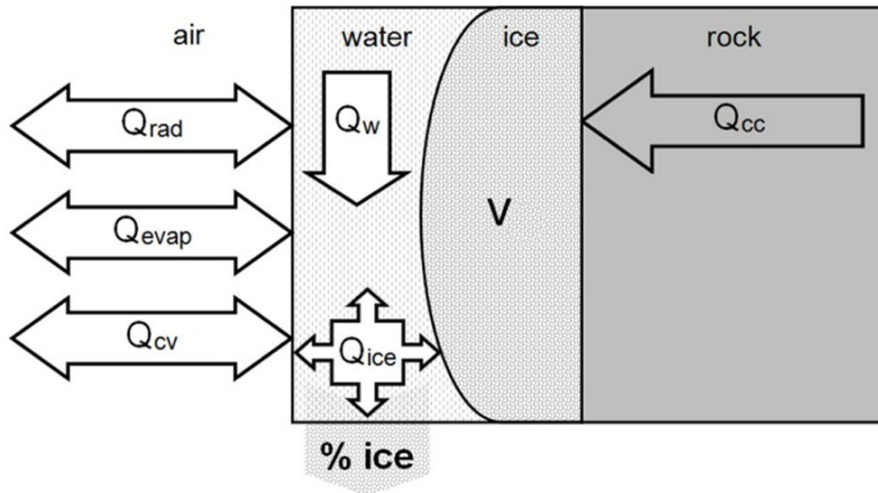


**Figure 4.8.** Schematic illustration of the ice wall growth and decay thermodynamic model (Thermo).

As the water falls down on and over the rockwall, the air convection around the flow either evacuate or bring energy to the water. The convective sensible and latent heat transfer ($Q_{cv}$ and $Q_{evap}$) between the air and the water can be expressed as in equations 3.5 and 3.7 (chapter 3). The same bulk aerodynamic approach was used to calculate the heat transfer coefficient ($h_{wa}$) (eq. 3.6, chapter 3). By using this approach, we assume that $h_{wa}$ varies

proportionally to wind speed. The bulk-exchange coefficient ($K_s$) was determined empirically and the values are presented in table 4.1 for the three ice walls studied.

The net radiation budget ($Q_{rad}$) at ice walls surfaces and the conductive heat flux coming from the rockwall ($Q_{cc}$) were also calculated as proposed in chapter 3 (equations 3.8 and 3.10). We also used an albedo value of 0.5 which represents a crude qualitative estimation for the whole ice wall growth and decay season, but a representative mean value for different types of natural ice (e.g. Bolsenga 1969; Hock 2005; Hu & al. 1999; Oke 1987).

The fifth term in the energy balance equation represents the heat flux carried by the flowing water ($Q_w$) and it can be written as:

$$Q_w = \frac{C_w D_{in}(\Delta T_w)}{S} \tag{4.4}$$

where $C_w$ is the specific heat of water, $D_{in}$ is the incoming water discharge, $\Delta T_w$ is the water temperature change between the top and the bottom of the ice wall and S is the mean surface area covered by the ice wall. Because the water sources of the three ice walls come from low discharge, underground and subsurface ground-water resurgences at the top of the rockwalls, no water flow measurement were performed. According to Heath (1983), the average saturated hydraulic conductivity for fractured shale and sandstone is around $10^{-7}$ cm·s$^{-1}$ and between $10^{-4}$ and $10^{-2}$ cm·s$^{-1}$ for silty-sandy deposits (in Dingman 2008). Assuming that the ground-water resurgence comes out from the whole rockwall and surface deposit (or regolith) areas, we decided to use a constant value of 1 L·s$^{-1}$ (kg·s$^{-1}$). This value is a very crude estimate $D_{in}$ can also be used as an adjustable empirical variable. Different values were tested and the results are presented below. For the simulation, we used a constant $\Delta T_w$ value of 0.5$^o$C. It represents the mean temperature difference recorded for the whole season between the 1 cm rockwall temperature sensor and the ice-rock interface temperature at G-Amphi and G-195. We also used this value for the G-69 ice walls.

When the temperature drops below 0°C and a sufficient amount of heat is lost through the environment, ice forms in the flowing water. The latent heat release during the freezing process ($Q_{ice}$) is of the same form as equation 3.12 and the energy balance (eq. 4.3) can then

be used to estimate the ice production rate dM/dt (eq. 3.13) (chapter 3). Finally, the ice fixation rate on the rockwall dV/dt is given by:

$$\frac{dV}{dt} = \frac{\frac{dM}{dt}}{\rho_i} * \%IF \tag{4.5}$$

where $\rho_i$ is the density of ice. A mean value of 880 kg·m$^{-3}$ was measured from different ice stalactites and ice concretion samples using a CT-scan (e.g. Boespflug & al. 1994; Calmels & Allard 2004; Hounsfield 1973; Knoll 1989). As described in chapter 3, %IF is an empirical value that represents the percentage of ice withheld in the system and anchored to the rockwall. A value of 5% (0.05) was first used to model the three ice walls volume evolution. With $K_s$, %IF and $D_{in}$ remain the more critical adjustable variables in the model. A sensitivity analysis on %IF and $D_{in}$ was also performed to test the robustness of the model to parameters change.

**Table 4.1.** Value of the constants for the three models proposed.

| Ice walls | Models | Thermo | | | | FDH | FDH+Qrad | |
|---|---|---|---|---|---|---|---|---|
| | Constants* | $K_s$ | %If | $D_{in}$ | $\Delta T_w$ | FDHF | FDHF | QRF |
| G-69 | | 0.006 | 0.05 | 1 | 0.5 | 0.025 | 0.02 | 5x10$^{-7}$ |
| G-Amphi | | 0.008 | 0.05 | 1 | 0.5 | 0.021 | 0.021 | 1x10$^{-7}$ |
| G-195 | | 0.00125 | 0.05 | 1 | 0.5 | 0.0008 | 0.0008 | 1x10$^{-7}$ |

\* The bulk-exchange coefficient $K_s$ and the percentage of ice withheld in the system %IF are dimensionless number, the incoming water flows $D_{in}$ are given in L·s$^{-1}$ (or kg·s$^{-1}$), the water temperature change between the top and the bottom of the ice walls $\Delta T_w$ in °C, the freezing degree-hours factor FDHF in m$^3$·h$^{-1}$·°C$^{-1}$ and the radiative heat budget factor QRF in m$^3$·h$^{-1}$·W$^{-1}$·m$^2$.

## 5.2. FREEZING DEGREE-HOURS MODEL (FDH)

A minimalist model is also proposed. It was previously stated that the air temperature is certainly the main variable controlling ice wall growth and decay (Gauthier 2008; Gauthier & al. 2012; Montagnat & al. 2010). As the easiest and most reliable readily available meteorological data, air temperature is widely used as a sole variable to develop empirical ice melt and freeze models (e.g. Ambach 1988; Ashton 1989; Braithwaite 1995; Hock

2003; Montagnat & al. 2010; Shen & Yapa 1985; Singh & al. 2000). A factor of proportionality is normally used to balance the temperature units with the growing or melting rate of the water-ice system. The volume of ice at each time step can be calculated as follows:

$$\frac{dV}{dt} = (T_f - T_a) * FDHF \tag{4.6}$$

where FDHF is the freezing degree-hours factor expressed in $m^3 \cdot h^{-1} \cdot {}^{\circ}C^{-1}$. FDHF is obtained empirically by fitting the FDH model with the ice volume evolution curves. The values of the FDHF for the three ice walls studied are given in table 4.1. The goal is to evaluate if a model solely based on the FDH calculation can reproduce, with the same precision, the ice wall volume's evolution

## 5.3. FREEZING DEGREE-HOURS AND RADIATION BUDGET MODEL (FDH+QRAD)

Observations also show that ice walls or ice cascades exposed to solar radiation tend to form and melt periodically at the beginning of the cold season and to melt more rapidly at spring time (Gauthier 2008; Gauthier & al. 2012). To overcome the problem of solar radiation exposure, a model including the FDH calculation combined with the radiative heat budget was developed, an approach also used to improve the spatial and temporal variability in snow and glacier melt modelling (e.g. Cazorzi & Dalla Fontana 1996; Hock 1999; Hock 2003). The model can be expressed as:

$$\frac{dV}{dt} = \left( \left( T_f - T_a \right) * FDHF \right) + \left( Q_{rad} * QRF \right) \tag{4.7}$$

where $Q_{rad}$ can be stated as in equation 3.8 and QRF is a factor of proportionality expressed as the radiative heat budget factor expressed in $m^3 \cdot h^{-1} \cdot W^{-1} \cdot m^2$. As FDHF, QRF is determined empirically. The values of FDHF and QRF for the three ice walls studied are given in table 4.1.

100

# 6. RESULTS AND DISCUSSION

## 6.1. ICE WALLS THERMODYNAMICS

Calculated and measured ice volume evolutions are provided in figure 4.9. Computing the ice volume from the thermodynamics model (Thermo) yields a good simulation of the overall ice volume evolution throughout the winter season. At the beginning of the ice formation, the Thermo model slightly underestimates the ice volume. But it simulates pretty well the periods with and without ice. When the air temperature consistently stays under 0°C, the ice walls rapidly grow (Fig. 4.5, 4.6 and 4.7). This fast growing period is well represented by the Thermo model (Fig. 4.9). The gap between the measured ice volume and the calculated ice volume rapidly decreases. The best model optimization is obtained when the Bulk exchange coefficient ($K_s$) is adjusted to fit this fast growing period (Fig. 4.9B). At G-195, the direct solar radiation received during the day induced a higher daily variability of the computed ice formed which agrees with field observations (Fig. 4.9A). The asymptotic ice evolution behaviour is also well rendered by the Thermo model. But unsurprisingly, the sudden collapse of the two north-facing ice walls (G-69 and G-Amphi) can't be simulated by the Thermo model. The model simulates the slow melting of the ice walls, but it can't predict the exact moment of the collapse. Moreover, the mechanical stress caused by large air temperature variations or rapid cooling can also result in a total or partial collapse of ice structures (Weiss & al. 2011): a behavior that cannot be reproduced by the model. At G-195, the model fits pretty well the decreasing ice volume. Instead of collapsing suddenly, the south-facing ice wall melts in place generating few collapsing ice structures.

From the analysis of the different heat exchange flux in the energy budget, it is possible to evaluate the importance of each term during the freezing and melting periods. Figure 4.10 shows representative examples of a 24 hour energy balance during freezing (February 10th, 2011: day 87) and melting (April 10th, 2011: day 146) periods. On February 10$^{th}$, along the northern Gaspésie coast, the mean air temperature revolved around -15$^{o}$C while the average wind speed frequently exceeded 15 km/h with many peaks over 30 km/h. In the surroundings of the G-195 ice wall, the mean air temperature was around -20$^{o}$C and the sky was clear with an average solar radiation received between 11:00 and 12:00 of 780 W/m$^2$. March 29$^{th}$, 2011 was a typical melting day of spring in northern Gaspésie. The mean daily

temperature was around 2$^o$C with a peak at 4.4$^o$C in the late afternoon. It was a clear day with 50% relative humidity and with wind speeds oscillating between 8 and 20 km/h. In the Matane river valley, near the G-195 ice wall, the mean daily air temperature was also around 2$^o$C, but slightly below 0$^o$C in the morning and the evening with a peak temperature of 7$^o$C in the afternoon. It was a sunny day, with an average global solar radiation over 1000 W/m$^2$ received between 10:00 and 13:00.

During cold, windy and sunny periods, the convective heat flux ($Q_{cv}$) was clearly the main factor responsible for the ice walls freezing process (Fig. 4.10A). The radiative heat budget ($Q_{rad}$) was of secondary importance at all study sites. The diffuse solar radiation received at the north-facing ice walls (G-69 and G-Amphi) was never high enough to completely counterbalance the emitted energy by the ice surface. At G-195, the sun radiation exposure clearly affected the growing process. During the night, in the morning and in the late afternoon, the radiation emitted by the ice surface (IR) coupled with $Q_{cv}$ favored the freezing process. But between 10:00 and 15:00, the solar radiation absorbed by the ice surface was enough to reverse the tendency and cause the melting of the ice cover.

During the melting period, the convective heat transfer ($Q_{cv}$) is the dominant heat flux on the north-facing ice walls (Fig. 4.10B). In the morning, the near 0$^o$C air temperature does not favour sensible heat transfer, but as soon as the temperature warms, this heat flux becomes the most important heat transfer process at the ice walls surfaces. Unlike during the short days of winter, solar radiation (G) becomes a major source of heat that induces ice melting at spring. The main energy flux responsible of the G-195 ice wall melt process comes almost entirely from the direct solar radiation. The sensible heat flux remains of secondary importance.
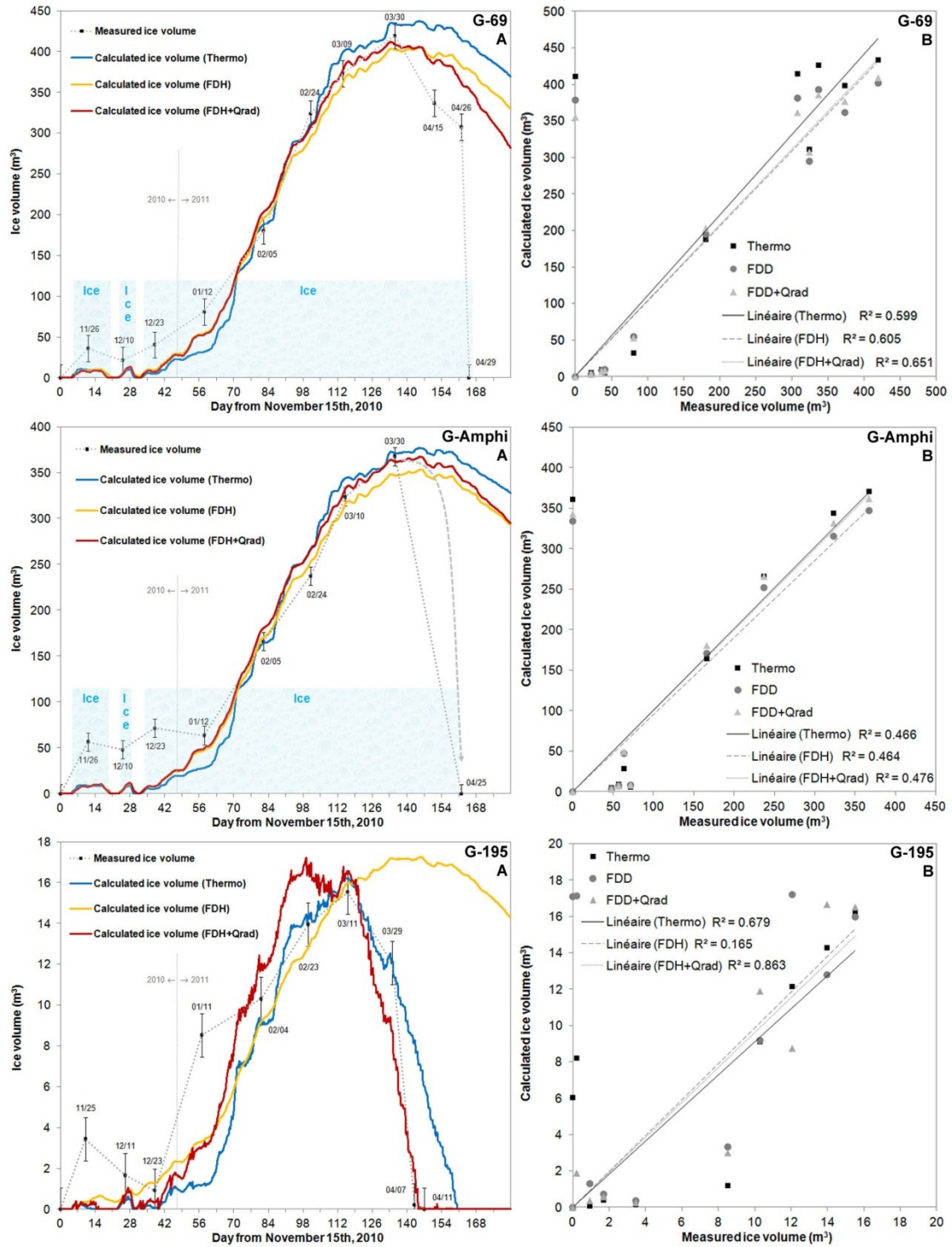
**Figure 4.9.** A) Calculated (Thermo, FDH and FDH+Qrad) and measured ice volume evolution at the three study sites (G-69, G-Amphi and G-195). B) Calculated (Thermo, FDH and FDH+Qrad) vs measured ice volume at the three study sites (G-69, G-Amphi and G-195). N.B.: Shaded surfaces in figure G-69 A and G-Amphi A represents the periods when the rockwall is covered by ice.
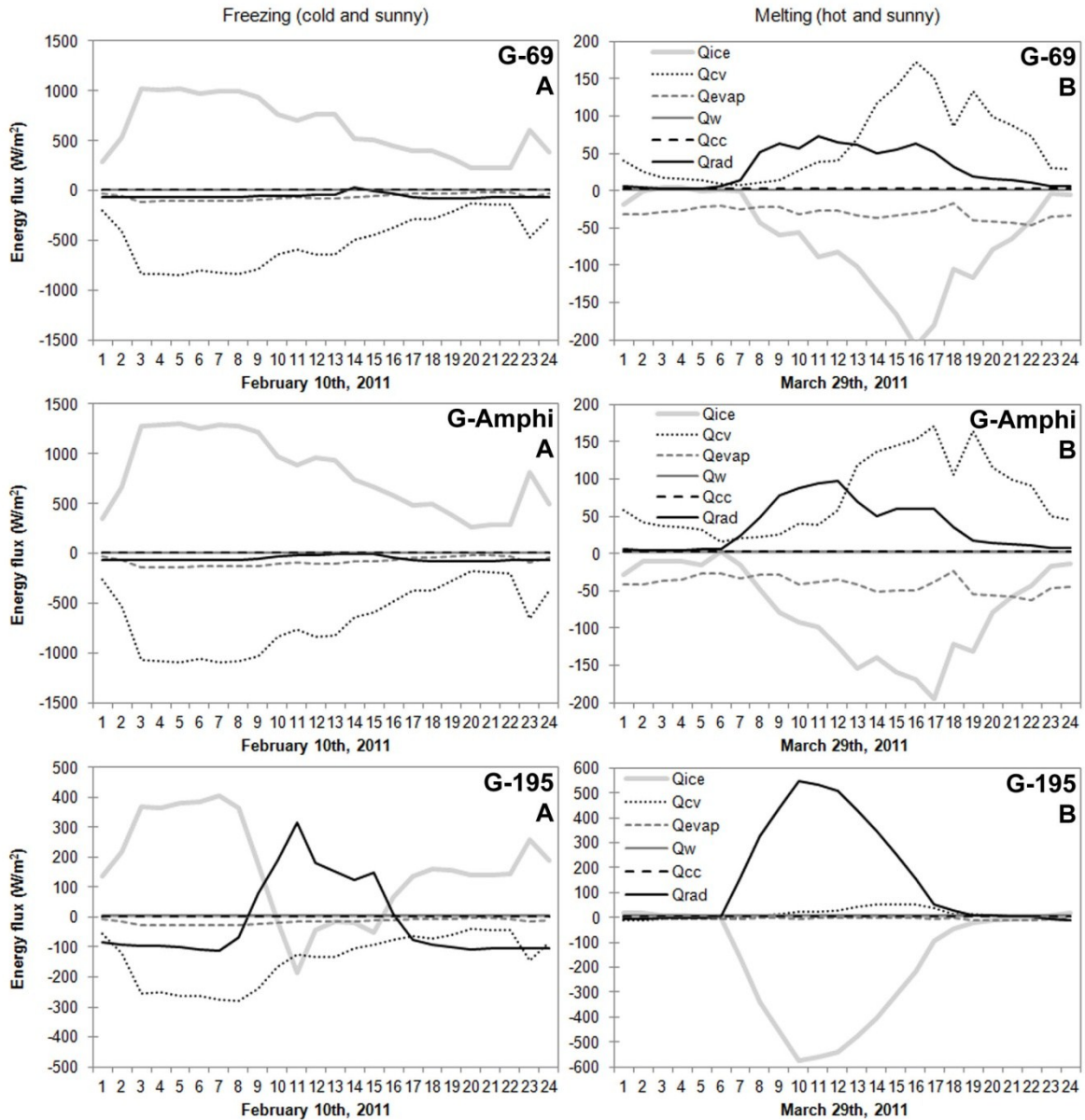
**Figure 4.10.** Examples of a 24 hour energy balances during a freezing (A: February 10th, 2011: day 87) and melting (B: April 10th, 2011: day 146) period at the three study sites (G-69, G-Amphi and G-195).

The latent heat flux ($Q_{evap}$) doesn't seem to play a major role during the freezing process (Fig. 4.10A). Because the relative humidity is directly related to the air temperature, the evaporation process is limited at cold air temperature or when the relative humidity is high. However, latent heat of evaporation tends to favour the ice walls growth process. The heat accumulated during the phase change process is evacuated from the ice walls system and released in the near atmosphere. When the temperature warms up, coupled with low relative humidity, the latent heat flux becomes more important, especially on the north-facing ice walls (Fig. 4.10, G-69 B and G-Amphi B). The energy evacuated from the ice walls system tends to slow the melting process.

Because we assumed that the conductive heat flux from the rockwall ($Q_{cc}$) is a positive constant of relatively low value, its contribution to the freezing or the melting process is almost negligible. But it tends to bring heat to the ice covers or to the flowing water. This marginal heat transfer may be partially responsible for the continuous liquid film which flows locally, at the ice-rock interface.

The constant value assigned to $D_{in}$ and $\Delta T_w$, leads to a constant, positive value of the sensible heat flux carried by the flowing water ($Q_w$) (Fig. 4.10). The value was however never high enough to significantly influence the freezing or the melting process. Even if we revise the value of $D_{in}$, the overall effect does not significantly affect the calculated ice volume evolution curves for the north-facing ice walls G-69 and G-Amphi (Fig. 4.11A). Because the surface area covered by those two ice walls is large (eq. 4.10), the energy is well distributed over the whole surface. In comparison, the surface area of the ice wall G-195 is small; a high incoming discharge value considerably influences the amplitude of the growing and melting process (Fig. 4.11C). To counterbalance the tendency, the empirical constant $K_s$ could be adjusted to redress the calculated ice volume curves. If we assume that the incoming underground water flow gradually decreases at the beginning of winter and increases while the snow cover melts in spring (Dingman 2008; Domenico & Schwartz 1990), these factors will increase the freezing process at the beginning of the ice walls formation and it will accelerate the melting process in spring. This could partially explain the gap between the calculated and measured ice volume at the beginning of the simulation.

Moreover, the increasing water flow at spring must accelerate the melting of the ice anchors on the rockwall and must influence the collapse of the ice walls.

The lag between the measured and the simulated value at the beginning of the simulation may also have been caused by a higher uncertainty in the ice volume estimation. A thin snow accumulation was present during the LiDAR measurement. In November, December and January, the thin ice cover may have been slightly overestimated because of the snow cover. Especially on December 23rd (along the northern Gaspésie coast) and January 11th (in the Matane river valley, road 195) when respectively 34 cm and 16 cm of snow had fallen the day before the LiDAR measurements. It is probable that the ice volume estimations of G-69 and G-Amphi performed on December 23rd and the G-195 ice volume estimation of January 11th were significantly overestimated because of the presence of a thick snow cover on different ice structures. This source of error then decreases as the ice cover thickens.

Another and even more significant source of error in the underestimation of the calculated ice volume during the early stage of formation comes from the ice walls growth itself and the limited capability of the model to simulate the fast and highly fluctuating ice volumes. At the beginning of the growth process, the water is always in contact with the surrounding air. The sensible heat transfer ($Q_{cv}$) is certainly higher during this early stage of formation than after the formation of a complete ice cover. As the ice cover forms, less water flows over the ice surface. The flowing water is gradually isolated from the outside environment. As suggested by Montagnat and others (2010), a conductive heat flux through the ice may represent better the reality during this advanced stage of formation. However, we observed frequent water overflow and runoffs over the ice surfaces, even in the middle of the winter. Using a higher value of %IF (e.g. 15%), we can calculate the first ice volume formed over the rockwalls, but then as soon as the temperature drops and stays below zero, the model considerably overestimates the ice volume (Fig. 4.11B).
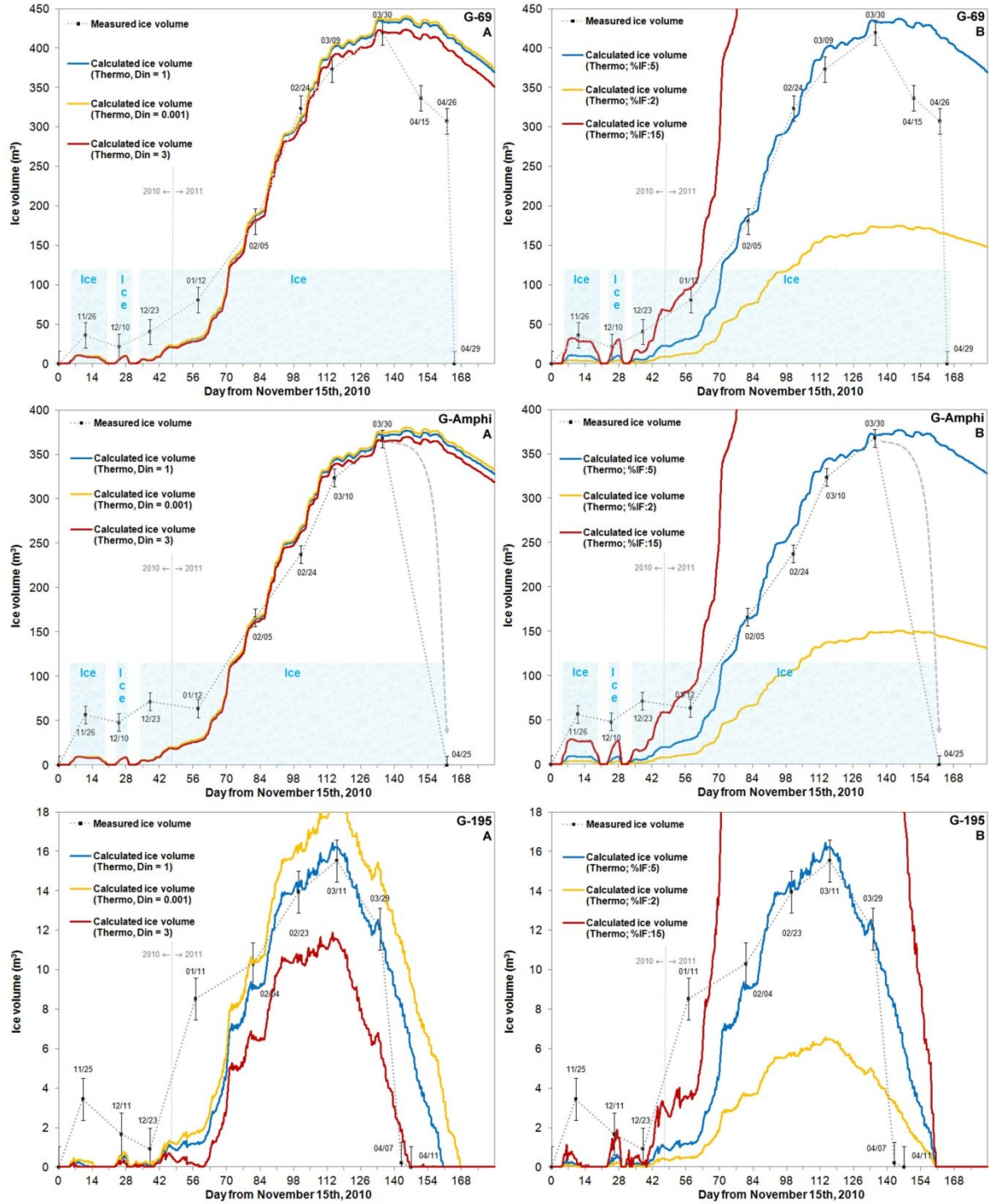
**Figure 4.11.** Calculated and measured ice volume evolution at the three study sites (G-69, G-Amphi and G-195). A) for different value of incoming water flow ($D_{in}$): $D_{in} = 1$ L/s; $D_{in} = 0.001$ L/s; $D_{in} = 3$ L/s; and B) for different percentage of ice withheld onto the rockwall (%IF): %IF:5 = 0.05 (5%); %IF:2 = 0.02 (2%); %IF:15 = 0.15 (15%).

## 6.2. MODEL COMPARISON

The measured and simulated ice walls volume changes are presented and compared in figure 4.9. The two simplified models (FDH and FDH+Qrad) were also tested to follow the ice cascade (G-Voile) growth and decay general evolution presented in chapter 3 (Annexe A, Fig. A.1). For the north-facing ice walls (G-69 and G-Amphi), the FDH model performed as well as the Thermo model. The calculated ice volume evolution curves are similar and the simulation results show comparable $R^2$. The efficiency of the FDH model is easily explained by the primary role played by the sensible heat flux ($Q_{cv}$) in the freezing and melting process of the north-facing ice wall. The FDH model even produces a better simulation of the rapid ice volume accumulation during the fast growing period that occurs near the end of December (day 40). The growth depletion that occurs around the beginning of March (day 105) is also well reproduced by this simple model. But for the same reason as for the Thermo model, the FDH model is incapable of simulating the sudden collapse of the north-facing ice walls. Moreover, the FDH model encounters difficulties when reproducing the south-facing ice wall evolution (Fig. 4.9, G-195). During the early stages of formation, observations show that ice forms and melts multiple times. Instead of a chaotic growth and melt behavior with daily fluctuation as the observations and the Thermo model suggest, the FDH model shows a constant evolution in the formation of ice. Even if the fast growing evolution occurring after December 23$^{rd}$ (day 38) is well reproduced by the FDH model, we were not able to simulate the fast melting of the exposed ice wall. The FDH model is also inefficient to simulate the ice cascade (G-Voile) growth and decay general evolution (Fig. A.1). Adding the radiative heat budget to the FDH model considerably improved the simulated ice volume path of the south-facing ice wall (G-195). The results are somewhat meaningful: better fit and higher $R^2$ value. The first ice growing stage is even better simulated than by the Thermo model. The FDH+Qrad model is also efficient to simulate the fast melting of the G-195 ice wall. This simple model also shows the best $R^2$ for the north-facing ice walls (G-69 and G-Amphi). Although it cannot exactly simulate the sudden collapse of the G-69 and G-Amphi ice walls, it showed a steeper melting tendency during the last melting period. Unfortunately, the FDH+Qrad model remains unable to reproduce adequately the growth and decay of the ice cascade G-Voile (Fig. A.1), even if it was demonstrated that the melting and the breakup of the ice cascade

108

is closely related to solar radiation exposure (chapter 3). This confirms the prominent role of an increase of the discharge on the melting of frozen waterfalls.

Unlike the development of a complex thermodynamics model which requires a complete meteorological setup, the development of the simplified model only requires a few air temperature sensors and pyranometers: an important aspect in the prospective development of an ice wall collapse predictive model. Furthermore, in the development of the Thermo model we assumed that wind speed, relative humidity and air pressure measurements were representative of the whole region conditions. It may be true for the air pressure which doesn't vary very much over the studied area, but the relative humidity may be quite different between the coast and 23 km inside the valley. These aspects are especially important for determining the wind speed to use in the calculation of the heat transfer coefficient ($h_{wa}$). The Thermo model would certainly return better results if each studied site had been equipped with its own anemometer. The sensible and latent heat flux calculation are closely related to the heat transfer coefficient, which in turn depends on a proper evaluation of the wind speed profile over the ice surface. Further studies should consider this aspect and concentrate in a better evaluation of the heat transfer coefficient over such vertical ice formations.

## 7. CONCLUSIONS

The meteorological data acquired in the vicinity of the ice walls greatly improved our comprehension of ice walls growth and decay dynamics. Even if it was not possible to observe any clear relationship between precipitation, relative humidity, solar radiation or wind speed and ice volume changes in the ice walls, several observations emerged: the liquid precipitation may increase the melting rate of the ice wall, a little layer of crusty ice forms after snow accumulation over some narrow ice ledges, low relative humidity must favour evaporation and heat release from the water-ice system to the atmosphere, direct solar radiation drastically increase the ice melting rate and high wind speed certainly favours the exchanges of sensible heat with the atmosphere. However, the air temperature and the cumulative effect of negative air temperatures (expressed as the "freezing degree-hours") clearly show the best relationship with the ice volume evolution. As the temperature drops and stays under 0°C, a fast ice growing period is observed. When the ice

walls are well formed, less water is available for freezing over the ice structures and the freezing rate decreases. The increasing air temperature brings heat to the ice covers which eventually collapse before the end of the melting process. Moreover, rapid air cooling (several $^{\mathrm{o}}C\cdot h^{-1}$ over several hours) and low temperatures ($<-10^{\mathrm{o}}C$) generated tensile stress that can trigger mechanical collapse of unstable ice structures (Gauthier & al. 2012; Montagnat & al. 2010; Weiss & al. 2011). Cracks were observed on the G-Amphi ice wall after a series of daily temperature change around $0^{\mathrm{o}}C$ but this was not sufficient to provoke its collapse. Strong ice anchors maintain the ice wall firmly attached to the rockwall. Heat must melt many of these anchors before the heavy ice wall collapse under its own weight. Furthermore, the relatively low angle slope ($60^{\mathrm{o}}$ to $65^{\mathrm{o}}$) rockwall on which G-Amphi ice wall formed may have favoured its stability.

The development of a thermodynamic model (Thermo) confirmed many of these assumptions. Firstly, the convective heat flux ($Q_{cv}$) proved to be the main factor responsible for the ice growth. The radiative heat budget ($Q_{rad}$) also plays a major role in the ice growing process, especially for the south-facing ice wall (G-195). Even during cold periods, the ice melts during sunny days whereas ice formation mainly occurs at night when heat is released through emissions of radiation from the ice surface towards the atmosphere. Under relatively low humidity, the latent heat of evaporation ($Q_{evap}$) tends to evacuate heat from the icy system, but it remains a second order heat flux. At any time during the growing or melting process, the conductive heat flux ($Q_{cc}$) and the sensible heat flux carried by the flowing water ($Q_{w}$) remains almost negligible, mainly because of the limited discharge of the underground water ($D_{in}$). However, these heat fluxes possibly accelerate the melting of ice anchors at the ice-rock interface and eventually favour the collapse of the ice walls. The melting of the north-facing ice wall mainly results from convective heat transfer ($Q_{cv}$) and solar radiation (G). For the south-facing ice wall, the incoming direct solar radiation (G) is the primary source of heat. Finally, no major difference in terms of ice volume changes, collapsing process or heat transfer was noticed between the two north-facing ice walls even if G-Amphi was forming on a lower angle rockwall than G-69.

The simplified temperature index model (FDH) was efficient for reproducing volume changes of north-facing ice walls. However, it proved inappropriate to simulate the daily

variation of the sun-exposed ice wall and the rapid melt induced by direct solar radiation. Adding the radiative heat budget ($Q_{rad}$) to the FDH model greatly improves its performance for both ice wall situations (north and south-facing). The FDH+Qrad model efficiency demonstrates the major contribution of radiation heat fluxes during the freezing and the melting process of the exposed ice wall. Unfortunately, the models remain inappropriate to simulate the collapse phase of the ice walls. However, a better understanding of the thermodynamic of these superficial ice formations would greatly facilitate the development of ice wall collapse forecasting models, an essential step in efficiently managing the risks of falling ice blocks on adjacent roads.

# CHAPITRE 5: FORECASTING METHOD OF ICE BLOCKS FALL BY LOGISTIC MODEL AND MELTING DEGREE-DAYS CALCULATION: A CASE STUDY IN NORTHERN GASPÉSIE, QUÉBEC, CANADA.

Francis Gauthier, Bernard Hétu and Michel Allard

**Résumé :** La chute de blocs de glace est un risque naturel fréquent dans les régions montagneuses au climat froid. Les blocs de glace proviennent de l'effondrement des glaces de paroi. Les données météorologiques d'Environnement on été analysées pour 440 cas de chutes de blocs de glace rapportés par le Ministère des transports du Québec (M.T.Q.). Les variables météorologiques ont été utilisés pour développer un modèle logistique de prévision des chutes de blocs de glace. Les analyses montrent que la chute des blocs de glace est principalement contrôlée par une augmentation de la température de l'air au-dessus du point de fusion de la glace. Le calcul des degrés-jours de fonte (DJ) peut être utilisé pour suivre les variations de la température et le transfert de chaleur dans les masses de glace. De grandes variations de la température de l'air, mais plus particulièrement une chute drastique en dessous de 0°C ou un cycle de gel et de dégel, peuvent induire des stress thermomécaniques suffisants pour favoriser l'ouverture de fissures et provoquer l'effondrement de structures de glace instables (formations de glace suspendues). En suivant l'évolution des DJ et le meilleur modèle logistique, il est possible de cibler les périodes les plus à risque et prévoir l'effondrement de certaines glaces de paroi.

**Abstract:** Ice blocks fall is a serious natural hazard that frequently happens in mountainous cold region. The ice blocks result from the melting and collapse of rockwall icings (ice walls or frozen waterfalls). Environment Canada weather data were analysed for 440 cases of ice blocks fall events reported in northern Gaspésie by the "Ministère des Transports du Québec (M.T.Q.). The available meteorological variables were used to develop a predictive ice blocks fall model. The analysis shows that the ice blocks fall are mainly controlled by an increase of the air temperature above the melting point of ice. The melting degree-days (DDmelt) can be used to follow the temperature variations and the heat transfer into the ice bodies. Furthermore, large daily temperature changes, especially drastic drops of temperatures below 0°C and freeze-thaw cycles can induce enough mechanical stress to favour the opening of cracks and possibly cause the collapse of unstable ice structures such as freestanding ice formations. By following the evolution of the DDmelt and the best logistic model, it is possible to forecast the collapse of some of the most problematic rockwall icings and target the most hazardous periods along the northern Gaspésie roads.

# 1. INTRODUCTION

In northern Gaspésie (Eastern Canada), the coastal road is flanked by relatively high cliffs. On those rockwalls, many waterfalls and resurgences (seepage) lead to the formation of rockwall icings during winter. The ice formations can be called ice walls when they form from an underground or subsurface resurgence, and ice cascades or frozen waterfalls when the water comes from a permanent surface runoff (Bianchi 2004; Gauthier 2008; Gauthier & al. 2012; Gauthier & al. 2013). Each spring, a series of ice block falls is reported by the "Ministère des Transports du Québec" (M.T.Q.) (Gauthier 2008; Gauthier & al. 2012; Girard & Hétu 1994; Hétu & al. 1994). In 2010, on April 22$^{nd}$ and 24$^{th}$, the collapse of the "Échappé belle" ice wall (Fig. 5.1B) was filmed (videos 5.1 and 5.2)[2]. Before the first event, the ice wall was 40 m high, 30 m wide and about 3 m thick at its base. Each collapse released nearly a ton of ice blocks rolling, jumping and sliding down a steep slope (35$^{o}$). During the first event, many ice blocks were stopped by the protection berm (Vid. 5.1). The remaining ice blocks ended up on the road. They were removed by the authorities immediately after the event. Two days later, at 15:11, the second half of the ice wall collapsed suddenly as a car was passing on the road below (Vid. 5.2). Fortunately, a massive 10 m$^3$ rolling ice block jumped over the ice and snow filled roadside berm, hit the electrical line and the road at a speed of about 70 km·h$^{-1}$ immediately after the passage of a vehicle. Some of the ice blocks finished their run 30 to 40 m away in the sea. Some protective infrastructures were built since. But the authorities are still in need of a set of effective predictive tools to better manage this kind of natural hazard.

We know that air temperature is the main variable controlling the growth and decay of ice walls and ice cascades (Gauthier 2008; Gauthier & al. 2012; Montagnat & al. 2010). Montagnat & al. (2010), showed that it is possible to quantify the ice cascades growth evolution with a simple conductive heat flux model through the ice cover. But the model was not effective to predict the collapse of the ice structures. Gauthier & al. (2012) showed that it is possible to statistically predict the ice block falls in spring by calculating the sum of positive mean air temperature starting March 1$^{st}$ and expressed as the positive degree-days (DDp). But in the last two years, winter events were also reported and the DDp model

---

[2]Electronic supplementary material (videos): 29924vid5-1.avi and 29924vid5-2.avi

cannot predict these events. Furthermore, Weiss & al. (2011) and Gauthier & al. (2012) showed that a rapid decrease of air temperature (several $^{o}C \cdot h^{-1}$) and low air temperature (<-10$^{o}$C) could induce enough mechanical stress to provoke the formation of cracks sometimes resulting in the collapse of freestanding ice structures. Meteorological variables representing this behavior should be included in the development of ice block falls predictive model.

In this paper, we present a twelve-year analysis based on the M.T.Q.'s ice blocks falls database and weather data from Environment Canada. New variables were developed and improved statistical models are proposed for a better risk management of ice falls along the northern Gaspésie road.



**Figure 5.1.** Road 132 west of the Mont-Saint-Pierre village, the Gaspesian plateau escarpment and a series of ice walls: Deux phoques en Askalade (A), Échappé belle (B), Petit cirque (C), l'Aigle noir (D), Blue Stratos (E) and Corneille (F).

## 2. STUDY AREA

The study area is a road corridor of over 80 km long between Sainte-Anne-des-Monts and Manche d'Épée (Fig. 5.2). Road 132 runs along the shore of the Saint-Lawrence estuary at the foot of the cliffs and steep slopes of the Gaspesian plateau (Hétu & Gray 1985). Rockwall icings formed on the many natural escarpments and manmade blasted cliffs located along the road. These cliffs are all facing north, north-east or north-west. A six-kilometer road section (road 198) south of l'Anse-Pleureuse is also part of the study area. Two rockwall icings formed on a south-west oriented escarpment. A total of 60 rockwall icings were located along these roads (Fig. 5.2). Out of this number, 22 are considered as hazardous by the M.T.Q..

The escarpments are mainly composed of bedded and highly fractured shale, sandstone and silty limestone: a geological setting favouring water infiltration and underground percolation (e.g. Brisebois & Nadeau 2003; Gautschi 2001; Walkinshaw & Santi 1996). Out of the 22 highly hazardous ice formations, six are frozen waterfalls (ice cascades # 2, 3, 10, 15, 18 and 22). The others formed after the freezing of underground or subsurface resurgence water over the cliff faces.

The region is characterized by a cold and maritime climate. The mean annual temperature is $3.3^{o}$C with an average minimum temperature in January of $-13.7$ °C (Gagnon 1970; Environment Canada 1971-2000). The maritime influence of the Gulf of St. Lawrence provides an average rainfall of about 1000 mm spread evenly throughout the year. One third of this precipitation falls as snow from mid-November to late April. The liquid precipitation in fall is also relatively high with about 200 mm for October and November. Generally, the first frost occurs in October, but ice begins to forms more convincingly on rockwalls around mid-November.
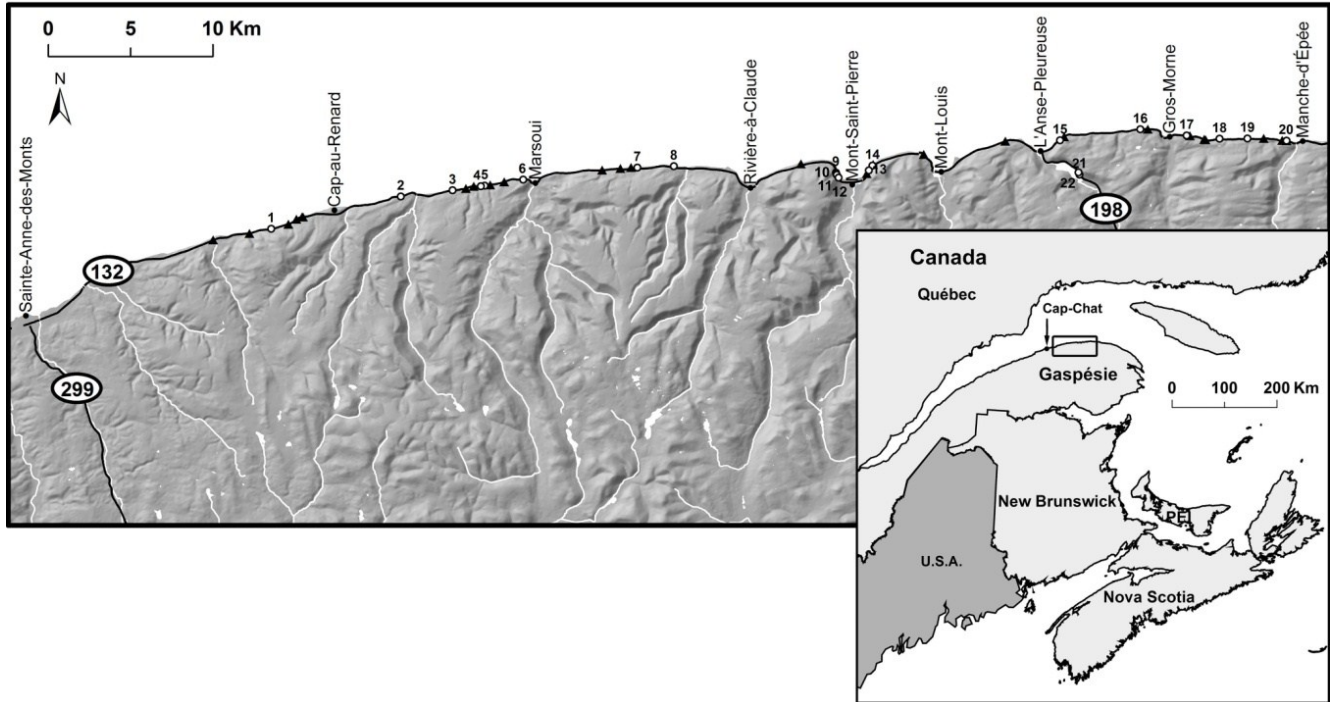
**Figure 5.2.** Location of 60 rockwall icings along the road 132 and 198 in Northern Gaspesie (Quebec, Canada): 38 potentially hazardous (black triangle) and 22 identified as risk threatening by the M.T.Q. (numbered white dot).

## 3. METHODOLOGY

### 3.1. THE ICE BLOCKS FALL DATABASE

The database on ice blocks fall events is part of M.T.Q.'s larger slope movement database (Service Centre of Sainte-Anne-des-Monts). Since 2000, every ice block removal intervention has been registered. For each event, the date and the type of intervention is noted. A manual intervention is reported when the ice blocks are small enough to be removed by hand. If mechanical equipment such as loaders is required, a mechanical intervention will be reported instead. For the study, we analyzed all the data from 2000 to 2012 excluding 2001. The data is missing for this specific year and it appears no one is able to tell what has happened with that year's archives.

### 3.2. METEOROLOGICAL DATA

The meteorological data comes from an Environment Canada weather station located in Cap-Chat (Fig. 5.2) (Environment Canada 2000-2012). The daily precipitation in water

equivalent (Ptot) and the daily mean (Tmean), maximum (Tmax) and minimum (Tmin) temperatures are the only weather data available for this station.

Many meaningful variables were calculated from these data. The daily liquid precipitation (P1) was extracted from Ptot when Tmean was higher to the freezing point of water (Tf = $0^{o}C$). According to Gadd (2006) and Gauthier & al. (2012), the liquid precipitation is a major variable because it accelerates the melting of rockwall icing formations. We also calculated a two (P2) and three-days (P3) antecedent liquid precipitation sum.

Gauthier & al. (2012) showed that important daily air temperature changes, but especially a drastic temperature decrease (Weiss & al. 2011) could induce mechanical stress enough to favour crack opening. For example, on March 28th 2008, Gauthier & al. (2012) described the opening of a large fracture at the base of a 75 m high ice column after a temperature cooling of $14^{o}C$ (from $-1^{o}C$ to $-15^{o}C$ in less than 24 hours). Sometimes these cracks result in the destabilisation and collapse of certain types of ice formations such a freestanding ice structures (suspended or columnar ice formation). During the night of January 20th and 21st 2008, Weiss & al. (2011) reported the collapse of an entire ice structure after air cooling of $15^{o}C$ (from $+6^{o}C$ to $-9^{o}C$). To represent these phenomena, three different variables are proposed. The daily temperature range (Dtr) is the difference between Tmax and Tmin. The cooling or freezing intensity (Fi) is also the difference between Tmax (or $0^{o}C$ if Tmax is positive) and Tmin, otherwise Fi equal 0. A daily freeze-thaw cycle (Ft = 1) occurs when Tmax is higher than $0^{o}C$ and Tmin is lower than $0^{o}C$. Otherwise, Ft is zero.

Gauthier & al. (2012) also showed that it is possible to follow the ice blocks falls frequency by calculating the positive degree-days (DDp): the sum of the positive value of Tmean starting from March 1st. This variable is regularly used as a simplistic representation of heat transfers in ice bodies (e.g. Ambach 1988; Braithwaite 1981; Braithwaite 1995; Hock 1999; Hock 2003; Shen & Yapa 1985; Singh & al. 2000). Because ice blocks falls were reported during winter after an extended thaw period, we proposed the use of a melting degree-days variable (DDmelt) instead. DDmelt can be expressed as the sum of Tmean (positive and negative) with a minimum value of zero starting at the first complete frost day (Tmax < $0^{o}C$). Compared to the DDp, the DDmelt can be used as a predictive variable during the whole cold season. Furthermore, it also takes into account the refreezing periods. During

such periods, rockwall icing formations can reform or reconsolidate resulting in a "re-stabilisation" of the ice structure. Finally, two dependant variables of the DDp and the DDmelt are needed: the squared DDp (DDp2) and the square DDmelt (DDmelt2). Their function is to make the logistic model result (ice blocks fall probability) decrease when it reaches the maximum probability of occurrence.

## 3.3. DATA ANALYSIS

At first, frequency histograms (interannual and julian-days) were produced and analyzed. The daily frequency is also compared to the Environment Canada weather data (Tmean, Tmax, Tmin, daily snow and rain, DDmelt). The spring, winter and fall weather conditions before and after significant ice blocks fall event periods are analyzed. According to (Gauthier & al. 2012), the degree-days (DDp or DDmelt) represent well the temperature rise and evolution and the heat transfer (e.g. Braithwaite 1995; Hock 2003; Montagnat & al. 2010) into ice masses. We use the DDmelt to develop a five degree Celsius cumulative degree-days frequency histogram for all the M.T.Q. interventions. Finally, the amounts of DDmelt accumulated before the collapse of eight specific rockwall icings were compiled.

To avoid using the year as a parameter in the development of the model, an explanatory variable representing each winter season rockwall icing growth potential is needed. A growth index (Ig) was calculated for each year's rockwall icing growth season. We first assume that a larger ice wall may result in more ice blocks falls on the road, especially during the melting season. We assume that two main conditions are required to support the growth of larger rockwall icings: persistent water flow and cold temperature. The accumulation of a thick snow cover at the beginning of the ice growth season can inhibit the freezing front in the ground (Bayard & al. 2005; Sutinen & al. 2008; Zhang & al. 2008). If this situation concurs with a cold winter, persistent water supply on the cliff will freeze and favour larger ice formations. To test these assumptions, we correlate the mean winter air temperature ($T_{mwa}$ = average temperature of December, January and February) and the total solid fall and early winter precipitation ($P_{sf}$ = snow accumulation of November and December) with the number of each year interventions. At the end, the Ig can be stated as:

$$Ig = P_{sf} \cdot T_{mwa}{}^2 \tag{5.1}$$

The Ig can be normalized by dividing each year's value by the mean Ig value. Finally, the Pearson coefficient correlation was calculated for each relation.

## 3.4. LOGISTIC MODEL

The meteorological variables effect on the ice blocks fall occurrences (Icefall = 1) or non-occurrences (Icefall = 0) was simulated with logistic regression (LR). This statistical tool is often used to predict event occurrences or non-occurrences from a series of explanatory variables. It has already been used as a tool in risk management to predict ice blocks fall (Gauthier & al. 2012), snow avalanches (e.g. Ancey 2006; Hebertson & Jenkins 2003; Jomelli & al. 2007) or debris-flow (e.g. Jomelli & al. 2003; Jomelli & al. 2004; Sepúlveda & Padilla 2008; Xu & al. 2012). Because the dependent variable (Icefall) is dichotomous, we used the binary LR model (Hosmer & Lemeshow 2000):

$$P = \frac{1}{1+e^{-(\beta_0+\beta_1 x_1+\cdots+\beta_i x_i)}} \tag{5.2}$$

where P is the probability of ice block fall occurrence, $\beta_0$ is the constant in the equation (intercept), $\beta_1$, $\beta_2$, ...$\beta_i$ are the coefficient calculated for the independent variables $x_1$, $x_2$, ...$x_i$. Before developing the LR models, a matrix of Pearson correlations was generated to evaluate the level of correlation between the different variables. The analyses were performed with the SPSS 20.0 software. The model fitting was done using the maximum likelihood method (McCullagh & Nelder 1989). To evaluate the validity of the LR models and variables, different statistical significance tests were performed. The standard error, the level of significance (p-value) and the Wald z-statistic were calculated for each variable. We use the Akaike Information Criterion (AIC) and the Nagelkerke R-square ($R^2$) to compare and evaluate the validity of adjustments to the tested models. The AIC provides information on the degree of approximation of the model (minimum loss of information) while penalizing the addition of variables that may be redundant (Burnham & Anderson 2002; McCullagh & Nelder 1989; Meylan & al. 2008). Finally, the delta AIC and Akaike weights are complementary tools for comparing models. The delta AIC is the difference between the AIC model and the AIC best model, while the Akaike weight (Aw) informs us about the probability that the tested model is the best given to the data and the other models (Burnham & Anderson 2002; Mazerolle 2004).

The first objective was to develop and compare these two simple models: the DDp+DDp2 model developed by Gauthier & al. (2012) and the new DDmelt+DDmelt2 model proposed in this paper. Because the P1, P2 and P3 variables are highly correlated together, the next strategy was to compare the significance of the variables used with the DDmelt and evaluate the more significant liquid precipitation variable. Then, each explanatory variable was analyzed independently to verify their individual effect on ice blocks fall occurrences. In the end, the goal was to determine the best and simplest predictive model. We opted for a backward step-wise analysis starting with the more complex model and ending with the best model. At each step, the less significant variable (highest p-value and closest to zero Wald z-statistic) was eliminated. The best model should show no insignificant variable (p-value over 5%), the lowest AIC, the highest Aw and the highest $R^2$.

## 4. RESULTS AND DISCUSSION

### 4.1. ICE BLOCKS FALL FREQUENCY

The M.T.Q. proceeds annually to an average of 37 interventions to remove ice blocks from the road (Fig. 5.3A). The number of ice blocks falls on the road vary from 23 events in 2003 and 2007 to 66 events in 2005. Prima facie, the proportion of mechanical interventions compared to the number of manual interventions seems to decrease in the last years. This observation is consistent with the increased frequency of maintenance and clearing of ditches and security berms.

As described by Gauthier & al. (2012), rockwall icings collapse is mainly a spring event (Fig. 5.3B). The events along road 198 occur over a short period in early spring. Most ice blocks fall events reported in fall occurred on this road section. The two rockwall icings present along this road section are exposed to the afternoon sun radiation. In 2008, the first winter event was registered in the M.T.Q. database. Since, some ice blocks falls were observed by Gauthier & al. (2012) and reported by many M.T.Q. patrollers (personal communications). However, it seems that most of these ice blocks falls didn't reach the road as they were stopped by the snow cover.
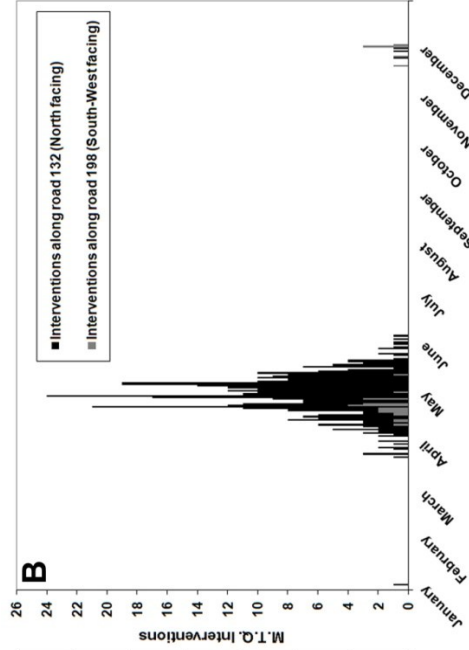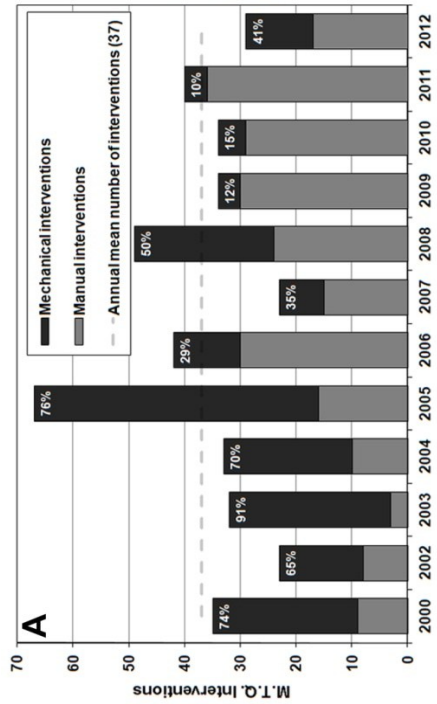
**Figure 5.3** Ice blocks fall annual frequency (A) and ice blocks fall time-frequency (recorded in iulian-days) (B).
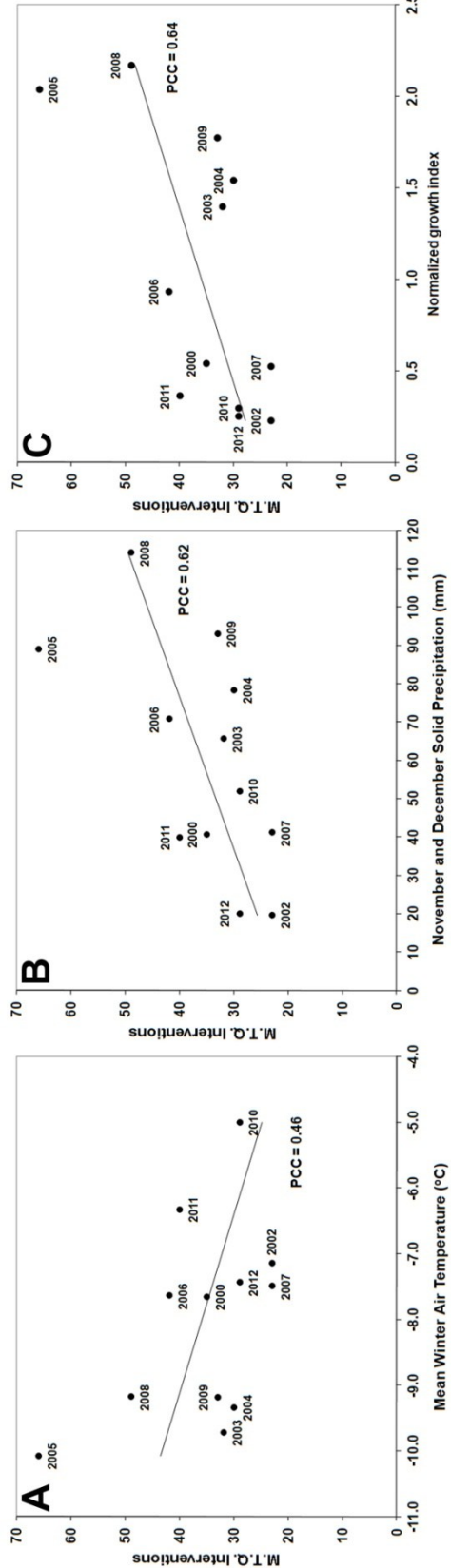


**Figure 5.4.** Correlation between the mean winter air temperature (A), the November and December solid precipitation (B), the normalised index growth (C) and the number of M.T.Q. interventions (PCC = Pearson Correlation Coefficient).

## 4.2. DATA ANALYSIS

A weak correlation between the mean winter air temperature and the number of M.T.Q. interventions was established (Fig. 5.4A). The number of reported ice blocks falls on the road tends to be slightly higher after a cold winter. A stronger correlation was established between the number of interventions and the late fall and early winter's solid precipitations (Fig. 5.4B). More interventions are reported in spring when heavy snow accumulation occurs at the beginning of the rockwall icings growing season. Finally, the Ig shows the best level of correlation with the number of interventions (Fig. 5.4C). With this acceptable level of correlation, it is preferable to use the Ig has a variable representing each year's growth potential instead of the year's digits.

Between the 2$^{nd}$ and 4$^{th}$ of December 2010, five ice blocks falls were reported by the M.T.Q. (Fig. 5.5A). During the last two weeks of November, ice formed over many rockwalls. Except for three days (November 24$^{th}$, 25$^{th}$ and 29$^{th}$), the mean air temperature stayed below 0$^{o}$C for 12 consecutive days. The first event comes after a significant temperature increase to 9.8$^{o}$C (Tmax) and an accumulation of 8.3 DDmelt. The following events, reported down the south-west facing rockwall along road 198 (rockwall icings # 21 and 22), occurred after 10.3 and 13.6 DDmelt accumulations and coincides with 18 and 22 mm rain events (Fig. 5.2 and 5.5A).

The ice block fall reported on January 4$^{th}$ 2008 is not the result of a temperature increase above the melting point or of a melting accelerated by heavy rain (Fig. 5.5B). It comes after a drastic temperature decrease of 14$^{o}$C (Dtr) from -7.1$^{o}$C to -21.1$^{o}$C. It is the only ice block fall event reported during a cooling or freezing intensity (Fi) time period higher than 10$^{o}$C and only two other events were reported with Fi higher than 5$^{o}$C. As mentioned previously, many other ice blocks falls were reported but none of them reached the road, the snow covering the slope stopping their run. For example, at the end of February 2010, the Tmax stayed below zero for 12 consecutive days and then reached a peak of 5.1$^{o}$C on February 23$^{rd}$ (Fig. 5.6A). During this period, 44 mm of rain and sleet fell on the north shore of the Gaspe Peninsula. Moreover, eight consecutive daily Ft cycles (February 19 to 26$^{th}$) and two consecutive Dtr of 8.1 and 8.7$^{o}$C were recorded (February 24 to 25$^{th}$). Many ice blocks were found down the ice carapaces. Fractures were observed on certain ice walls (Fig.

5.6B) and many ice cascades melted and collapsed after the noticeable increase of the water flow (Fig. 5.6C).

Apparently, the spring events begin when the air temperature rises above the melting point of ice (Fig. 5.7). At the beginning of the melting season, some events concur with high Dtr values and during Ft cycles. On the 629 days with a Dtr higher than $10^{o}$C and 710 freeze-thaw cycles (Ft) recorded at the weather station, 101 and 134 ice block fall events have been reported respectively. For instance, two ice blocks falls were reported on April $16^{th}$ 2011 after a temperature decrease of $9.7^{o}$C below zero, a Dtr of $11.4^{o}$C and a Ft cycle. However, more events, such as those that occurred on April 28, 29 and $30^{th}$ 2008 or April $23^{rd}$ and $25^{th}$ 2011, occur during warm days with Tmax exceeding $10^{o}$C and with Tmin above $0^{o}$C (Fig. 5.7). Other ice blocks removal interventions take place at the occasion of heavy rain events such as the three events reported on April $24^{th}$ 2008 after two consecutive rainy days of 9 and 7 mm respectively (Fig. 5.7A). As the temperatures continue to rise, more events are reported, but the mean daily air temperature (Tmean) variation can hardly be correlated with the ice blocks fall events. The DDmelt is more effective to follow the Tmean evolution and the M.T.Q. interventions frequency.

As previously suggested by Gauthier & al. (2012), the DDp, or the DDmelt in our case, can be used as the main variable to describe the ice blocks fall frequency (Fig. 5.8) and the rockwall icing collapsing periods (Tab. 5.1). In Table 5.1 we present the amount of DDmelt accumulated before the collapse of eight different problematic rockwall icings present in the study area. As the air temperature rise and the DDmelt accumulate, the number of reported ice blocks fall events grow (Fig. 5.8). The proportion of manual interventions is higher during this period. During this early stage of melting, water stream discharges increase which tends to accelerate the melting process of the ice cascades (Gauthier 2008; Gauthier & al. 2012). They then generally collapse in little ice block pieces resulting in events of smaller magnitude. Furthermore, the mean amount of DDmelt accumulated before the collapse of frozen waterfalls is considerably lower than for the collapse of ice walls (ice cascade # 2, 10 and 22, Table 5.1). Their decay and collapse is faster. Conversely, the ice walls also melt, but they remain attached to the rockwalls for longer periods. Only the most unstable structures (freestanding ice columns, ice stalactites and

other partially adherent ice structure) collapse, resulting in smaller ice blocks fall events at the beginning of the melting season. After an accumulation of 40 to 90 DDmelt the ice blocks fall frequency reaches a peak. The number of mechanical interventions is higher. As shown in the videos 5.1 and 5.2, complete ice wall formations collapse results in many events of greater magnitude. The mean amount of DDmelt needed before the collapse of ice walls is higher (ice walls # 1, 8, 12, 20 and 21, Table 5.1). After, this period of intense activity, the last pieces of ice still attached to the rockwalls melt and fall resulting in minor ice blocks fall events. This tendency can easily be modeled by logistic regression.
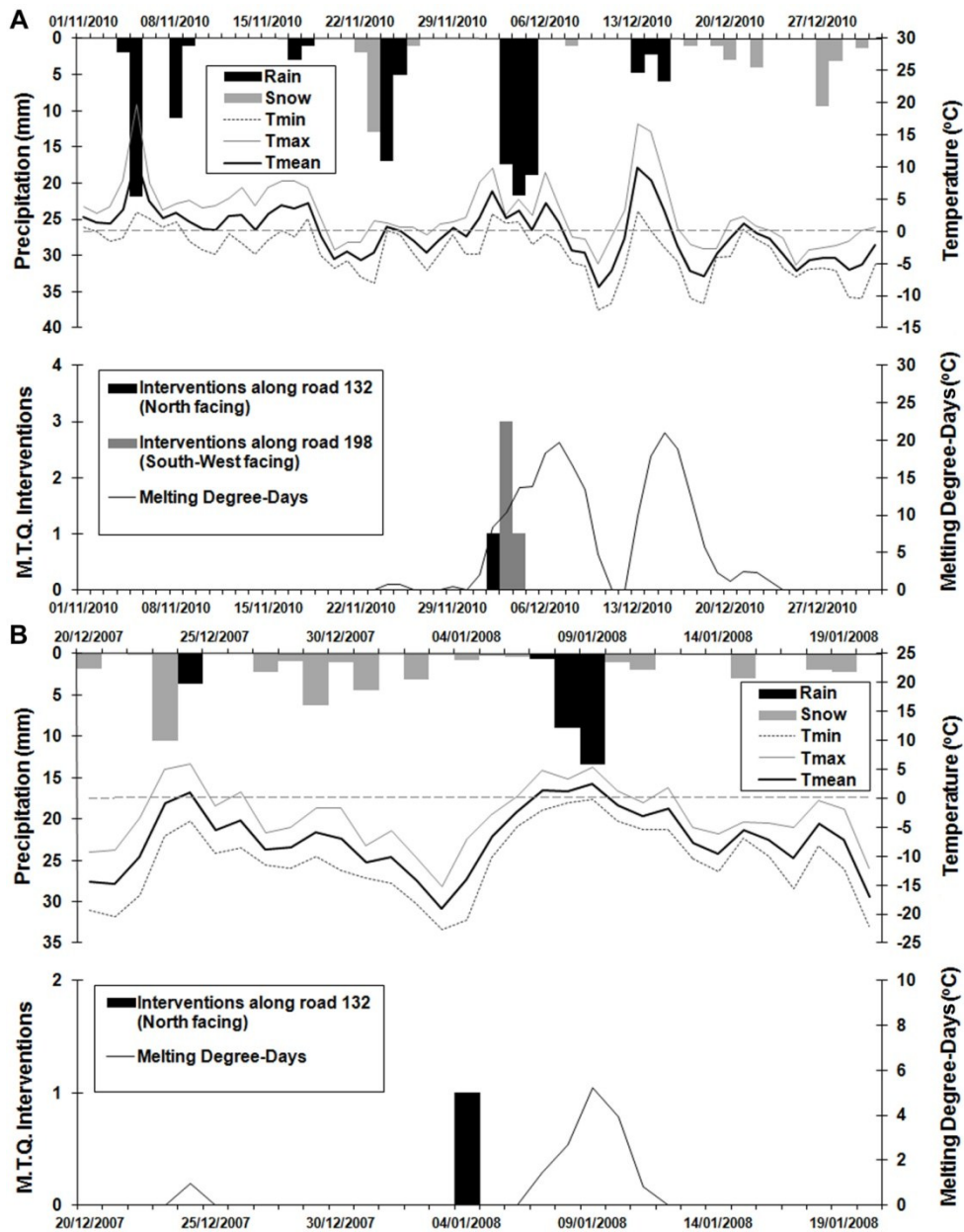
**Figure 5.5.** Evolution of weather conditions and M.T.Q. interventions between (A) November 1st to December 31st 2010 and (B) December 20th 2007 to January 20th 2008.
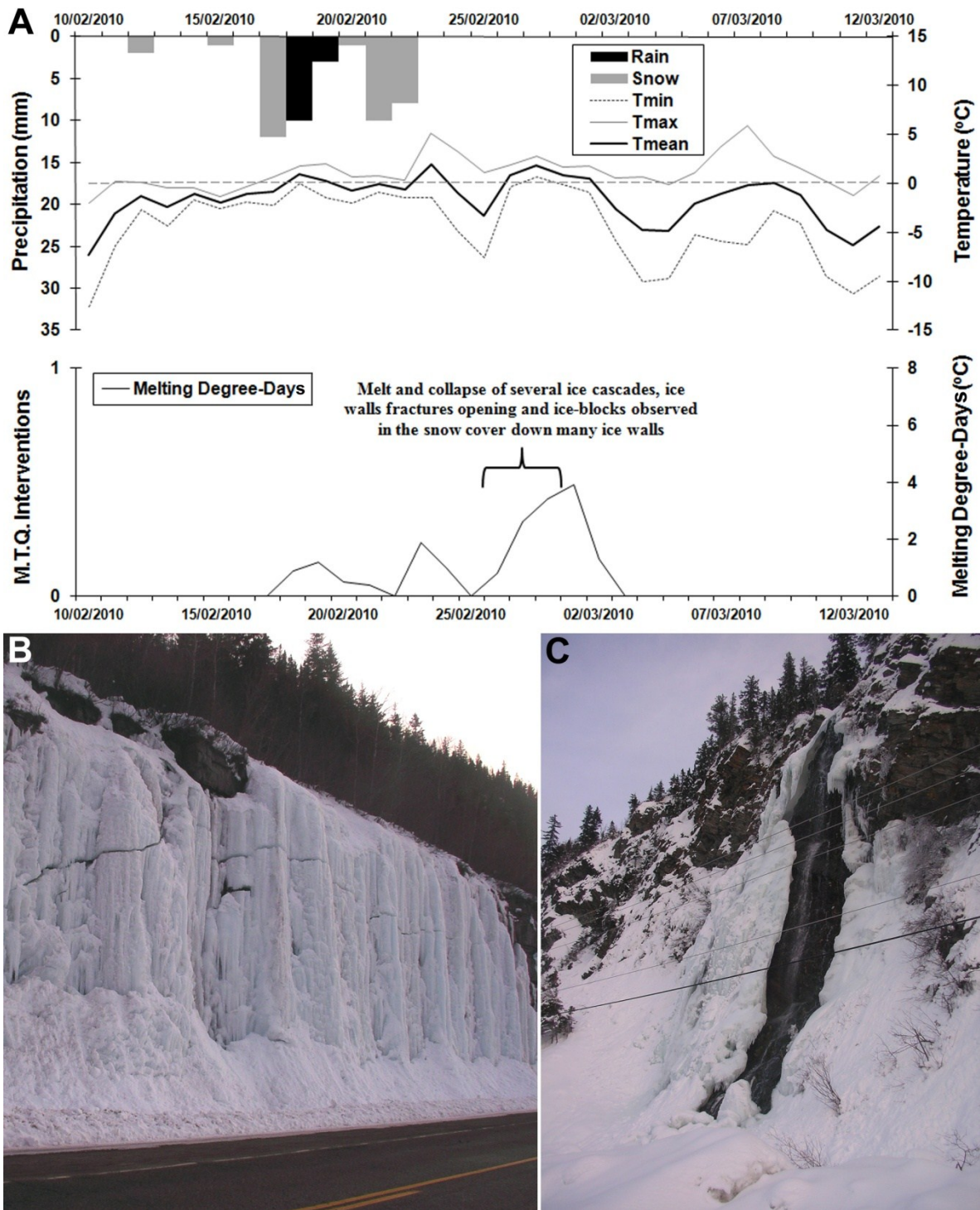
**Figure 5.6.** Weather condition evolution between February 10th and March 13th 2010 (A), fractures opening over an ice wall (ice wall #7, March 28th 2010) (B), melt and collapse of the Voile de la mariée (ice cascade #2, March 28th 2010) (C).
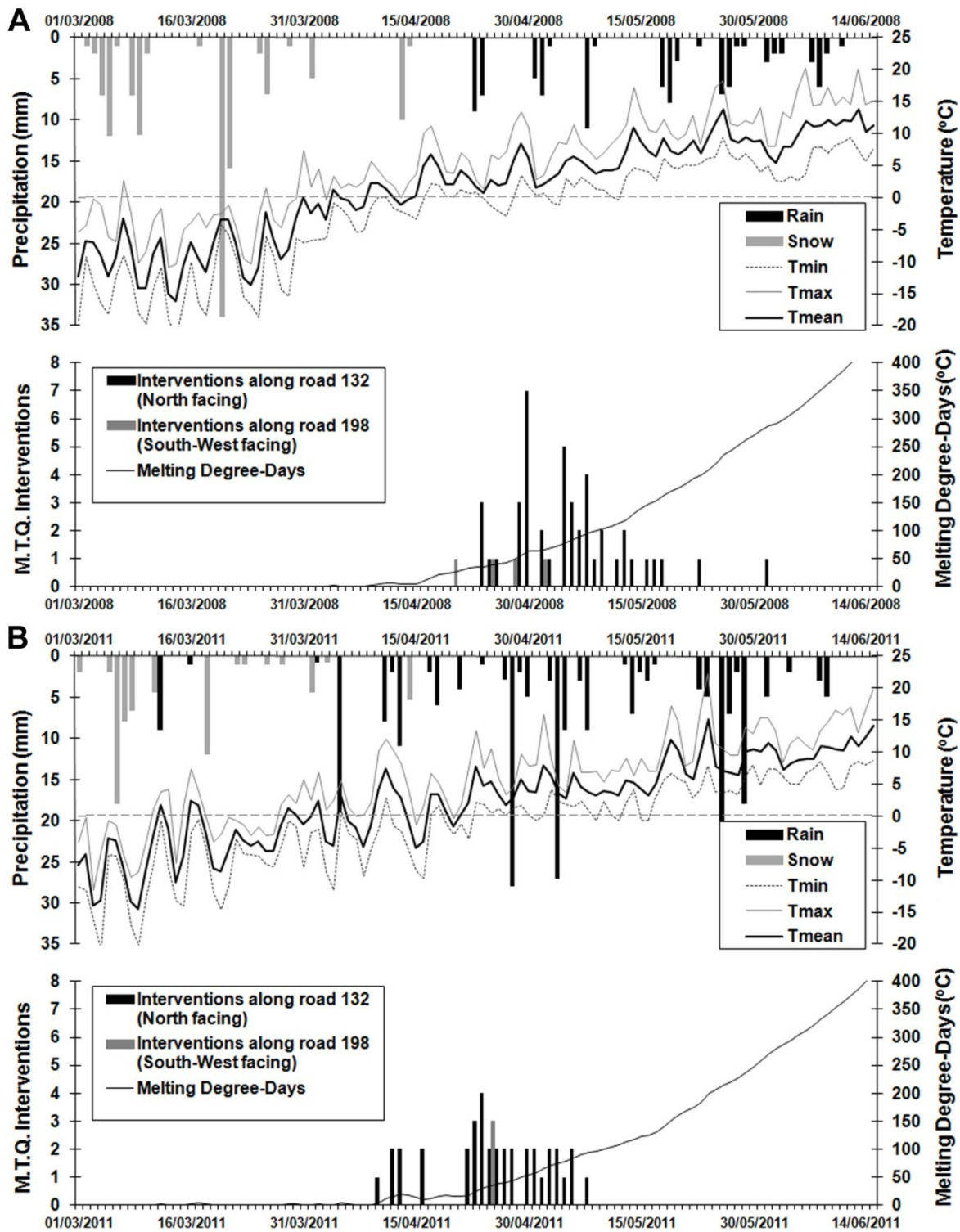
**Figure 5.7.** Weather condition evolution between March 1st and June 15th and the M.T.Q. interventions in 2008 (A) and 2011 (B).
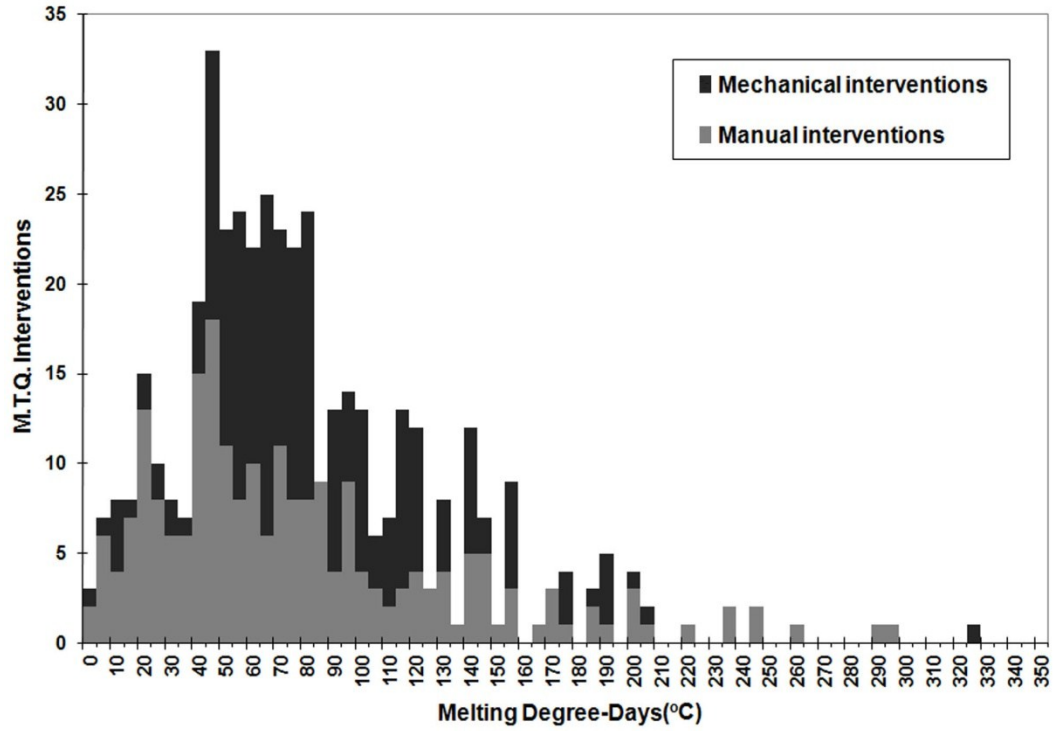
**Figure 5.8.** Ice blocks fall frequency in melting degree-days (DDmelt).

**Table 5.1.** Melting degree-days (DDmelt) before the collapse of specific rockwall icings.

| # | Rockwall icings | Hydrology | Orientation (exposure) | Date[1] | DDmelt | Mean | Max | Min | Standard Deviation | Relative Standard Deviation |
|---|---|---|---|---|---|---|---|---|---|---|
| 1 | Aqua Velva | Resurgence | North | 2007-05-01 | 60.6 | | | | | |
| | | | | 2008-04-15 | 48.0 | | | | | |
| | | | | 2008-05-07 | 91.0 | | | | | |
| | | | | 2009-04-29 | 66.1 | | | | | |
| | | | | 2009-05-04 | 92.6 | 64.5 | 92.6 | 40.8 | 20.3 | 0.32 |
| | | | | 2010-04-15 | 44.7 | | | | | |
| | | | | 2010-04-19 | 52.0 | | | | | |
| | | | | 2011-04-27 | 40.8 | | | | | |
| | | | | 2011-05-06 | 84.8 | | | | | |
| 2 | Voile de la mariée (G-Voile) | Surface runoff | North | 2008-04-15 | 4.8 | | | | | |
| | | | | 2008-04-18 | 21.4 | | | | | |
| | | | | 2009-04-02 | 4.6 | | | | | |
| | | | | 2009-04-10 | 21.2 | | | | | |
| | | | | 2010-04-03 | 4.5 | 13.5 | 28.5 | 4.1 | 10.0 | 0.74 |
| | | | | 2010-04-07 | 28.5 | | | | | |
| | | | | 2011-04-10 | 4.1 | | | | | |
| | | | | 2011-04-13 | 18.9 | | | | | |
| 8 | Sans nom (G-Amphi) | Resurgence | North | 2008-04-28 | 48.0 | | | | | |
| | | | | 2008-04-30 | 62.6 | | | | | |
| | | | | 2009-04-24 | 41.4 | | | | | |
| | | | | 2010-04-15 | 44.7 | 50.6 | 65.9 | 40.8 | 11.0 | 0.22 |
| | | | | 2010-04-22 | 65.9 | | | | | |
| | | | | 2011-04-27 | 40.8 | | | | | |
| 10 | Corneille | Surface runoff | East-North-East | 2008-04-15 | 4.8 | | | | | |
| | | | | 2008-04-18 | 21.4 | | | | | |
| | | | | 2009-04-10 | 21.2 | | | | | |
| | | | | 2010-04-04 | 11.1 | | | | | |
| | | | | 2010-04-12 | 28.5 | 13.4 | 28.5 | 2.6 | 9.3 | 0.69 |
| | | | | 2011-04-11 | 11.5 | | | | | |
| | | | | 2012-03-29 | 6.2 | | | | | |
| | | | | 2012-04-05 | 2.6 | | | | | |
| 12 | Échappé belle | Resurgence | North | 2008-05-08 | 95.8 | | | | | |
| | | | | 2009-05-07 | 100.2 | | | | | |
| | | | | 2010-04-22 | 65.9 | 82.7 | 100.2 | 65.9 | 14.6 | 0.18 |
| | | | | 2010-04-24 | 76.5 | | | | | |
| | | | | 2011-05-04 | 75.3 | | | | | |
| 20 | Loup-Garou (G-69) | Resurgence | North | 2008-04-30 | 62.6 | | | | | |
| | | | | 2009-04-28 | 63.8 | 56.9 | 63.8 | 43.8 | 9.2 | 0.16 |
| | | | | 2010-04-20 | 57.5 | | | | | |
| | | | | 2011-04-28 | 43.8 | | | | | |
| 21 | Moment magique | Resurgence | South-West | 2000-04-21 | 46.1 | | | | | |
| | | | | 2004-04-22 | 18.3 | | | | | |
| | | | | 2005-04-25 | 50.5 | | | | | |
| | | | | 2005-04-29 | 62.6 | | | | | |
| | | | | 2006-04-13 | 42.2 | | | | | |
| | | | | 2006-04-21 | 65.5 | 45.4 | 66.3 | 18.3 | 16.4 | 0.36 |
| | | | | 2007-04-29 | 52.8 | | | | | |
| | | | | 2008-04-25 | 38.2 | | | | | |
| | | | | 2008-05-02 | 66.3 | | | | | |
| | | | | 2011-04-25 | 35.5 | | | | | |
| | | | | 2012-04-15 | 21.1 | | | | | |
| 22 | D'la belle visite | Surface runoff | South-West | 2004-04-18 | 5.5 | | | | | |
| | | | | 2004-04-21 | 10.3 | | | | | |
| | | | | *20/11/2004** | 4.9 | | | | | |
| | | | | *26/11/2004** | 17.6 | | | | | |
| | | | | 2008-04-20 | 25.5 | 13.7 | 25.5 | 4.9 | 6.7 | 0.49 |
| | | | | *03/12/2010** | 10.3 | | | | | |
| | | | | *04/12/2010** | 13.6 | | | | | |
| | | | | 2011-04-14 | 18.2 | | | | | |
| | | | | 2012-04-14 | 17.1 | | | | | |

[1] When only one date is presented, it means that the whole ice wall collapse in a single event. When two dates in the same year are presented, they represent the first and last ice fall event for this ice wall.

* Autumn ice fall

130

## 4.3. LOGISTIC MODELS

Many variables used during the development of the model show good correlations together (Tab. 5.2). The strong correlation between Tmin, Tmax, Dtr and Fi is natural although they represent distinct mechanisms fostering the melting or fracturing of rockwall icings. On the other hand, the direct effect of liquid precipitation on the melting process of rockwall icing should be represented by a single variable.

Signification tests of the models and variables are presented in Table 5.3. The DDmelt+DDmelt2 model (model 2) shows a better coefficient of determination ($R^2$) and a lower AIC than the DDp+DDp2 model (model 1). The simulated probability of falling ice blocks is higher for a narrower range of degree-days (Fig. 5.9A).

When used with the DDmelt+DDmelt2 model, P1 shows better predictive capacity than variables P2 and P3 (higher $R^2$ and lower AIC) (Tab. 5.2). The variable estimate is also more significant than the two other predictive variables.

A positive relationship was established between P1, Tmax, Tmin, Dtr, Ft, Ig and the ice blocks fall events (positive estimate value, Tab. 5.3). This means that a high value of these variables increases the probability of falling ice blocks: an ascertainment which is in accordance with the data analysis. In return, the Fi shows a negative relationship with the ice blocks fall probability. This is an unexpected effect because we had assumed that a strong decrease of the temperature below zero would increase the probability of falling ice blocks. This result can be explained by the limited number of ice blocks fall reported during high cooling time period (only three events reported with a Fi higher than 5$^o$C).

All the complex models tested (13 to 19) show acceptable $R^2$ (Tab. 5.3). At every step (backward stepwise analysis), the less significant variable in the model (highest p value or lowest Wald z-value) is eliminated. Tmin and P1 were withdrawn after the first two steps. Models 15 and 16 show the lowest AIC. Model 15 shows a slightly better $R^2$, but the Fi appears to be insignificant (p = 0.167). Furthermore, the Fi and Dtr variables are highly correlated together. They represent the same physical mechanism and unlike the Dtr, Fi shows a negative effect on the ice blocks fall probability. Following this logic, the best model choice should be model 16 (DDmelt+ DDmelt2 + Tmax + Dtr + Ft + Ig).

**Table 5.2.** Matrix of Pearson correlations between each variable used in the logistic models.

| | Icefall | Tmax | Tmin | DDmelt | DDmelt2 | Dtr | Ft | Fi | P1 | P2 | P3 | Ig |
|---|---|---|---|---|---|---|---|---|---|---|---|---|
| Icefall | 1 | .274 | .270 | -.030 | -.124 | .024 | .053 | -.330 | .136 | .142 | .148 | .066 |
| Tmax | .274 | 1 | .919 | .717 | .582 | .248 | .067 | -.649 | .224 | .268 | .300 | -.063 |
| Tmin | .270 | .919 | 1 | .703 | .569 | -.154 | .035 | -.841 | .271 | .327 | .354 | -.050 |
| DDmelt | -.030 | .717 | .703 | 1 | .947 | .070 | -.245 | -.494 | .166 | .216 | .248 | -.040 |
| DDmelt2 | -.124 | .582 | .569 | .947 | 1 | .059 | -.215 | -.356 | .133 | .171 | .190 | -.053 |
| Dtr | .024 | .248 | -.154 | .070 | .059 | 1 | .084 | .442 | -.105 | -.130 | -.120 | -.034 |
| Ft | .053 | .067 | .035 | -.245 | -.215 | .084 | 1 | .008 | -.045 | -.004 | .018 | -.061 |
| Fi | -.330 | -.649 | -.841 | -.494 | -.356 | .442 | .008 | 1 | -.261 | -.310 | -.337 | .014 |
| P1 | .136 | .224 | .271 | .166 | .133 | -.105 | -.045 | -.261 | 1 | .774 | .627 | -.015 |
| P2 | .142 | .268 | .327 | .216 | .171 | -.130 | -.004 | -.310 | .774 | 1 | .861 | -.018 |
| P3 | .148 | .300 | .354 | .248 | .190 | -.120 | .018 | -.337 | .627 | .861 | 1 | -.030 |
| Ig | .066 | -.063 | -.050 | -.040 | -.053 | -.034 | -.061 | .014 | -.015 | -.018 | -.030 | 1 |

**Table 5.3.** Statistical parameters of the logistic models (N=2832; ice block fall event = 440; no event = 2392).

| # | Models | K | Variables | Estimate | Std. Error | Wald Z | p | Sig.[1] | Delta AIC | Akaike Weight | Nagelkerke $R^2$ |
|---|--------|---|-----------|----------|------------|--------|---|---------|-----------|---------------|------------------|
| 1 | DDp+ DDp2 | 3 | (Intercept) | -3.222 | 0.115 | -27.92 | < 2E-16 | *** | 251.0 | 0.000 | 0.504 |
|   |         |   | DDp | 0.049 | 0.002 | 22.95 | < 2E-16 | *** |   |   |   |
|   |         |   | DDp2 | 0.000 | 0.000 | -19.03 | < 2E-16 | *** |   |   |   |
| 2 | DDmelt+ DDmelt2 | 3 | (Intercept) | -3.338 | 0.121 | -27.50 | < 2E-16 | *** | 162.7 | 0.000 | 0.542 |
|   |         |   | DDmelt | 0.087 | 0.004 | 23.12 | < 2E-16 | *** |   |   |   |
|   |         |   | DDmelt2 | 0.000 | 0.000 | -19.03 | < 2E-16 | *** |   |   |   |
| 3 | DDmelt+ DDmelt2+P1 | 4 | (Intercept) | -3.383 | 0.124 | -27.30 | < 2E-16 | *** | 156.9 | 0.000 | 0.545 |
|   |         |   | DDmelt | 0.086 | 0.004 | 22.80 | < 2E-16 | *** |   |   |   |
|   |         |   | DDmelt2 | 0.000 | 0.000 | -18.87 | < 2E-16 | *** |   |   |   |
|   |         |   | P1 | 0.037 | 0.013 | 2.81 | 0.005 | ** |   |   |   |
| 4 | DDmelt+ DDmelt2+P2 | 4 | (Intercept) | -3.375 | 0.124 | -27.22 | < 2E-16 | *** | 161.0 | 0.000 | 0.543 |
|   |         |   | DDmelt | 0.087 | 0.004 | 22.73 | < 2E-16 | *** |   |   |   |
|   |         |   | DDmelt2 | 0.000 | 0.000 | -18.84 | < 2E-16 | *** |   |   |   |
|   |         |   | P2 | 0.017 | 0.009 | 1.95 | 0.051 | . |   |   |   |
| 5 | DDmelt+ DDmelt2+P3 | 4 | (Intercept) | -3.357 | 0.124 | -27.16 | < 2E-16 | *** | 163.8 | 0.000 | 0.542 |
|   |         |   | DDmelt | 0.087 | 0.004 | 22.64 | < 2E-16 | *** |   |   |   |
|   |         |   | DDmelt2 | 0.000 | 0.000 | -18.80 | < 2E-16 | *** |   |   |   |
|   |         |   | P3 | 0.007 | 0.007 | 0.95 | 0.341 |   |   |   |   |
| 6 | P1 | 2 | (Intercept) | -1.803 | 0.056 | -32.25 | < 2E-16 | *** | 1184.3 | 0.000 | 0.025 |
|   |    |   | P1 | 0.064 | 0.010 | 6.57 | 0.000 | *** |   |   |   |
| 7 | Tmax | 2 | (Intercept) | -2.186 | 0.073 | -29.90 | < 2E-16 | *** | 1005.6 | 0.000 | 0.129 |
|   |      |   | Tmax | 0.091 | 0.007 | 13.90 | < 2E-16 | *** |   |   |   |
| 8 | Tmin | 2 | (Intercept) | -1.502 | 0.054 | -27.75 | < 2E-16 | *** | 999.3 | 0.000 | 0.132 |
|   |      |   | Tmin | 0.101 | 0.007 | 13.64 | < 2E-16 | *** |   |   |   |
| 9 | Dtr | 2 | (Intercept) | -1.828 | 0.120 | -15.23 | < 2E-16 | *** | 1223.6 | 0.000 | 0.001 |
|   |     |   | Dtr | 0.018 | 0.014 | 1.26 | 0.207 |   |   |   |   |
| 10 | Ft | 2 | (Intercept) | -1.781 | 0.062 | -28.82 | < 2E-16 | *** | 1217.4 | 0.000 | 0.005 |
|   |    |   | Ft | 0.323 | 0.114 | 2.83 | 0.005 | ** |   |   |   |
| 11 | Fi | 2 | (Intercept) | -0.761 | 0.062 | -12.22 | < 2E-16 | *** | 750.0 | 0.000 | 0.267 |
|   |    |   | Fi | -0.517 | 0.037 | -14.11 | < 2E-16 | *** |   |   |   |
| 12 | Ig | 2 | (Intercept) | -1.965 | 0.096 | -20.45 | < 2E-16 | *** | 1212.9 | 0.000 | 0.007 |
|   |    |   | Ig | 0.000 | 0.000 | 3.50 | 0.000 | *** |   |   |   |
| 13 | DDmelt+ DDmelt2 + P1 + Tmax + Tmin + Dtr + Ft + Fi + Ig | 10 | (Intercept) | -3.084 | 0.264 | -11.68 | < 2E-16 | *** | 3.2 | 0.058 | 0.612 |
|   |   |   | DDmelt | 0.055 | 0.004 | 12.65 | < 2E-16 | *** |   |   |   |
|   |   |   | DDmelt2 | 0.000 | 0.000 | -13.34 | < 2E-16 | *** |   |   |   |
|   |   |   | P1 | 0.011 | 0.012 | 0.91 | 0.361 |   |   |   |   |
|   |   |   | Tmax | 1.421 | 18.990 | 0.08 | 0.940 |   |   |   |   |
|   |   |   | Tmin | -1.174 | 18.990 | -0.06 | 0.951 |   |   |   |   |
|   |   |   | Dtr | -1.312 | 18.990 | -0.07 | 0.945 |   |   |   |   |
|   |   |   | Ft | 0.436 | 0.183 | 2.38 | 0.017 | * |   |   |   |
|   |   |   | Fi | -0.120 | 0.087 | -1.38 | 0.167 |   |   |   |   |
|   |   |   | Ig | 0.000 | 0.000 | 3.28 | 0.001 | ** |   |   |   |
| 14 | DDmelt+ DDmelt2 + P1 + Tmax + Dtr + Ft + Fi + Ig | 9 | (Intercept) | -3.084 | 0.264 | -11.68 | < 2E-16 | *** | 1.2 | 0.157 | 0.612 |
|   |   |   | DDmelt | 0.055 | 0.004 | 12.66 | < 2E-16 | *** |   |   |   |
|   |   |   | DDmelt2 | 0.000 | 0.000 | -13.35 | < 2E-16 | *** |   |   |   |
|   |   |   | P1 | 0.011 | 0.012 | 0.92 | 0.360 |   |   |   |   |
|   |   |   | Tmax | 0.247 | 0.054 | 4.55 | 0.000 | *** |   |   |   |
|   |   |   | Dtr | -0.138 | 0.060 | -2.30 | 0.022 | * |   |   |   |
|   |   |   | Ft | 0.436 | 0.183 | 2.38 | 0.017 | * |   |   |   |
|   |   |   | Fi | -0.120 | 0.087 | -1.38 | 0.167 |   |   |   |   |
|   |   |   | Ig | 0.000 | 0.000 | 3.28 | 0.001 | ** |   |   |   |
| 15 | DDmelt+ DDmelt2 + Tmax + Dtr + Ft + Fi + Ig | 8 | (Intercept) | -3.022 | 0.254 | -11.88 | < 2E-16 | *** | 0.0 | 0.285 | 0.612 |
|   |   |   | DDmelt | 0.054 | 0.004 | 12.64 | < 2E-16 | *** |   |   |   |
|   |   |   | DDmelt2 | 0.000 | 0.000 | -13.34 | < 2E-16 | *** |   |   |   |
|   |   |   | Tmax | 0.251 | 0.054 | 4.62 | 0.000 | *** |   |   |   |
|   |   |   | Dtr | -0.144 | 0.060 | -2.41 | 0.016 | * |   |   |   |
|   |   |   | Ft | 0.422 | 0.183 | 2.31 | 0.021 | * |   |   |   |
|   |   |   | Fi | -0.120 | 0.087 | -1.38 | 0.167 |   |   |   |   |
|   |   |   | Ig | 0.000 | 0.000 | 3.25 | 0.001 | ** |   |   |   |

| | Model | df | Term | Estimate | Std. Error | t value | p value | | ΔAIC | Weight | $R^2$ |
|---|---|---|---|---|---|---|---|---|---|---|---|
| 16 | DDmelt+ DDmelt2 + Tmax + Dtr + Ft + Ig | 7 | (Intercept) | -3.118 | 0.247 | -12.62 | < 2E-16 | *** | 0.0 | 0.285 | 0.611 |
| | | | DDmelt | 0.056 | 0.004 | 13.10 | < 2E-16 | *** | | | |
| | | | DDmelt2 | 0.000 | 0.000 | -14.36 | < 2E-16 | *** | | | |
| | | | Tmax | 0.313 | 0.033 | 9.39 | < 2E-16 | *** | | | |
| | | | Dtr | -0.211 | 0.037 | -5.77 | 0.000 | *** | | | |
| | | | Ft | 0.421 | 0.182 | 2.31 | 0.021 | * | | | |
| | | | Ig | 0.000 | 0.000 | 3.25 | 0.001 | ** | | | |
| 17 | DDmelt+ DDmelt2 + Tmax + Dtr + Ig | 6 | (Intercept) | -2.972 | 0.238 | -12.51 | < 2E-16 | *** | 3.5 | 0.050 | 0.609 |
| | | | DDmelt | 0.056 | 0.004 | 12.98 | < 2E-16 | *** | | | |
| | | | DDmelt2 | 0.000 | 0.000 | -14.29 | < 2E-16 | *** | | | |
| | | | Tmax | 0.281 | 0.027 | 10.27 | < 2E-16 | *** | | | |
| | | | Dtr | -0.175 | 0.031 | -5.66 | 0.000 | *** | | | |
| | | | Ig | 0.000 | 0.000 | 3.22 | 0.001 | ** | | | |
| 18 | DDmelt+ DDmelt2 + Tmax + Dtr | 5 | (Intercept) | -2.597 | 0.202 | -12.88 | < 2E-16 | *** | 12.0 | 0.001 | 0.605 |
| | | | DDmelt | 0.056 | 0.004 | 13.12 | < 2E-16 | *** | | | |
| | | | DDmelt2 | 0.000 | 0.000 | -14.40 | < 2E-16 | *** | | | |
| | | | Tmax | 0.282 | 0.028 | 10.27 | < 2E-16 | *** | | | |
| | | | Dtr | -0.182 | 0.031 | -5.87 | 0.000 | *** | | | |
| 19 | DDmelt+ DDmelt2 + Tmax | 4 | (Intercept) | -3.541 | 0.146 | -24.24 | < 2E-16 | *** | 49.2 | 0.000 | 0.589 |
| | | | DDmelt | 0.065 | 0.004 | 15.58 | < 2E-16 | *** | | | |
| | | | DDmelt2 | 0.000 | 0.000 | -15.55 | < 2E-16 | *** | | | |
| | | | Tmax | 0.176 | 0.018 | 9.97 | < 2E-16 | *** | | | |

Best model AIC = 1225.2

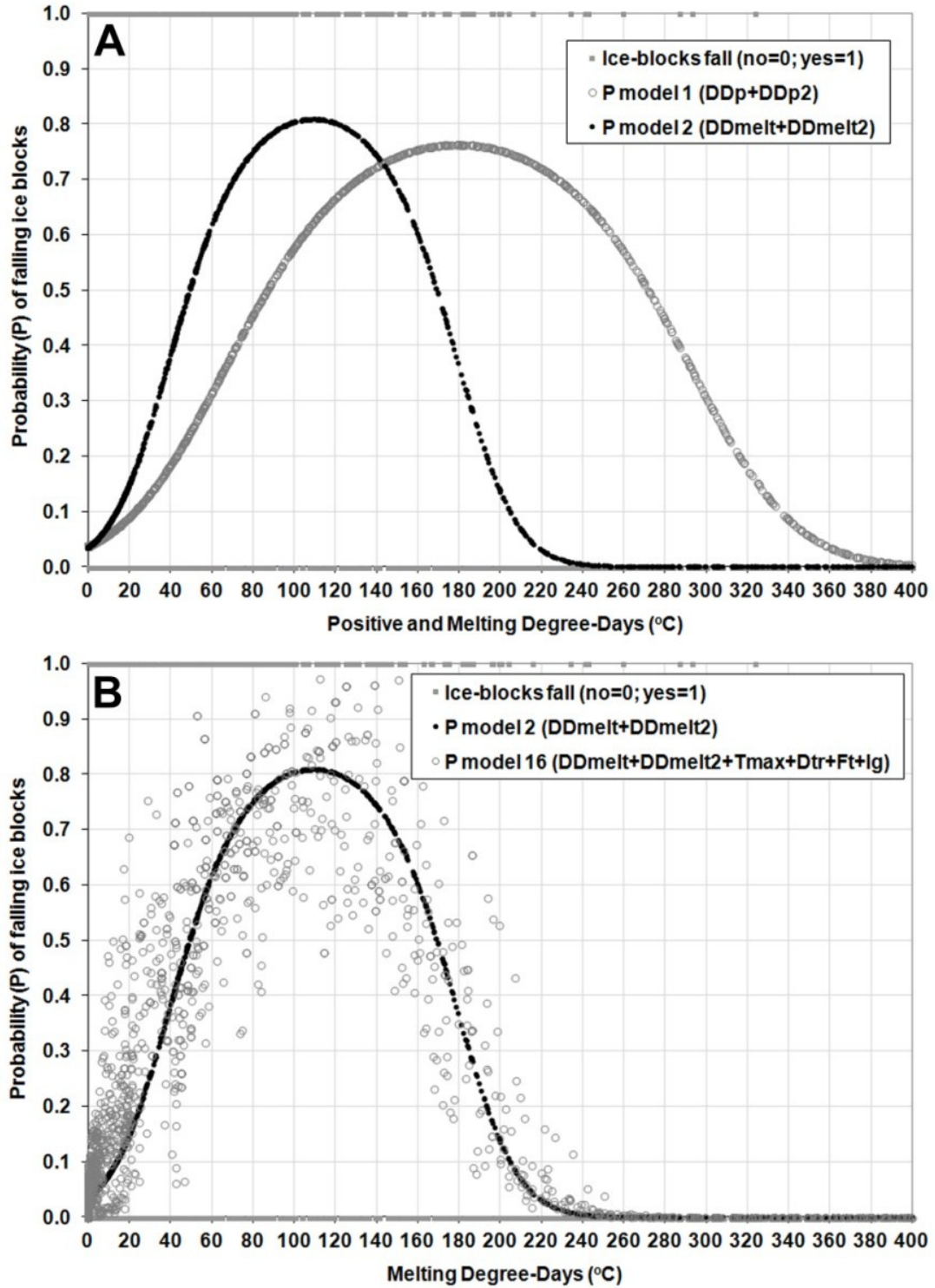[1] Signification codes:  0 '***' 0.001 '**' 0.01 '*' 0.05 '.' 0.1 ' ' 1

134

**Figure 5.9.** Probability of ice blocks fall: model 1 versus model 2 (A) and model 2 versus model 16 (B).

## 4.4. ICE BLOCKS FALL PREDICTION METHOD

In Figure 5.10, we proposed an ice blocks fall forecasting method. In 2011, we followed the weather evolution, the DDmelt and the best logistic model (model #16) and we tried to predict the collapse of specific rockwall icings and targeted the most hazardous periods. From the last season's DDmelt range, the ice cascades (#2, 10 and 22) should collapse after 2.6 to 16.4 DDmelt. All the ice cascades melted and fell apart in their own range of DDmelt and during a high increase of falling ice blocks probability caused by an increase of Tmax and during a period of high Dtr with many Ft cycles (Fig. 5.10 and Tab. 5.1). During the same periods, some interventions were reported by the M.T.Q.. The south facing ice wall #21 collapsed on April 25th after 35.5 DDmelt and during a warm and sunny spring day (Tmax = 10.6$^{o}$C). The high and rising temperatures between April 20th and 26th and the high Dtr has greatly increased the probability of ice blocks fall along the road of northern Gaspésie. During this highly hazardous period, the number of interventions was very high (Fig. 5.10). An unstable ice column broke down from the Aqua Velva ice wall (#1) on April 27th, while the rest of the ice wall collapsed on May 6th. The first event happened earlier than predicted, but it was of small magnitude and the ice blocks did not reach the road. The second event occurred in the range of DDmelt reported over the previous melting seasons (Table 5.9) and after a significant increase of Tmax and a high Dtr. Ice walls #8 and 20 collapsed at the beginning of their predicted periods. It was not during a warm day or after a high Dtr or Ft cycle. But, it was during 3 mm and 28 mm rain events, respectively. Finally, Échappé Belle (ice wall #12) collapsed in the middle of its previous years range of DDmelt and also during a rain event (27 mm). Most of the other M.T.Q. interventions occurred during high temperature periods with high probability of ice blocks falls (between April 27th and May 5th). After that, most of the rockwalls were free of ice and very few events were reported. The probability of falling ice blocks decreased drastically after May 19th and no ice blocks falls were reported after this date.
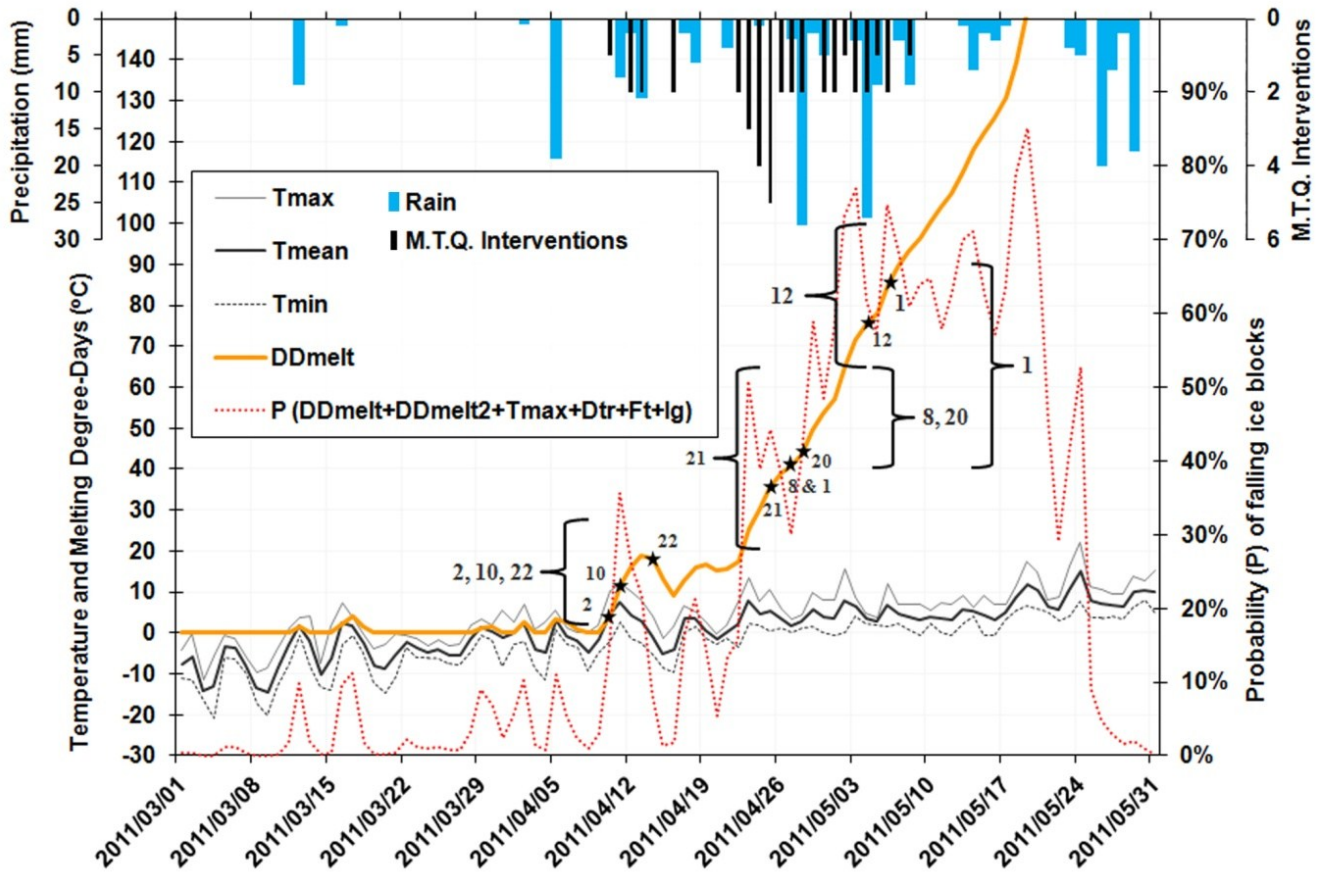
**Figure 5.10.** Spring 2011 follow up of the daily mean, maximum and minimum air temperature, liquid precipitation, the melting degree-day, the model 16 (DDmelt+ DDmelt2 + Tmax + Dtr + Ft + Ig) and the M.T.Q. interventions. N.B.: The brackets represent the range of DDmelt reported over the previous years for eight specifics rockwall icings (#1, 2, 8, 10, 12, 20, 21 and 22); the stars represent the 2011 collapsing dates of the eight specifics rockwall icings.

## 5. CONCLUSIONS

This study shows that rockwall icings collapse process is closely related to weather conditions. Because the ice blocks falls are mainly controlled by the increase of temperatures above the melting point of ice, the DDmelt is representative of the various heat transfers into these types of ice bodies. Heavy rain events also accelerate the melting of the ice on the cliff faces. The mechanical stress induce by rapid air cooling or low temperature and sometimes resulting in the collapse of fragile ice structures were also considered by introducing the daily temperature range (Dtr), the cooling or freezing intensity (Fi) and the freeze-thaw cycles (Ft) in the forecasting model. A rockwall index growth was also correlated with the number of interventions occurring each year.

All these variables were used to develop logistics predictive models for the whole study area. The best predictive model is composed of six descriptive variables: DDmelt, DDmelt2, Tmax, Dtr, Ft and Ig. The minimum temperature (Tmin), the total daily liquid precipitation (P1) and the freezing intensity (Fi) were withdrawn from the model due to a lack of significance.

Because the interannual variability of the DDmelt is very small before reaching the breaking point of the different rockwall icings, it is possible to predict the collapse of some of the most problematic of them. However, additional studies would be needed to explain this specificity of the DDmelt between the different ice formations. We believe that the variability of the water flow at each sites, the rockwall geomorphology and the morphology of the ice structure itself are part of the answer. On a regional scale, the logistic model can be used to target the most hazardous periods along the northern Gaspésie roads. However, even if the total daily precipitation (P1) was not retained as a highly significant variable in the development of the model, the result of the ice blocks fall forecasting method has clearly shown that many events occur during heavy rain events.

In this research, we demonstrated that external meteorological variables are the main factors controlling the rockwall icing melting and collapsing processes. However, glaciological (ice structure), hydrological (runoff origin or discharge), geomorphic (slope angle, aspect) factors also need to be taken into consideration when managing the risk of ice blocks fall.

138

# CHAPITRE 6: CONCLUSIONS GÉNÉRALES

## 1. SYNTHÈSE

Dans le nord de la Gaspésie, 60 glaces de paroi ont été localisées près des routes. Sur ce nombre, 22 sont considérées comme problématiques ou représentant un risque pour le Ministère des Transports du Québec (M.T.Q.). Certaines d'entre elles peuvent atteindre deux à trois mètres d'épaisseur et accumuler plus de 3000 m$^3$ de glace. La fonte et l'écroulement de ces structures de glace entrainent la chute de blocs de glace sur les routes du nord de la Gaspésie. Afin de mieux comprendre les mécanismes de leur formation et de leur fonte, plusieurs de ces formations de glace ont fait l'objet d'un suivi photographique continu. Des échantillons de glace ont été prélevés afin de procéder à des analyses tomodensitométriques et cristallographiques. L'évolution volumétrique de quatre glaces de paroi a été modélisée à l'aide de différents modèles thermodynamiques et validée à partir de mesures du volume de glace effectuées sur des images acquises au LiDAR terrestre. Chacune des glaces de paroi choisies présentait des caractéristiques hydrologiques, géomorphologiques ou géographiques différentes. Enfin, une méthode de prévision des chutes de blocs de glace a été développée en comparant les interventions du M.T.Q. pour déloger les blocs de glace tombés sur la chaussée aux données météorologiques d'Environnement Canada.

L'étude des diverses formes et structures de glace a permis d'identifier quatre types de glaces constituant les glaces de paroi :

- Les glaces de ruissellement sont issues du gel progressif d'une pellicule d'eau ruisselante à la surface des structures rocheuses. Elles forment des pellicules et des stalactites de glace qui dominent les formations de glace de paroi. La densité apparente de la glace y est élevée, se rapprochant de celle de la glace pure. La structure cristalline des stalactites est à l'image de sa dynamique globale de croissance : du haut vers le bas, principalement le long d'un cristal central et radialement du centre vers l'extérieur.

• Les accrétions de glace représentent le second type de glace constituant les glaces de paroi. Elles sont le résultat du gel plus ou moins rapide des gouttelettes d'eau chutant et s'étalant sur un obstacle. Ces accumulations de glace présentent une densité apparente inférieure à celle des glaces de ruissellement, en raison d'une abondance de bulles d'air endogènes. La structure cristalline est homogène avec des cristaux de petite et moyenne taille qui croissent sans direction préférentielle.

• Des croûtes de glace de neige peuvent également se former lors de la métamorphose de la neige en glace sur de petits replats des glaces de paroi. Elles forment des croûtes de glace poreuses constituées de petits cristaux allongés près de la surface et de cristaux de tailles diverses ne présentant pas de direction préférentielle de croissance à la base.

• Les glaces de regel sont le résultat de la fusion de ces divers types de glace au cours de l'hiver. Avec les cycles de gel et de dégel, plusieurs cristaux de glace s'amalgament pour former des grains de plus grande dimension sans direction de croissance préférentielle. La formation d'un réseau de microfractures à la frontière de nombreux cristaux engendre une glace avec une plus faible densité apparente.

À plus grande échelle, les glaces de paroi peuvent être classifiées en fonction de deux critères hydrologiques :

• Les carapaces de glaces issues du gel des eaux d'une résurgence sur une falaise (petit débit limité par le potentiel hydrogéologique).

• Les cascades de glace résultant du gel des eaux d'une chute sur une falaise (débit plus élevé limité par la taille du bassin versant).

Ces dernières peuvent également être classifiées en fonction de deux critères mécaniques fortement dépendants de la géomorphologie des falaises sur lesquelles elles se forment :

• Les glaces autoportantes se forment au niveau des surplombs rocheux. Elles forment des structures suspendues (sans appui au sol) ou colonnaires (avec appui au sol à leur base) dont l'équilibre statique repose essentiellement sur leur propre résistance mécanique interne.

- Les glaces adhérentes ou partiellement adhérentes se forment sur des falaises verticales ou sub-verticales. Elles forment des structures dont le centre de masse est dirigé partiellement ou en totalité vers la paroi rocheuse.

Ces caractéristiques influencent la dynamique de croissance, de fonte et de dislocation des glaces de paroi. Dans tous les cas, les modèles thermodynamiques développés ont démontré que le taux de croissance et de fonte des glaces de paroi est fortement dépendant de la température de l'air, mais plus spécifiquement du taux de transfert de chaleur par convection du système constitué d'eau et de glace vers l'atmosphère.

Dans le cas d'une cascade de glace orientée vers le nord, le taux de croissance est aussi dépendant de la diminution du débit liquide. Lorsque celui-ci atteint son niveau de base, la croissance est optimale. Cependant, la formation d'une couverture de glace recouvrant complètement la surface de la chute d'eau forme un isolant naturel. Les transferts de chaleur entre l'eau et l'atmosphère sont alors limités par l'épaisseur du couvert de glace. La croissance devient alors étroitement contrôlée par les fluctuations quotidiennes du bilan radiatif : formation de glace durant la nuit et fonte durant le jour. Il en résulte une dynamique en deux phases : une phase de croissance initiale contrôlée par la convection de l'air suivie d'une phase de croissance ralentie et de stabilité contrôlée par l'évacuation de chaleur par rayonnement. Au printemps, la fonte et la dislocation du couvert de glace résultent principalement d'une augmentation du rayonnement solaire direct et diffus durant le jour et de la hausse du flux de chaleur sensible associée à l'augmentation du débit liquide.

Dans le cas des carapaces de glace exposées au nord, l'eau provient généralement de multiples sources résurgentes sur la falaise : la formation de la glace à la surface de ces parois rocheuses est complexe. De nombreuses exfiltrations d'eau ont été observées sur la surface des carapaces durant leur formation. Il en résulte une dynamique de croissance essentiellement contrôlée par le transfert convectif de la chaleur de l'eau ruisselant à la surface des structures de glace vers l'atmosphère. La fonte est à la fois le résultat de la hausse des températures au-dessus du point de fusion de la glace et du transfert convectif de chaleur et celui d'une exposition plus marquée au rayonnement solaire. Lorsqu'elles sont exposées au sud, la croissance est ralentie. Elle s'effectue principalement durant la nuit.

Lors des journées ensoleillées, le rayonnement solaire durant le jour fourni une quantité d'énergie généralement supérieure à l'énergie évacuée par convection. Il en résulte une dynamique fluctuante de croissance et de fonte fortement contrôlée par l'équilibre relatif entre les transferts convectifs et le bilan radiatif à la surface de la carapace de glace.

Puisque la croissance et la fonte sont principalement contrôlées par les transferts convectifs à la surface des glaces de paroi, surtout celles d'orientation nord, l'élaboration d'un modèle simple basé sur le calcul des degrés-heures de gel ou de fonte (DH) a permis de modéliser leur évolution volumétrique avec une précision acceptable. L'ajout du bilan radiatif à ce modèle a également permis de simuler la croissance et la fonte d'une glace de paroi exposée au rayonnement solaire.

Puisque la fonte et l'écroulement des glaces de paroi sont étroitement reliés aux conditions météorologiques, il a été possible de développer des modèles logistiques de prévision des chutes de blocs de glace sur les routes du nord de la Gaspésie. Certaines variables, comme la température maximum de l'air et les précipitations liquides favorisent la fonte des couverts de glace et accroissent la probabilité de chutes de blocs de glace sur les routes du nord de la Gaspésie. D'autres, comme les cycles de gel et de dégel et les écarts quotidiens de la température de l'air peuvent entrainer des chocs thermomécaniques suffisants pour déstabiliser certaines structures de glace instables comme les formations de glace suspendue ou colonnaire. Le meilleur modèle de prévision est une version à six variables descriptives composées d'un indice annuel de croissance des glaces de paroi (Ig), des cycles de gel-dégel (Ft), de l'écart quotidien de la température (Dtr), de la température maximale de l'air (Tmax), des degrés-jours de fonte (DDmelt) et des DDmelt élevés au carré (DDmelt2). Il a également été démontré que le nombre de degrés-jours de fonte accumulé avant l'écroulement d'une glace de paroi donnée est restreint et du même ordre d'une année à l'autre. Cette variable simple, déduite du développement des modèles thermodynamiques, présente un avantage sur le plan de la gestion du risque d'écroulement de ces formations de glace. Au printemps 2011, le suivi des degrés-jours de fonte et du meilleur modèle logistique a permis de prédire l'écroulement de huit glaces de paroi avec une précision très acceptable étalée sur quelques jours dans la plupart des cas. Il a également été possible de cibler les périodes plus à risque sur le territoire nord-gaspésien.

Ces outils de prévision des chutes de blocs de glace constituent une étape importante vers une gestion plus efficace de l'aléa.

## 2. PROSPECTIVES ET RECOMMANDATIONS

Les avancées scientifiques et les outils de prévision des chutes de blocs de glace présentées dans cette thèse sont novateurs et efficaces. Malgré ce constat positif, certaines mesures visant la protection du réseau routier nord-gaspésien devrait être entreprises. Par exemple, des infrastructures de protection fixes devraient être installées sous les deux ou trois glaces de paroi les plus problématiques. La méthode de prévision développée pourrait être utilisée pour cibler les périodes à risque et accroitre l'efficacité des interventions. Par exemple, le modèle permettrait le déploiement d'un panneau indicateur mobile avertissant les usagers de la route qu'ils pénètrent dans une zone à risque. Enfin, comme tant d'autres études en science naturelle et génie, les réponses apportées soulèvent inévitablement de nouvelles interrogations. Les investigations futures devraient porter sur certains de ces aspects :

- Approfondir l'étude « morphodynamique » des divers types et formes de glace en fonction des conditions hydrométéorologiques (p.ex. : taux de croissance et morphologie des stalactites et des accrétions de glace en fonction de la température de l'air, du débit entrant et de la vitesse du vent);

- Déterminer plus précisément un coefficient de transfert convectif pour l'étude des systèmes eau-air-glace sur paroi verticale;

- Mesurer l'albédo des glaces de paroi sous diverses conditions d'exposition et durant différentes périodes au cours de l'hiver;

- Développer une technique de mesure permettant d'estimer les volumes de glace évacués au pied des chutes d'eau;

- Préciser le débit des résurgences d'eau souterraine sur les falaises;

- Évaluer les impacts des changements climatiques sur la formation et la fonte des glaces de paroi et sur la récurrence saisonnière des chutes de blocs de glace;

• Calculer la probabilité d'impact entre un véhicule et un bloc de glace sur les routes nord-gaspésiennes afin de déterminer si les chutes de blocs de glace demeurent sous le niveau du risque acceptable;

• Tester l'efficacité des capteurs sismiques ou acoustiques pour détecter l'écroulement d'une glace de paroi.

• Développer des outils d'aide à la décision adaptés au besoin des adeptes de l'escalade glace.

# BIBLIOGRAPHIE

American and Canadian Alpine Club 1999. Accidents in North American Mountaineering. Golden, CO. American Alpine Club.

Ambach, W. 1988. Interpretation of the positive-degree-days factor by heat balance characteristics - West Greenland. Nordic Hydrology, **19**(4): 217–224.

Ancey, C. 2006. Dynamique des avalanches. Presses polytechniques et universitaires Romandes, Lausanne, Suisse & Cermagref, Antony, France.

Andres, D. 1995. Frazil Generation and Ice Floe Formation on a Regulated river. 8th Workshop on the Hydraulics of Ice Covered Rivers (CRIPE), 1995, Kamloops, Canada. Canadian Geophysical Union, 59-75.

Ashton, G.D. 1989. Thin Ice Growth. Water Resources Research, **25**(3): 564–566.

Atlas, D., Srivastava, R.C. & Sekhon, R.S. 1973. Doppler radar characteristics of precipitation at vertical incidence. Reviews of Geophysics, **11**(1): 1-35.

Baltsavias, E.P. 1999. Aiborne laser scanning: basic relations and formulas. ISPRS Journal of Photogrammetry and Remote Sensing, **54**: 199-214.

Bayard, D., Stähli, M., Parriaux, A. & Flühler, H. 2005. The influence of seasonally frozen soil on the snowmelt runoff at two Alpine sites in southern Switzerland. Journal of Hydrology, **309**(1-4): 66-84.

Bianchi, A. 2004. Frozen waterfalls: How they develop, how they collapse., IFMGA-IVBVUIAGM, Union Internationale des Associations de Guide de Montagne, 23 pp.

Bloomer, J.R. 1981. Thermal conductivities of mudrocks in the United Kingdom. Quarterly Journal of Engineering Geology and Hydrogeology, **14**(4): 357-362.

Boespflug, X., Ross, N., Long, B.F. & Dumais, J.F. 1994. Tomodensimetrie axiale: relation entre l'intensité tomographique et la densité de la matière. Canadian Journal of Earth Sciences, **31**: 426–434.

Bolsenga, S.J. 1969. Total albedo of Great Lakes ice. Water Resour. Res., **5**(5): 1132-1133.

Braithwaite, R.J. 1981. On glacier energy balance, ablation, and air temperature. Journal of Glaciology, **27**(97): 381-391.

Braithwaite, R.J. 1995. Positive degree-day factors for ablation on the Greenland ice sheet studied by energy-balance modelling. Journal of Glaciology, **41**: 153-160.

Brisebois, D. & Nadeau, J. 2003. Géologie de la Gaspésie et du Bas-Saint-Laurent (SNRC 22A, 22B, 22C, 22G, 22H, 21N et 21O). Ministère des Ressources Naturelles, de la Faune et des Parcs (MRNFP), Québec. DV 2003-08, échelle 1/250 000.

Burnham, K.P. & Anderson, D.R. 2002. Model Selection and Multimodel Inference: a practical information-theoretic approach. Springer-Verlag, New York.

Calmels, F. & Allard, M. 2004. Ice segregation and gas distribution in permafrost using tomodensitometric analysis. Permafrost and Periglacial Processes, **15**(4): 367-378.

Cazorzi, F. & Dalla Fontana, G. 1996. Snowmelt modelling by combining air temperature and a distributed radiation index. Journal of Hydrology, **181**(1–4): 169-187.

Colbeck, S.C. 1979. Water flow through heterogeneous snow. Cold Regions Science and Technology, **1**(1): 37-45.

Colbeck, S.C. 1982. An Overview of Seasonal Snow Metamorphism. Reviews of Geophysics and Space Physics, **20**(1): 45-61.

Colbeck, S.C. 1983. Theory of metamorphism of dry snow. Journal of Geophysical Research, **88**(C9): 5475-5482.

Day, T.J. 1976. On the precision of salt dilution gauging. Journal of Hydrology, **31**: 293-306.

de Bruyn, J.R. 1997. On the formation of periodic arrays of icicles. Cold Regions Science and Technology, **25**(3): 225-229.

Dingman, S.L. 2008. Physical Hydrology, second edition. Waveland Press Inc., Long Grove, Illinois.

Domenico, P.A. & Schwartz, W.W. 1990. Physical and chemical hydrogeology. John Wiley & Sons, New York.

Driese, S.G., McKay, L.D. & Penfield, C.P. 2001. Lithologic and Pedogenic Influences on Porosity Distribution and Groundwater Flow in Fractured Sedimentary Saprolite: A New Application of Environmental Sedimentology. Journal of Sedimentary Research, **71**(5): 843-857.

Duchesne, M.J., Moore, F., Long, B.F. & Labrie, J. 2009. A rapid method for converting medical Computed Tomography scanner topogram attenuation scale to Hounsfield Unit scale and to obtain relative density values. Engineering Geology, **103**(3–4): 100-105.

Durand, G., Gagliardini, O., Thorsteinsson, T., Svensson, A., Kipfstuhl, S. & Dahl-Jensen, D. 2006. Ice microstructure and fabric: an up-to-date approach for measuring textures. Journal of Glaciology, **52**(179): 619-630.

Environnement Canada 1971-2000. Normales et moyennes climatiques au Canada 1971-2000 [on-line]. Available at http://climat.meteo.gc.ca/climate_normals/results_f.html?stnID=5816&lang=f&dCode=0&province=QUE&provBut=Recherche&month1=0&month2=12 [consulted July 2012].

Environnement Canada 2000-2012. Service météo, Données climatiques au Canada [on-line]. Available at http://climat.meteo.gc.ca/climateData/dailydata_f.html?Prov=QC&StationID=27195&timeframe=2&Month=1&Year=2000&cmdB1=Allez [consulted July 2012].

Fortin, G., Ilinca, A. & Laforte, J.L. 2004. Modèle d'accrétion de glace sur un objet bidimensionnel fixe appliquable aux pales d'éoliennes. VertigO – La revue en sciences de l'environnement, **5**(1): 1-9.

Gadd, W. 2006. Ice & Mixed Climbing: Moderne Technique. The Mountaineers Books, Seattle.

Gagnon, R.M. 1970. Climat des Chic-Chocs. Ministère des Richesses naturelles, Québec, MP 36, p. 103.

Gauthier, F. 2008. Les glaces de paroi: Formation, écroulement et impact géomorphologique, Mémoire de maîtrise, INRS-ETE, Québec, Canada.

Gauthier, F., Hétu, B. & Bergeron, N. 2012. Analyses statistiques des conditions climatiques propices aux chutes de blocs de glace dans les corridors routiers du nord de la Gaspésie, Québec, Canada. Canadian Geotechnical Journal, **49**(12): 1408-1426.

Gauthier, F., Hétu, B. & Bergeron, N. 2013. Impacts géomorphologiques des chutes de blocs de glace sur les versants du nord de la Gaspésie (Québec, Canada). Canadian Journal of Earth Sciences, **50**(4): 406-422.

Gautschi, A. 2001. Hydrogeology of a fractured shale (Opalinus Clay): Implications for deep geological disposal of radioactive wastes. Hydrogeology Journal, **9**(1): 97-107.

Girard, J.-F. & Hétu, B. 1994. Les mouvements de masse en Gaspésie septentrionale, Hydro-Québec, 45 pp.

Gottlieb, L. 1980. Development and applications of a runoff model for snow-covered and glacierized basins. Nordic Hydrology, **11**(5): 255-272.

Groleau, M. 1994. Impacts géomorphologiques et écologiques des chutes de glace de paroi sur l'évolution d'un versant forestier, Mont-Saint-Pierre, Gaspésie septentrionale, Université Laval, Québec, Canada.

Gunn, R. & Kinzer, G.D. 1949. The terminal velocity of fall for water droplets in stagnant air. Journal of Meteorology, **6**: 243-248.

Hanley, T.O.D. & Michel, B. 1977. Laboratory formation of border ice and frazil slush. Canadian Journal of Civil Engineering, **4**(2): 153-160.

Hay, J.E. & Fitzharris, B.B. 1988. A comparison of the energy-balance and bulk-aerodynamic approaches for estimating glacier melt. Journal of Glaciology, **34**: 145-153.

Heath, R.C. 1983. Basic Ground-water hydrology. U.S. Geological Survey Water Supply Paper 2220.

Hebertson, E.G. & Jenkins, M.J. 2003. Historical climate factors associated with major avalanche years on the Wasatch Plateau, Utah. Cold Regions Science and Technology, **37**: 315–332.

Hétu, B. & Gray, J.T. 1985. Le modelé glaciaire du centre de la Gaspésie septentrionale, Québec. Géographie physique et Quaternaire, **39**(1): 47-66.

Hétu, B. & Vandelac, P. 1989. La dynamique des éboulis schisteux au cours de l'hiver, Gaspésie septentrionale, Québec. Géographie physique et Quaternaire, **43**(3): 389-406.

Hétu, B., Girard, J.-F. & Boisjoly, J. 1994. Les risques naturels reliés à la dynamique des versants dans le nord de la Gaspésie : zone littorale et mont Albert. Bulletin de l'Association québécoise pour l'étude du Quaternaire, **20**(2): 9-15.

Hock, R. 1998. Modelling of glacier melt and discharge., Report ISBN 3-906148-18-1, Zürcher Geographische Schriften 70, Geogr. Inst. ETH, Zürich, 140 pp.

Hock, R. 1999. A distributed temperature-index ice- and snowmelt model including potential direct solar radiation. Journal of Glaciology, **45**(149): 101-111.

Hock, R. 2003. Temperature index melt modelling in mountain areas. Journal of Hydrology, **282**(1-4): 104-115.

Hock, R. 2005. Glacier melt: a review of processes and their modelling. Progress in Physical Geography, **29**(3): 362-391.

Hosmer, D. & Lemeshow, S. 2000. Applied logistic regression, New York.

Hounsfield, G.N. 1973. Computerized transverse axial scanning (tomography). Part 1. Description of system. British Journal of Radiology, **46**: 1016–1022.

Hu, X., Pollard, W.H. & Lewis, J.E. 1999. Energy exchange during river icing formation in a subarctic environment, Yukon Territory. Géographie physique et Quaternaire, **53**(2): 223-234.

James, T.D., Murray, T., Barrand, N.E. & Barr, S.L. 2006. Extracting photogrammetric ground control from lidar DEMs for change detection. The Photogrammetric Record, **21**(116): 312-328.

Jomelli, V., Chochillon, C., Brunstein, D. & Pech, P. 2003. Hillslope Debris Flows Frequency Since the Beginning of the 20th Century in the French Alps. *Edited by* C. Rickenmann, IAHS publication, Millpress, Rotterdam. pp. 127–137.

Jomelli, V., Pech, P., Chochillon, C. & Brunstein, D. 2004. Geomorphic variations of debris flows and recent climatic change in the French Alps. Climatic Change, **64**: 77–102.

Jomelli, V., Delval, C., Grancher, D., Escande, S., Brunstein, D., Hetu, B., Filion, L. & Pech, P. 2007. Probabilistic analysis of recent snow avalanche activity and weather in the French Alps. Cold Regions Science and Technology, **47**(1-2): 180-192.

Jones, K.F. 1996. Ice Accretion in Freezing Rain, U.S. Army Corps of Engineers, CRREL.

Kharitonsky, D. & Gonczarowski, J. 1993. A physically based model for icicle growth. The Visual Computer, **10**: 88-100.

Knight, C.A. 1980. Icicles as crystallization phenomena. Journal of Crystal Growth, **49**: 193-198.

Knoll, G.F. 1989. Radiation Detection and Measurement, John Wiley & Sons: New York.

Laudise, R.A. & Barns, R.L. 1979. Are icicles single crystals? Journal ofCrystal Growth, **46**: 379-386.

Lliboutry, L. 1964. Traité de glaciologie. Tome 1: Glace, neige et hydrologie nivale. Masson & Cie, Paris.

Lock, G.S.H. 1990. The growth and decay of ice. Cambridge University Press, Cambridge.

Macklin, W.C. & Payne, G.S. 1967. A theoretical study of the ice accretion process. Quarterly Journal of the Royal Meteorological Society, **93**(396): 195-213.

Macklin, W.C. & Payne, G.S. 1969. The spreading of accreted droplets. Quarterly Journal of the Royal Meteorological Society, **95**(406): 724-730.

Maeno, N. & Nishimura, K. 1979. Fluidization of snow. Cold Regions Science and Technology, **1**(2): 109-120.

Maeno, N., Makkonen, L. & Takahashi, T. 1994a. Bent icicles and spikes. Annals of glaciology, **19**: 138-140.

Maeno, N., Makkonen, L., Nishimura, K., Kosugi, K. & Takahashi, T. 1994b. Growth rates of icicles. Journal of Glaciology, **40**(135): 319–326.

Mah, C.H. & Wyllie , D.C. 2004. Rock Slope Engineering : Civil and mining, 4th Edition. Spon Press, New York.

Makkonen, L. 1988. A model of icicle growth. Journal of Glaciology, **34**(116): 64–70.

Makkonen, L. 2000. Models for the Growth of Rime, Glaze, Icicles and Wet Snow on Structures. Philosophical Transactions: Mathematical, Physical and Engineering Sciences, **358**(1776): 2913-2939.

Martin, S. 1981. Frazil ice in rivers and oceans. Annual Review of Fluid Mechanics, **13**(1): 379-397.

Mazerolle, M.J. 2004. Appendix 1: Making sense out of Akaike's Information Criterion (AIC): its use and interpretation in model selection and inference from ecological data. *In* In: Mouvements et reproduction des amphibiens en tourbières perturbées, Thèse de docotrat, Faculté de foresterie et de géomatique, Université Laval, Québec.

McClung, D. & Schaerer, P. 2006. The Avalanche Handbook, 3rd Edition. The Mountaineers Books, Leicester, Englang.

McCullagh, P. & Nelder, J.A. 1989. Generalized Linear Models. Chapman and Hall, Monographs on Statistics and Applied Probability, London.

McKay, L.D., Driese, S.G., Smith, K.H. & Vepraskas, M.J. 2005. Hydrogeology and pedology of saprolite formed from sedimentary rock, eastern Tennessee, USA. Geoderma, **126**(1-2): 27-45.

Meylan, P., Favre, A.-C. & Musy, A. 2008. Hydrologie fréquentielle: une science prédictive, Lausanne, Suisse.

Michel, B. 1971. Winter regime of rivers and lakes., Monogr. lII-Bla, Cold Reg. Res. Eng. Lab. Hanover, N.H. 131 pp.

Montagnat, M., Weiss, J., Cinquin-Lapierre, B., Labory, P.A., Moreau, L., Damilano, F. & Lavigne, D. 2010. Waterfall ice: formation, structure and evolution. Journal of Glaciology, **56**(196): 225-234.

Moore, G.K. 1988. Concepts of Groundwater Occurrence and Flow Near Oak Ridge National Laboratory, TN. Oak Ridge National Labratory, Oak Ridge, TN. ORNL/TM-10969.

Moore, R.D. 2004a. Introduction to salt dilution gauging for streamflow measurement: Part 1. Streamline Watershed Management Bulletin, **7**(4): 20-23.

Moore, R.D. 2004b. Introduction to salt dilution gauging for streamflow measurement Part II: Constant-rate injection. Streamline Watershed Management Bulletin, **8**(1): 11-15.

Moore, R.D. 2005. Sluginjection using salt in solution. Streamline Watershed management bulletin, **8**(2): 1-6.

Munro, D.S. 1989. Surface roughness and bulk heat transfer on a glacier: comparision with eddy correlation. Journal of Glaciology, **35**(121): 343-348.

Ogawa, N. & Furukawa, Y. 2002. Surface instability of icicles. Physical Review E, **66**(4): 041202.

Oke, T.R. 1987. Boundary Layer Climates, Routledge, New-York.

Osterkamp, T.E. & Gosink, J.P. 1983. Frazil ice formation and ice cover development in interior Alaska streams. Cold Regions Science and Technology, **8**(1): 43-56.

Rabatel, A., Deline, P., Jaillet, S. & Ravanel, L. 2008. Rock falls in high-alpine rock walls quantified by terrestrial lidar measurements: A case study in the Mont Blanc area. Geophys. Res. Lett., **35**(10): L10502.

Schohl, G.A. & Ettema, R. 1986. Theory and laboratory observations of naled ice growth. Journal of Glaciology, **32**(111): 168-177.

Schohl, G.A. & Ettema, R. 1990. Two-dimensional spreading and thickening of aufeis. Journal of Glaciology, **36**(123): 169-178.

Sepúlveda, S. & Padilla, C. 2008. Rain-induced debris and mudflow triggering factors assessment in the Santiago cordilleran foothills, Central Chile. Natural Hazards, **47**(2): 201-215.

Shen, H.T. & Yapa, P.D. 1985. A unified degree-day method for river ice cover thickness simulation. Canadian Journal of Civil Engineering, **12**(1): 54–62

Short, M.B., Baygents, J.C. & Goldstein, R.E. 2006. A free-boundary theory for the shape of the ideal dripping icicle. Physics of Fluids, **18**(8): 083101-083105.

Singh, P., Kumar, N. & Arora, M. 2000. Degree-day factors for snow and ice for Dokriani Glacier, Garhwal Himalayas. Journal of Hydrology, **235**(1-2): 1-11.

Solomon, D.K., Moore, G.K., Toran, L.E., Dreier, R.B. & McMaster, W.M. 1992. Status report; a hydrologic framework for the Oak Ridge Reservation: Oak Ridge National Laboratory, (ORNL/TM-12026), Environmental Sciences Division, Publication no. 3815.

Stickler, M. & Alfredsen, K.T. 2009. Anchor ice formation in streams: a field study. Hydrological Processes, **23**(16): 2307-2315.

Streitz, J.T. & Ettema, R. 2002. Observations from an aufeis windtunnel. Cold Regions Science and Technology, **34**(2): 85-96.

Sutinen, R., Hänninen, P. & Venäläinen, A. 2008. Effect of mild winter events on soil water content beneath snowpack. Cold Regions Science and Technology, **51**(1): 56-67.

Szilder, K. & Lozowski, E.P. 1994. An analytical model form icicle growth. Annals of glaciology, **19**: 141-145.

Szilder, K. & Lozowski, E.P. 2000. Numerical simulations of pendant ice formations. Cold Regions Science and Technology, **31**(1): 1-11.

Turcotte, B. & Morse, B. 2011. Ice processes in a steep river basin. Cold Regions Science and Technology, **67**(3): 146-156.

Ueno, K. 2003. Pattern formation in crystal growth under parabolic shear flow. Physical Review E, **68**(2): 021603.

Ueno, K. 2004. Pattern formation in crystal growth under parabolic shear flow. II. Physical Review E, **69**(5): 051604.

Ueno, K. 2007. Characteristics of the wavelength of ripples on icicles. Physics of Fluids, **19**(9): 093602-093610.

Veillette, J.J. & Cloutier, M. 1993. Géologie des formations en surface, Gaspésie, Québec. Commission Géologique du Canada, Ressources naturelles Canada, Ottawa, Carte 1804A, échelle 1/250 000.

Wagnon, P., Sicart, J.-E., Berthier, E. & Chazarin, J.-P. 2003. Wintertime high-altitude surface energy balance of a Bolivian glacier, Illimani, 6340 m above sea level. J. Geophys. Res., **108**(D6): 4177.

Walkinshaw, J.L. & Santi, P.M. 1996. Chapter 21: Shales and other degradable materials. *In* Landslides: Investigation and mitigation, Special report 247. *Edited by* A.K. Turner & R.L. Schuster, National Academy Press, Washington, D.C.

Weiss, J., Montagnat, M., Cinquin-Lapierre, B., Labory, P.A., Moreau, L., Damilano, F. & Lavigne, D. 2011. Waterfall ice: mechanical stability of vertical structures. Journal of Glaciology, **57**(203): 407-415.

Xu, W., Yu, W. & Zhang, G. 2012. Prediction method of debris flow by logistic model with two types of rainfall: a case study in the Sichuan, China. Natural Hazards, **62**(2): 733-744.

Ye, S.Q. & Doering, J. 2004. Simulation of the supercooling process and frazil evolution in turbulent flows. Canadian Journal of Civil Engineering, **31**(6): 915–926.

Zhang, Y., Wang, S., Barr, A.G. & Black, T.A. 2008. Impact of snow cover on soil temperature and its simulation in a boreal aspen forest. Cold Regions Science and Technology, **52**(3): 355-370.
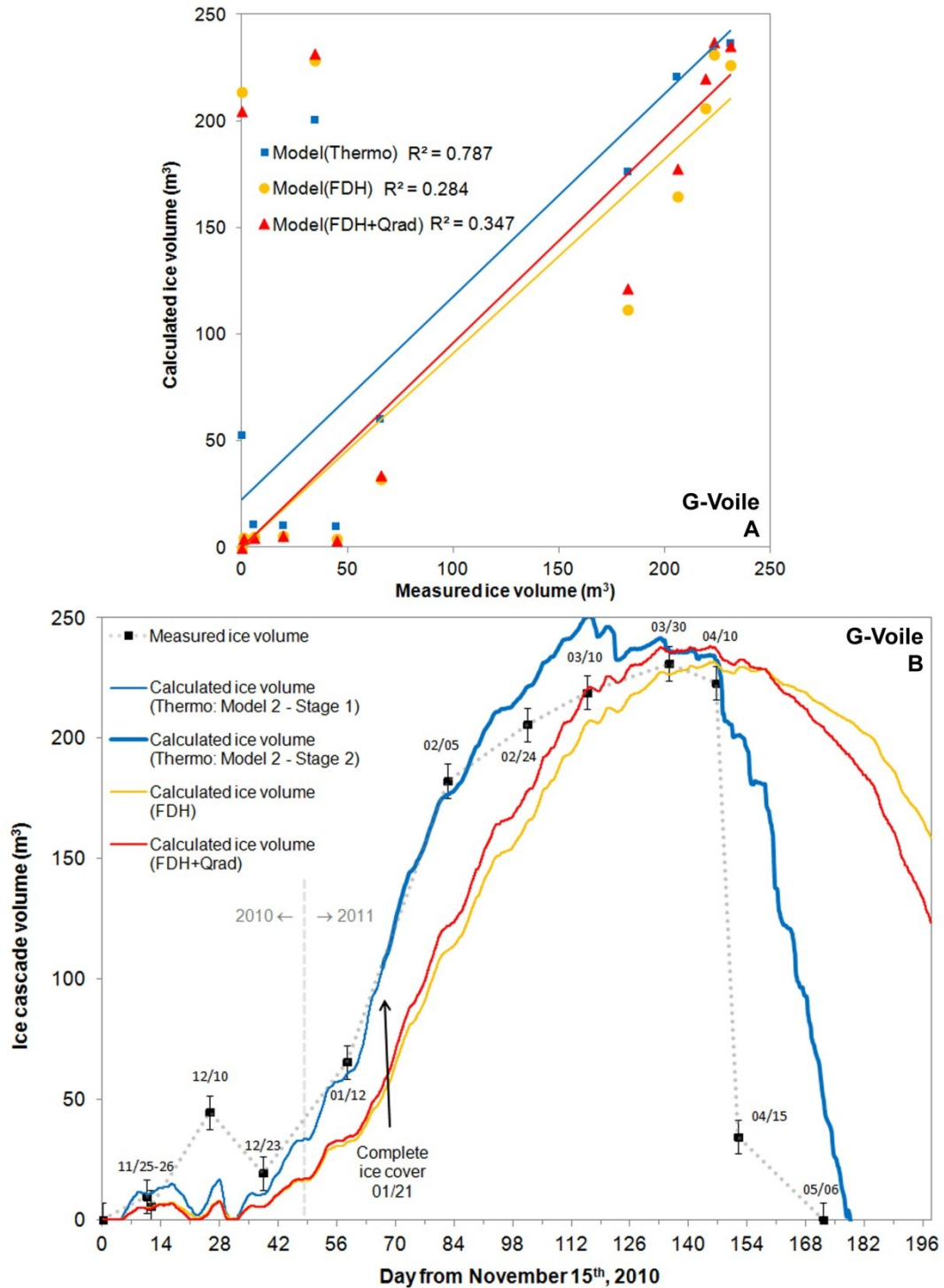
**ANNEXE A**



**Figure A.1.** A) Calculated (Thermo, FDH and FDH+Qrad) vs measured ice cascade volume (G-Voile, chapter 3). B) Calculated (Thermo, FDH and FDH+Qrad) and measured ice cascade volume evolution (G-Voile, chapter 3).